KU LEUVEN

ARENBERG DOCTORAL SCHOOL
Faculty of Engineering Science

Expanding the materials palette for Selective Laser Melting of metals

Karolien Kempen

Dissertation presented in partial
fulfillment of the requirements for the
degree of Doctor in Engineering
Science: Mechanical
Engineering

March 2015

Expanding the materials palette for Selective Laser Melting of metals

Karolien KEMPEN

Supervisory Committee:
Prof. dr. ir. L. Froyen, chair
Prof. dr. ir. J.-P. Kruth, supervisor
Prof. dr. ir. J. Van Humbeeck, co-supervisor
Prof. dr. ir. B. Lauwers
Prof. dr. ir. J. Duflou
Prof. dr. D. Bourell
(University of Texas, Austin)

Dissertation presented in partial
fulfillment of the requirements for
the degree of Doctor
in Engineering Science: Mechanical
Engineering

March 2015

Uitgegeven in eigen beheer, Karolien Kempen, Celestijnenlaan 300 box 2420, B-3001 Heverlee (Belgium)

ISBN XXX-XX-XXXX-XXX-X

D/XXXX/XXXX/XX

Preface

’t is gebeurd!

Na bijna vijf jaar kan ik vol trots terugblikken op een mooie doctoraatsopleiding aan het departement Werktuigkunde van de KU Leuven. Op mijn eentje was dit werk zeker niet tot stand kunnen komen in zijn huidige vorm, en daarom neem ik graag de tijd om heel wat mensen te bedanken...

In de eerste plaats wil ik mijn beide promotoren professor Jean-Pierre Kruth en professor Jan Van Humbeeck bedanken.
Jean-Pierre, bedankt voor de kans om in eerste instantie een masterthesis, en ook later mijn doctoraatsonderzoek te mogen starten onder uw begeleiding. Uw passie en kennis in de wereld van Additive Manufacturing zijn erg aanstekelijk en hebben mij van de eerste tot de laatste dag geïnspireerd. Bovendien staat in uw drukke planning uw deur steeds open, wat niet enkel door mij maar door de hele groep ten zeerste geapprecieerd wordt.
Jan, bedankt voor uw vertrouwen in mij én in mijn werk. Ik kan steeds bij u terecht met mijn véle materiaalkundige vragen, én niet-materiaalkundige adviezen. Tot de allerlaatste loodjes wist u mij te motiveren en daarvoor is geen dankwoord te groot.
Tijdens mijn volledig doctoraatstraject kon ik niet bij één, maar bij twee promotoren steeds terecht en dat is als doctoraatstudent een waar plezier. Bedankt!

Een woord van dank ook aan de andere leden van de examencommissie, voor alle tijd en moeite die zij investeerden in het lezen en kritisch beoordelen van mijn proefschrift en dagelijks werk. Uw waardevolle opmerkingen hebben de scriptie tot zijn huidige vorm gebracht. Professor Ludo Froyen, professor Joost Duflou en professor Dave Bourell, Bedankt, Thanks!
Professor Bert Lauwers wens ik bovendien nog te bedanken voor zijn vertrouwen

in mijn organisatie-vermogen bij de ISEM conferentie en de prachtige kans tot verdere ontplooiing die ik gekregen heb aan KU Leuven- Technologiecampus Geel. Bedankt!

Ik heb 6 jaar lang het geluk gehad om te mogen werken in het enthousiaste team van *"de Gele Trappers"*. Stuk voor stuk fantastische mensen, en zonder hen was dit werk nooit tot stand gekomen. Jullie hielpen mij door alles heen, al dan niet werk-gerelateerd, merci!
In eerste instantie bedankt aan mijn maatje Stijn Clijsters, buiten een fantastische collega waar iedereen op kan rekenen, ben je een echte vriend geworden! Merci, voor alles en nog zo veel meer!
Sam Buls, held! Er is werkelijk niets wat jij niet kan. Elke dag nog doe je mij verbazen. Merci voor alles, op de bureau en daarbuiten!
Mathew Speirs, I *thouroughly* enjoyed working with you. You're always ready to help out and teach us some English language. Thanks!
Raya Mertens, in jouw handen weet ik dat ik de AM groep gerust kan achterlaten. Je bent een grote meerwaarde voor het team, Merci!
Sasan Dadbakhsh, we had some great discussions and you know how to put smiles on all our faces, Thanks!
Sebastian Meyers, de toekomst van de keramiek, je staat altijd klaar om mee te denken, redeneren, of simpelweg het werk te verlichten, merci daarvoor!
Dries Van Camp en Bavo Fallon, jullie passen perfect in de AM groep en heb alle vertrouwen in de goede opvolging, merci!
Uiteraard ook een woord van dank aan de buren van de metrologie-groep, die ons steeds bijstaan met raad en daad in de metrologie. Merci Frank, Bart, Tan Ye, Gabriel en Min, maar uiteraard ook Haibin, Nick en Philip.

Uiteraard ook nog een groot woord van dank aan Evren Yasa, Tom Craeghs, Simon Van Bael en Jan Deckers. Ik heb zo veel van jullie geleerd en jullie namen steeds tijd en geduld om me verder te helpen of op te leiden, merci!
Evren, I look up to you in every way. You are the one that spiked my interest for research in general. I can not thank you enough.
Lore Thijs en Bey Vrancken, ik ben nog steeds verre van een materiaalkundig expert, maar alles wat ik weet, heb ik van jullie geleerd, merci daarvoor!
Tot slot ook nog een dikke merci aan de andere leden van de AM groep, voor hun waardevolle bijdragen aan de discussies en projecten: Jef, Brecht, Ann en Chen Li.

Een erg bijzonder woord van dank gaat naar Lieve Notré, Karin Dewit en Anja Vansteenwegen, voor hun logistieke en administratieve ondersteuning, de

fijne babbels en leuke aanmoedigingen. Het is een enorme steun te weten dat er mensen zijn waar je steeds met alles terecht kan. Ook iedereen van de andere administratief ondersteunende diensten verdienen uiteraard een woord van dank: Valerie, Frieda, Régine, Stéphanie, Carine, Marijke, José en Peter.
Dirk Bastiaensen, Eddy Smets en Pascal Coremans wens ik te bedanken voor hun technische hulp bij zowel het onderzoek als de didactische taken.
Ook aan de helpende handen van MTM: Paul Crabbé, Olivier Van Roey, Wout Veulemans, Rudy Devos en Kris Van de Staey. Bedankt!

Onder het motto "geen inspanning zonder ontspanning", wil ik zeker ook nog *de kaarters* en *de squashers* bedanken, voor de vele fijne middagen. Niets geeft meer moed om weer fris aan de namiddag te beginnen dan een dubbele open miserie, afgeklopt en tegengeklopt, met JaPie, de Baartkaas, De Kers, Baboe en de vele anderen. Bedankt!

Doorheen de jaren kreeg ik de hulp van vele uitstekende thesisstudenten: Aline Royakkers, Davy Orye, Peter Van Puyvelde, Raya Mertens, Miguel Godino Martinez en Maria Luz Montero Sistiaga. Jullie harde werk leverde een grote bijdrage aan deze onderzoeksresultaten, bedankt!

Ik wens vervolgens ook nog de nieuwe collega's bij KU Leuven TechnologieCampus Geel en Mobilab te bedanken om mij doorheen de laatste loodjes te helpen. Bedankt!

Bedankt ook aan al mijn vrienden, die mij doorheen de jaren van de nodige ontspanning en bemoedigende babbels hebben voorzien, en op het einde van de volledige krankzinnigheid gered hebben ;-). Bedankt Evy, Hanne en Mieke. Bedankt aan alle vrienden van de CCC. Bedankt aan alle ploeggenootjes van Mevoc en Voach en de Splitters uiteraard. Bedankt aan alle vrouwen van Dionysus. Bedankt aan alle klasgenoten doorheen de jaren industrieel en burgerlijk ingenieur.
Bedankt ook aan Renée en Jinthe, zonder het te beseffen hebben jullie me door moeilijke momenten geholpen.

Tot slot richt ik graag een woord van dank aan mijn ouders. Make en Paul, Pake en Greet, jullie hebben steeds in mij geloofd, en mij alle middelen gegeven om de opleidingen te kunnen volgen waar ik zelf voor koos. Er bestaat geen enkele manier om jullie daarvoor voldoende te bedanken. Ik ben trots op wie ik ben vandaag en dat is volledig jullie verdienste. Lott, ik kan mij geen betere zus wensen. Merci voor alles, tijdens deze doctoraatsperiode, maar ook lang ervoor en nog lang erna. *There's no greater friend than a sister, and there's no greater sister than you.*

Karolien Kempen

Abstract

Selective Laser Melting (SLM) is an Additive Manufacturing technique in which a product is built up in a layer-by-layer fashion, by melting metal powder particles using a high power laser. It enables the production of complex three-dimensional parts with high density. As SLM is a relatively new manufacturing process, many obstacles have to be overcome and the goal of this work is to address some of the process' limitations and mainly to broaden the materials palette.

Four different materials, divided in two material groups were processed in this work. The first part describes the work on two aluminum alloys, a cast aluminum alloy, A360.0, and a wrought aluminum alloy, 7075. The second part handles the process capabilities of two types of tool steel: a low-carbon maraging steel 18Ni300, and a high-carbon M2 High Speed Steel. The primary goal of this thesis is to produce nearly-fully dense parts in all four materials. Along the way, barriers need to be overcome that characterize the SLM process, but prohibit it from reaching a higher technology readiness level, like thermal stresses, cracks and poor dimensional accuracy.

Cracks are eliminated by the use of either baseplate pre-heating, or addition of alloying powders (e.g. silicon), depending on the origin of the crack formation. The influence of the composition, size and morphology of base powder material is shown to be influential for the final part quality.

After proper powder selection, the production of nearly-fully dense parts can be achieved after optimization of scan parameters like laser power, scan speed, scan spacing and layer thickness. Laser remelting as an additional scan strategy can increase the part density and improve the top surface roughness significantly. Furthermore, a preliminary experiment of single track scans offers a great amount of information and defines a process window, in which a stable melt pool is formed.

Material characterization in terms of mechanical properties and microstructure are conducted to compare the quality of as-built SLM parts to conventionally produced and heat treated parts.

Beknopte samenvatting

Selectief Laser Smelten (SLM) is een additieve vervaardigingstechniek (AM) waarbij een product laagsgewijs opgebouwd wordt door metalen poederdeeltjes aan elkaar te smelten met een laser. De techniek laat toe om complexe, driedimensionele werkstukken op te bouwen die bijna volledig dens zijn. Daar SLM een relatief nieuwe productietechniek is, moeten nog vele obstakels overwonnen worden, en het doel van dit werk is om enkele van deze limitaties te adresseren en het materialenpallet uit te breiden.

Vier verschillende materialen, verdeeld in twee materiaalgroepen, werden verwerkt. Het eerste deel bespreekt het werk op twee aluminium legeringen: een gietlegering A360.0 en een kneedlegering 7075. Het tweede deel beschrijft SLM van twee gereedschappstalen: maraging staal 18Ni300 (met laag koolstofgehalte) en M2 snelstaal (met hoog koolstofgehalte). Het hoofddoel van deze thesis is de productie van bijna volledig dense werkstukken in de vier metalen. Om dat doel te bereiken moeten meerdere barrières overwonnen worden, zoals thermische spanningen, scheurvorming en ondermaatse dimensionele nauwkeurigheid.

Scheuren worden vermeden door verwarming van de basisplaat, of het toevoegen van andere poedermaterialen (bv. silicium), afhankelijk van de oorzaak van de scheurvorming.

De invloed van de samenstelling, de deeltjesgrootte en morfologie van het poedervormig basismateriaal is van groot belang voor de kwaliteit van het eindstuk.

Na zorgvuldige poederselectie kan een bijna volledig dens werkstuk opgebouwd worden, door optimalisatie van scan parameters zoals laser vermogen, scan snelheid, scan afstand en laagdikte. Laser hersmelten als extra scan strategie kan de densiteit van het werkstuk nog verder verhogen en bovendien de ruwheid van het bovenoppervlak sterk doen afnemen.

Bovendien kan een initieel onderzoek waarbij enkel tweedimensionale lijnen gescand worden reeds veel nuttige informatie leveren over de vorming van het smeltbad. Hieruit wordt een proces venster opgesteld waarbinnen een scanlijn voldoet aan de vooropgestelde vereisten.

Materiaalkarakterisatie door mechanische testen en microscopie bepalen tot slot in welke mate de kwaliteit van de SLM-geproduceerde materialen voldoet aan de materiaaleigenschappen voor conventioneel geproduceerde werkstukken.

List of Symbols

Greek letters

α	Rotation angle
α_{therm}	Thermal expansion coefficient
ϵ	Elongation
ϵ_{pl}	Plastic deformation
γ_{SV}	Solid-vapour surface tension
γ_{LV}	Liquid-vapour surface tension
γ_{LS}	Liquid-solid surface tension
ρ	Density
ρ_{pack}	Packing density
λ	Wavelength
λ_{therm}	Thermal conductivity
σ_{comp}	Compressive stress
σ_{tens}	Tensile stress
η	Viscosity
θ	Contact angle
θ_h	Divergence angle

Roman letters

a_1	Scan spacing factor
a_2	Island scanning factor
a_3	Island scanning factor
a_{therm}	Thermal diffusivity
A_{abs}	Absorbtance
A_s	Austenite start temperature
c_p	Specific heat capacity
d	Laser spot diameter
$d_{v,x}$	Particle size
E	Modulus of elasticity
E_v	Energy density
E_A	2-dimensional Energy density
E_L	1-dimensional Energy density
$\overrightarrow{G}$	Temperature gradient
h	Scan spacing, Hatch spacing
I	Laser Intensity
L	Melt pool length
M^2	Beam Quality parameter
M_a	Marangoni number
M_s	Martensite start temperature
P	Laser Power
P_a	Average roughness (no filter)
P_t	Peak-to-peak roughness (no filter)
P_{sk}	Skewness (no filter)
P_q	Root mean square roughness (no filter)
$r_{min,circ}$	radius of minimum circumscribed circle
$r_{max,insc}$	radius of maximum inscribed circle
$\overrightarrow{R}$	Growth rate
R_a	Average roughness
$R_{p,0.2}$	0.2% Proof stress
R_t	Peak-to-peak roughness
r_f	Focus Radius
S_a	Average 3D roughness
S_t	Peak-to-peak 3D roughness
t	Layer Thickness
t_f	Solidification time
T	Temperature
T_L	Liquidus temperature
T_m	Melting temperature
T_S	Solvus temperature

HRC	Hardness Rockwell C
HV	Hardness Vickers
v	Scan Speed
$\dot{V}$	Scanning productivity
X_1	Scan offset in X direction
Y_1	Scan offset in Y direction

Abbreviations

2D	Two Dimensional
3D	Three Dimensional
3DP	3D Printing
AISI	American Iron and Steel Institute
AM	Additive Manufacturing
ANSI	American National Standards Institute
APT	Atom Probe Tomography
ASM	American Society for Metals
ASTM	American Society for Testing and Materials
bcc	Body-Centered Cubic
BPP	Beam Parameter Product
BSE	Back Scatter Electron
CAD	Computer Aided Design
CL	Concept Laser
CCM	Crack Compliance Method
CMOS	Complementary Metal-Oxide Semiconductor
CT	Computed Tomography
CW	Continuous Wave
DDF	Direct Digital Fabrication
DIN	Deutsches Institut fur Normung
DLF	Direct Laser Fabrication
DMD	Direct Metal Deposition
DMLS	Direct Metal Laser Sintering
EBM	Electron Beam Machining
EDM	Electrical Discharge Machining
EDX	Energy Dispersive X-Ray Spectroscopy
FDM	Fused Deposition Modeling
FE	Finite Element
FEG	Field Emission Gun
fcc	Face-Centered Cubic
HIP	Hot Isostatic Pressing
HPDC	High Pressure Die Cast
HSS	High Speed Steel
HT	Heat Treatment
ICP-AES	Inductively Coupled Plasma Atomic Emission Spectroscopy
IET	Impulse Excitation Test
ISO	International organization for standardization
LC	Laser Cladding
LENS	Laser Engineered Net Shaping
LM	Layer Manufacturing

LMD	Laser Metal Deposition
LM-Q	Laser Melting-Quality
LOM	Laminated Object Manufacturing
LOM	Light Optical Microscopy
OM	Optical Microscopy
PID	Proportional-Integral-Derivative
RM	Rapid Manufacturing
RP	Rapid Prototyping
SE	Secondary Electron
SEM	Scanning Electron Microscopy
SIM	Strategic Initiative Materials
SLA	Stereolithography
SLE	Selective Laser Erosion
SLM	Selective Laser Melting
SLS	Selective laser Sintering
SMD	Shape Metal Deposition
TGM	Temperature Gradient Mechanism
UTS	Ultimate tensile strength
WAAM	Wire Arc Additive Manufacturing
WEDM	Wire Electrical Discharge Machining
XRD	X-ray Diffraction
YAG	Yttrium Aluminum Garnet

Contents

List of Figures

List of Tables

Chapter 1

Introduction

This thesis mainly aims at contributing to raise the SLM process to a competitive level of manufacturing. As the ambition is broad and many obstacles have to be overcome, the goal of this work is to address some of the process' limitations and mainly to broaden the materials palette. In this chapter, the general group of Additive Manufacturing technologies is paraphrased and an overview of the different processes that fit within this group is given (section 1.1). This first section also presents the most common advantages and applications of Additive Manufacturing. Section 1.2 describes the Selective Laser Melting technology, with a detailed description of the process, the main advantages and applications, the wide variety of process parameters and the physical interactions that take place upon the formation of the melt pool.

1.1 Additive Manufacturing

Additive Manufacturing (AM) depends on building three-dimensional parts by adding base material in a layer-by-layer fashion. A three-dimensional computer model is digitally sliced into two-dimensional layers. The computer program subsequently generates a suitable scan pattern in each of these layers. This data is then sent to the AM machine which builds the part layer-to-layer to completion. Thus, these Additive Manufacturing processes rely on adding base material, instead of removing it like in the more conventional subtractive processes like turning, milling and grinding, or forming it like e.g. in forging, pressing and incremental forming.

While "Additive Manufacturing" is the proper term to describe this group of processes, as defined in the ASTM F2792 standard [11], other synonyms like Rapid Manufacturing, Freeform Fabrication, Layer manufacturing, Direct Digital Fabrication , 3D Printing, ... are still used as well.

Different processes fit within the group of AM technologies. Their basic principle is the same, but they employ different types of base material and binding mechanisms. Table 1.1 presents the base materials, the machine lay-out, the layer creation technique and the binding mechanism of several Additive Manufacturing processes. Most processes perform a material deposition step, followed by a material consolidation step, which are then repeated until part completion. Some processes combine material deposition and consolidation in one step.

Processing of polymers usually happens through Stereolithography, 3D-printing, Fused Deposition Modeling or Selective Laser Sintering. The focus of this work lies within the powder bed based processes for metals. The Selective Laser Melting process is an AM technique where a laser melts consecutive layers of powder on top of each other. A more in-depth introduction on the SLM process is given in section 1.2. The laser cladding technique can also bring important insights to this work, as it is also a laser-based metal powder AM process. The EBM process is also of relevance as it is also a metal powder-bed fusion technique, but it doesn't form the main focus of this work. These three latter processes are most commonly used for Additive Manufacturing of metals [56, 91, 139].

SLM and EBM are similar in that way, that they both apply heat in a high-energy beam to a powder bed, being a laser beam for SLM and an electron beam for EBM [62]. In booth processes, the powder is fully melted and consolidated upon cooling to a nearly fully dense part. In EBM however, the particles are first sintered together in a pre-heating step, to avoid that the powder particles would repel each other due to the electromagnetic charging of the electron beam. It is because of this electromagnetic charging, that the EBM process is only fit for processing non-magnetic metals [114, 48]. This doesn't form a problem in SLM, because a laser beam is employed instead of an electron beam. Theoretically, any metal with a good absorptivity for the laser light can be processed.

The pre-heating that is employed in EBM does come with an advantage compared to SLM: higher ambient temperatures are reached (up to $700°C$ [78]), which results in lower thermal gradients reducing the thermal stresses. Furthermore, the atmosphere in SLM is usually commercially pure Argon or Nitrogen gas, compared to vacuum in Electron Beam Melting causing less oxidation and

	Process	**Lay-out**	**Layer Creation Technique**	**Phase change**	**Materials**
LIQUID	Stereolithography (SLA)	Liquid resin in a vat	Liquid layer deposition	Photo-polymerization	Acrylates, epoxies, filled resins
	Fused Deposition Modeling (FDM)	Material melted in a nozzle	Continuous extrusion	Solidification by cooling	Polymers, wax, filled polymers, metals
	Ink jet printing	Droplets of molten material	Drop on demand deposition	solidification by cooling	Polymers, wax
POWDER	3D Printing	Binder + powder in bed	Layer of powder	No phase change of powder, solidification of binder by cooling/evaporation	ceramics /metals /polymers with binder
	Selective Laser Sintering/Melting (SLS/SLM)	Powder bed	Layer of powder	Sintering/melting by laser and re-solidification by cooling	polymers, metals , ceramics
	Electron Beam Melting (EBM)	Powder bed	Layer of powder	Melting by electron beam and re-solidification by cooling	non-magnetic metals
	Laser Cladding (LC), (also LENS, DMD, ...)	Powder delivery through nozzle	Continuous injection of powder	laser melting and solidification by cooling	metals, (ceramics)
SOLID	Laminated Object Manufacturing	Feeding, cutting and binding of sheets	Deposition of sheet material	No phase change of sheet, binding by phase change of solder, glue or otherwise	Paper, polymer, composites, metals, ceramics
	Shape Metal Deposition (SMD)	Metal wire delivery through nozzle	Continuous injection of metal wire	Laser melting and solidification by cooling	Metals
	Wire Arc Additive Manufacturing (WAAM)	Metal wire delivery through nozzle	Continuous injection of metal wire	Arc beam melting and solidification upon cooling	Metals
GAS	Selective Laser Chemical Vapour Deposition	Gas flow in laser	Condensation of gas	Forming solid material from gas by chemical reaction	Metals, ceramics

Table 1.1: Overview of the main Additive Manufacturing processes, sorted by the aggregation state of the base material. (updated from [86])

contamination of the melt pool during EBM [113]. The SLM process on the other hand, enables a higher resolution and better surface roughness than the EBM process, and ensures an easy release of the part from within the powder bed and reuse of the non-used powder as it is not pre-sintered.

SLM is not the only metal AM process involving a laser beam as an energy source. Several varients of direct energy deposition processes use a laser beam to melt the base material, and (re-)solidification happens upon cooling. Examples are Laser Engineered Net Shaping (LENS) [55, 111], Direct Metal Deposition (DMD)[45, 102], Laser Cladding (LC) [138, 140], Direct Laser Fabrication (DLF) [126, 175], Laser Metal Deposition (LMD) [189], laser (beam) deposition [15], laser rapid forming [94] and Shaped Metal Deposition (SMD) [15, 21]. For all these processes, the base material is fed into the focus of the laser beam through a nozzle. In some processes like Wire Arc Additive Manufacturing (WAAM), material is also fed through a nozzle, but into an arc beam instead of a laser beam [74]. These processes are usually less accurate than the SLM process, as they involve a divergent, not well focused powder jet and a much higher energy input and thus a larger melt pool, surrounded by semi-melted particles sticking to the part surface.

Advantages and Applications Due to their layer-wise nature, the AM processes gain many advantages compared to conventional manufacturing processes:

- High geometrical freedom creating design opportunities like internal cavities, thin walls, lightweight structures or monolithic parts instead of assemblies.
- The additive (i.e. no excess material needs to be removed) and near-net-shape production leads to a minimal amount of waste material and post-processing steps, hereby reducing lead times and costs.
- Some processes are suited for the fabrication of functionally graded materials.
- The direct link between the digital design and the final part enables the mass production of parts with customized features, and if needed a fast adaptation thereof.

Overall, Additive Manufacturing is a technique that expedites the product development process. Companies all over the world rely on AM in an effort to reduce the time to market, improve product quality, reduce cost and waste, and

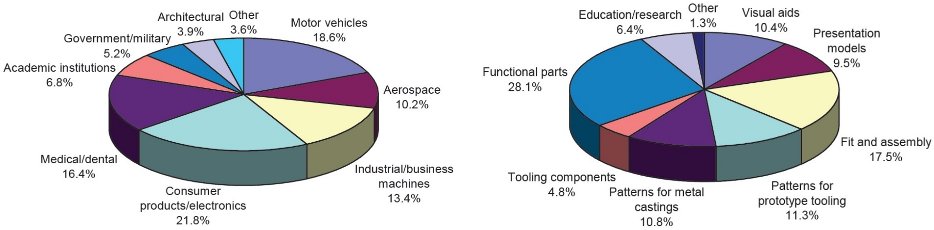

Figure 1.1: Results of a survey by Wohler's Associates with 31 AM manufacturers and 74 service providers on (left) what industries are served; (right) how their customers use AM parts. [172]

develop novel products in a creative way.

The long list of advantages leads to a broad field of applications for Additive Manufacturing. Wohler's report 2013 [172] reports the distribution of AM applications, as indicated by companies all over the world that use Additive Manufacturing (Figure 1.1).

Design and manufacturing companies use AM parts for all kinds of products in the industrial, bio-medical, aeronautical and military markets, to name just a few; complex tools, medical implants, geometrically challenging protoypes, engine parts, lightweight components, assemblies for airplanes and art or fashion artefacts are just the beginning of a very extensive list of products that have benefited from the AM technology. A small selection of AM applications is shown in Figure 1.2

1.2 Selective Laser Melting

The focus of this thesis lies within the Selective Laser Melting (SLM) process, which is an AM process in which the base material is powder and the particles are bound by melting with a laser beam. The high thermal energy of the laser beam melts the powder material, which then changes to a solid phase as it cools down. Other terms in the AM industry for this process are Powder Bed Fusion, Direct Metal Laser Sintering (DMLS) and Laser Cusing.

This section consists of four subsections. In 1.2.1 the different steps in the SLM process are enumerated and the different elements of a general SLM machine are shown. The second subsection elaborates on the advantages of the SLM process, and to which fields of application they lead. In 1.2.3 the large amount

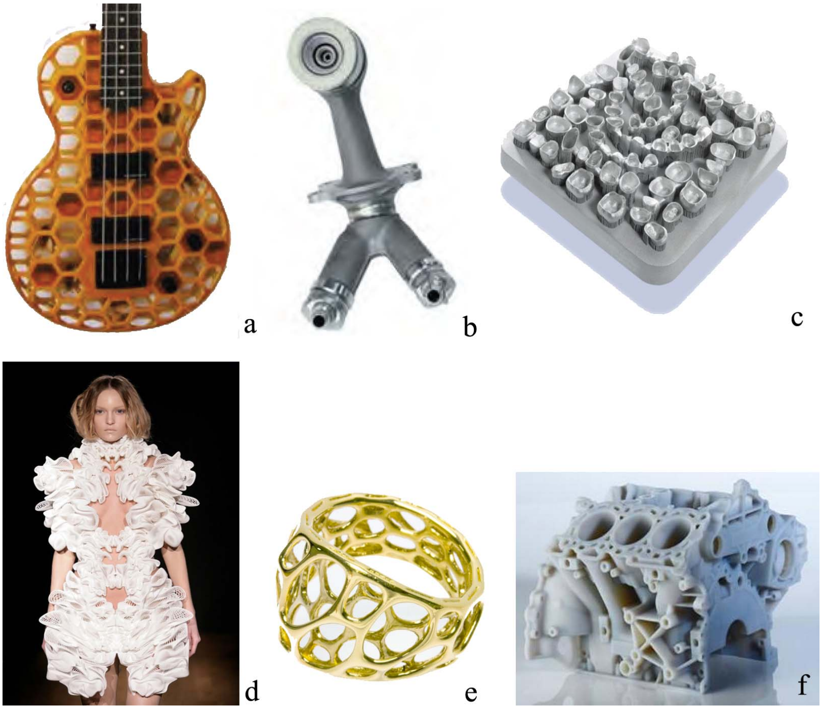

Figure 1.2: A small selection of AM applications: a) a guitar casing [172] b) an engine fuel nozzle [51] c) dental crowns [35] d) an Iris Van Herpen designer dress [101] e) jewelry [47] f) an engine prototype [148]

.

of parameters that influence the process behavior are described. A subdivision is made between scan parameters, machine parameters and material parameters. The last subsection handles on the formation of the melt pool and the physical phenomena that are encountered.

1.2.1 Process

A schematic overview of a typical SLM machine and its main components is depicted in Figure 1.3. The module consists of a build platform, on which a baseplate is mounted. The baseplate is a plate where the final part will be built upon. The build platform moves down during production, in steps equal to the thickness of one layer. Next to the build platform, a feed container

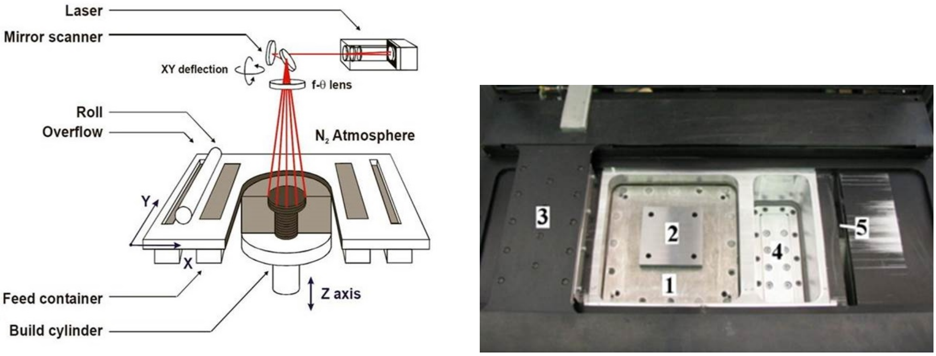

Figure 1.3: A schematic overview of the SLM machine and its main components (left). The build module consisting of a build platform(1) with a baseplate(2), a coating system(3) a feed container(4) and an overflow container(5)(right).

moves upward during processing. The feed container is filled with base powder material and it provides the powder for every new layer. A coater system which can be a roller or a scraper, spreads the powder supplied by the feed container in a thin layer over the baseplate. Then, a laser scans the predefined scan pattern on the powder bed. For the processing of metals, a laser with a wavelength approaching 1064 nm is used, because it has the highest absorbtivity for metals.

The laser beam passes through an f-theta lens, which adjusts the focus of the laser beam, according to the scanning angle theta in order to obtain a horizontal (flat) focus plane coinciding with the powder bed surface. The laser light is deflected onto the powder bed through a galvano scanner which consists of two galvano mirrors for the X- and Y-direction of the laser path. The entire build module operates under a protective atmosphere of Argon or Nitrogen gas, to avoid reactions with the hot solidified melt pool.

The entire Selective Laser Melting process includes the following steps:

1. A 3-dimensional CAD drawing is created. The orientation of the part can be changed for better process conditions or reduced production time, and support structures can be added to enhance the production of downfacing areas.
2. This 3-dimensional model is sliced into 2-dimensional layers with a certain layer thickness. For SLM, this layer thickness generally ranges between 20 and 100 μm.

3. Scan vectors are generated that fill the 2D slices. This defines the path that the laser will follow in each layer. The scan vectors can be generated in different scanning patterns like zig-zag, unidirectional, spiral, meander, etc...(Figure 1.4)
4. The SLM machine is prepared for production. This includes mounting a baseplate in the build platform, putting powder in the feed container and allocating parameters to the different scan vectors in the machine software.
5. During production, a powder layer is deposited: the feed container moves up, the build platform moves down over the height of one layer and the coater spreads a thin layer of powder on the baseplate.
6. The laser beam is directed across the powder bed, according to the defined scanning pattern and parameters, creating a melt pool on its path. After interaction with the laser beam, the melt pool cools down and the material solidifies.
7. Steps 5. and 6. are repeated until part completion.
8. After complete cooldown to room temperature, the part attached to the baseplate is removed from the machine. The powder is sieved before re-use.
9. The parts are cut from the baseplate typically by Wire Electrical Discharge machining (WEDM).
10. Some post-processing steps might be necessary to meet the dimensional or qualitative requirements. This might include sandblasting, milling or a heat treatment to induce precipitation or eliminate residual stresses.

A great complexity and uniqueness of the process is caused by the laser-metal physical interaction. The final properties of the laser processed material are significantly affected by the laser-metal interaction, while typical processing issues like porosity, balling and residual stresses result from this stage.
During SLM, the short interaction of the laser and the powder bed leads to rapid heating and cooling. Most of the laser beam energy is absorbed, while some heat is lost by radiation, convection and evaporation. Surplus, while the melt pool is in the fluid state, the material can interact with the atmosphere, for instance by dissolution of remaining oxygen or nitrogen [151].

Because of the rapid movement of the laser, and the relatively large mass of colder material surrounding the melt pool, the cooling rates are very high and solidification happens fast. Metallurgically, this leads to metastable phases, a

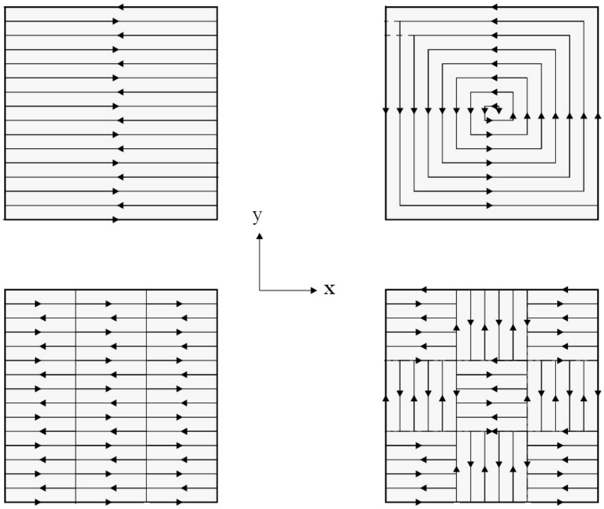

Figure 1.4: Different scan strategies that can be applied to fill a 2D surface with scan lines, from left to right, top to bottom: zig-zag scanning ; spiral scanning ; paintbrush scanning and island scanning [70]

very fine microstructure and thermal stresses. To avoid these thermal stresses which can lead to the layer curling up, parts in the SLM process are always built on a metal substrate, a baseplate.

1.2.2 Advantages and Applications

The unique and layer-wise production method of SLM opens a broad perspective of several advantages and applications. The most important one is undoubtedly the freedom of design. SLM can produce an object of virtually any shape, leading to entirely new design rules and a very broad field of lightweight structures. Moreover, the process is very flexible in two ways. First, design changes can easily be made, even at the very end of the process chain, and secondly, many different shaped parts can be produced in one batch. Both effects decrease the lead time and time-to-market significantly.
Furthermore, direct production is possible, without costly and time-consuming tooling. Surplus, different assembly-parts can be made in one monolithic part, increasing the product's life time. Because of the near-net-shape production, the process is very material-efficient. Any powder that was not consolidated

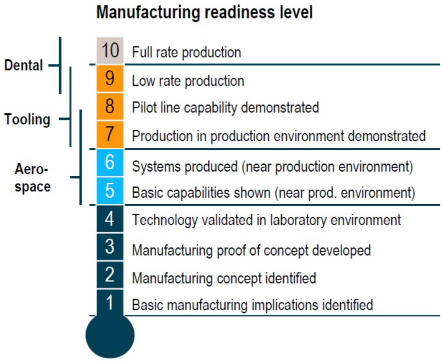

Figure 1.5: Indication of the manufacturing readiness level for different application areas in Additive Manufacturing [37]

during production can be sieved and re-used in the next batch.
In addition, materials that are hard to process (like hard metals and tool steels) can be used to make nearly-full dense parts.

While Additive Manufacturing was invented for the purpose of rapid prototyping, process speed, material cost and part quality were not an issue until recently. Meanwhile, the AM technologies, amongst which SLM plays an important role, have reached both a higher technology readiness level as a higher market readiness level. The manufacturing readiness level still varies a lot in different fields of application, as indicated in Figure 1.5. More and more, the current market demands the additive manufacturing of parts in an economical way, and with high quality. Some examples of industries where the SLM process can deliver great advantages for several applications are given below.

Automotive: Production of special components for motorsport (e.g. cooling ducts) or prototypes for visual aids. An example is found in the re-design of a fuel pump, to improve its functionalty [37]. By the reduction in weight and the replacement of straight channels with sharp corners by smooth free-form channels, lower pressure drops were measured and less leakage occured.

Aerospace: Production of lightweight parts with complex geometry, e.g. fuel nozzles, stationary turbine components, re-design of burners, ... A great benefit of SLM in aerospace industry is the possibilty for severe weight reduction by optimizing the design structure. As example, a conventional belt buckle weighs 155 g. By design optimization, the weight was reduced by 55 %. For an Airbus 380, this would mean a reduction of 72.5 kg, leading to a fuel reduction of 3.3 million liters over the airplane's lifetime [37].

Medical/Dental: Production of dental bridges, crowns and caps, customized prosthetics such as hip implants [168]. Whereas standard implants might not fit, and the production of a single-series part is very costly, SLM can offer a great solution for patient-specific implants. Based on a three-dimensional scan, the resulting implant fits perfectly into place, leading to faster recovery and reduced operation time. For dental crown for instance, one SLM machine can produce up to 450 crowns per day, while a dental technician can make around 40.

Tooling: Manufacturing inserts and tools/moulds with conformal cooling channels or micro-features.

Other: Several other industrial areas such as machine/device builders, military, architectural, design and fashion, or even jewelry, where complex geometry, weight reduction, no material waste and high customization are great advantages.

1.2.3 Process Parameters

The SLM process' great complexity lies in the many thermal, physical and mechanical interactions and the influence of an extensive amount of parameters on these interactions. Three groups of influential parameters can be distinguished: scan parameters which are selected by the machine operator, material parameters which are fixed by the choice of material and powders, and the machine parameters, fixed by the type of machine, like laser properties and the process atmosphere.

Scan Parameters

The scan parameters are chosen by the operator and thereby strongly depend on the operator's expertise in parameter optimization. This is why the optimization of the scan parameters for a new material can take a very long time. It is the goal of this thesis to bring insight into the influence of all these

parameters on the melt pool formation and final part properties.
A summary of the scan parameters with the most relevance to this work is given in Table 1.2.

Parameter	**Symbol**	**Unit**	**Description**
Laser Power	P	W	The applied laser energy per unit time
Layer Thickness	t	μm	The thickness of one 2D slice
Scan Speed	v	mm/s	The speed at which the laser beam moves across the powder bed
Scan Spacing	h	μm	The distance between two adjacent scan tracks
Scan spacing factor	a_1	/	Determines the scan spacing in function of the laser spot diameter
Island scanning factor	a_2	/	Determines the distance to the island border in function of the laser spot diameter
Island scanning factor	a_3	/	Determines the overlap between adjacent islands in function of the laser spot diameter
Rotation angle	α	°	The inter-angle scanning rotation between consecutive layers
Scan offset	X_1 , Y_1	μm	The scan track offset between consecutive layers, both in X- and Y-direction
Scan Strategy			The method of filling a 2D surface with scan vectors

Table 1.2: Overview of the most relevant SLM scan parameters.

The **layer thickness** of one powder layer is denoted with the symbol t and is already determined in the slicing step of the process. When cutting the three-dimensional part into 2D-slices, they are cut with a layer thickness t. This is also the depth with which the build platform will be lowered in every step during production, making it the thickness of one powder layer. Note that the final thickness of one layer after melting and solidification is less, because of the shrinkage that happens during the transformation of an about 40 % dense powder layer to a nearly 100 % dense solidified layer. The layer thickness in SLM usually varies between 20 and 100 μm, depending on the process conditions and the part's requirements. The lower limit is defined by the particle size of the powder that was used, in order to deposit a uniform powder layer. The upper limit of the layer thickness is defined by other scan parameters like laser power and scan speed. The formed melt pool must be sufficiently deep to melt throughout the entire layer thickness, and still guarantee a good wetting with the previous layer or baseplate [147]. Surplus, the melt pool must still meet the other requirements for a stable melt pool for SLM. The advantage of a higher layer thickness is the reduced production time. Also the scan speed can reduce the production time, if chosen high enough, and if the scanning time weighs up to the coating time, calculation time etc...

The **scan speed** is the speed at which the laser moves across the powder bed during scanning. It must be taken into account that the nominal speed is always assumed, but due to the dynamics of the scanner system, the nominal speed is not always reached throughout an entire scan vector. In the beginning and at the end of every scan vector, the galvano mirrors in the scanner have to accelerate/decelerate from zero to nominal speed, or vice versa. This acceleration time delay can reach up to 1 ms, leading to severe consequences for parts produced with high scan speed. As long as the galvano mirrors haven't reached the nominal speed, an overheating will take place, since the laser power has reached its nominal value, but the scan speed it too low. This overheating can cause severe process implications like keyhole porosity, increased evaporation, melt pool instability, . . . , as will be shown further on in this thesis. A possible solution for this scanner mirror inertia can be to add so-called 'ghost-vectors' in the beginning and end of every scan vector. The laser power will be set to zero for these vectors, but the scan speed will have time to reach its nominal value, before reaching the actual part border, where the laser power will be turned on [68].
Another way to avoid this overheating due to the scanner mirrors' dynamics, is to implement a filter with a proper PID control loop to guarantee faster response of the mirrors [25].

The **scan spacing** can be defined as an absolute value (in μm) or as a percentage of the laser spot diameter (a_1 x d, with d as the laser spot diameter), depending on the hatching software and SLM machine. The scan spacing

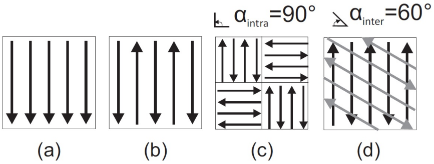

Figure 1.6: Scanning strategies, most commonly used in this doctoral thesis: (a) Unidirectional scanning (b) Bi-directional scanning, or zigzag scanning (c) island scanning or sectoral scanning with intra-layer rotation (d) inter-layer rotations [150]

determines the distance between adjacent scan vectors, and hereby also the overlap between them. In general, an overlap of about 30 to 40 % is desirable, but this can depend on the part requirements and melt pool shape. The overlap between neighbouring scan vectors has a great influence on the part density and surface roughness [53, 112, 84], but also here a good trade-off must be made between part quality and production time.

The **scan strategy** is defined as the way the two-dimensional surface is filled with scan vectors. Like coloring a drawing, there are infinite ways to fill your contours with your 'pencil'. Different scanning strategies affect the thermal history during the SLM process and consequently alter the material properties including density, thermal and residual stress, microstructure, etc. For example, it has been reported that an alternating scanning strategy (rotating the scanning direction in each layer) improves the density of Ti6Al4V parts [82]. The scanning strategy also influences the residual stresses and can be modified to mitigate quality issues such as warpage, cracks and delamination [106]. The most common scan strategies are depicted in Figure 1.6: *unidirectional*: straight, parallel lines in one direction; *zigzag*: straight parallel lines in alternation direction. *Island Scanning, Sectoral scanning*: the area to be scanned is devided into smaller square sectors, of which the size and orientation can be set as desired. The adjacent sectors are scanned perpendicular to each other (Figure 1.6c and Figure 1.7). This sectoral or island scanning is a patented scan strategy developed to decrease the residual stress. However, the scan spacing factors have to be set correctly, to avoid bad connection between the islands and aligned porosity [183].

The island scanning strategy is patented by Concept Laser GmbH [35] and is determined by the size of the islands, the X- and Y-offset, the rotation angle α and the scan spacing factors. **Scan spacing factor** a_1 determines the scan

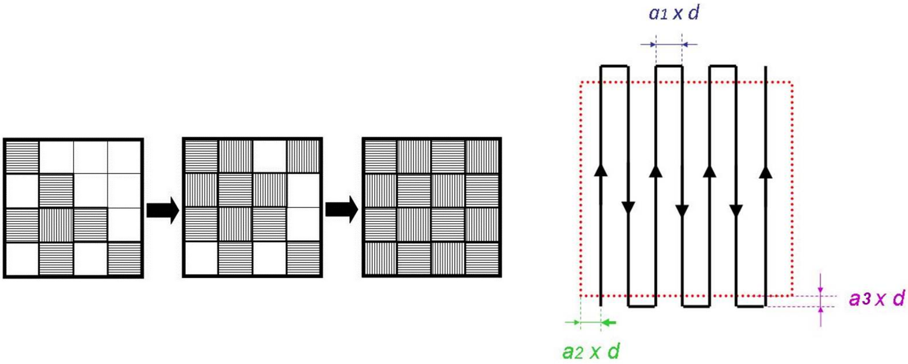

Figure 1.7: Island scanning strategy (left) ; Indication of the scan spacing factors a_1, a_2 and a_3 (right)

spacing h between two neighbouring scan tracks by the following equation 1.1:

$$h = a_1.d \tag{1.1}$$

with h the scan spacing in μm, a_1 the first scan spacing factor and d the laser spot diameter in μm. The second and third scan spacing factors are also expressed as a function of the laser spot diameter, and determine the distance from the island border (a_2) and the overlap with the neighbouring islands (a_3), as indicated in Figure 1.7. A bad choice of scan spacing factors can lead to porosity in between islands which, however small, can lead to deterioration of the mechanical properties [185]. To avoid aligned porosity throughout the height of one part, the scan strategy can be shifted or rotated throughout consecutive layers. The **rotation angle** α is the inter-layer rotation, often chosen as 30°, 60° or 90° for a good density and/or surface quality. The inter-layer rotation can also be used to create a morphological texture in the part [152]. The **scan offset** parameters give an offset for the scan vectors in both X- and Y-direction for every consecutive layer. By proper selection of the scan offset parameters, a density improvement can be accomplished [183].

The effect of the most important process parameters can be combined and presented as the "energy density". The energy density is an engineering parameter representing the energy delivered to a unit volume of powder material. This is achieved by combining the laser power, scan speed, scan spacing and layer thickness as:

$$E_V = \frac{P}{v.h.t}\left[\frac{J}{mm^3}\right] \tag{1.2}$$

with scan spacing h and layer thickness t in [mm]. Accordingly, increasing the laser power or decreasing the scan speed, scan spacing or layer thickness increase the laser energy density. Depending on the tests or interpretation, the two-dimensional or one-dimensional energy input can be defined as in equation 1.3 and 1.4.

$$E_A = \frac{P}{v.h}\left[\frac{J}{mm^2}\right] \tag{1.3}$$

$$E_L = \frac{P}{v}\left[\frac{J}{mm}\right] \tag{1.4}$$

The one-dimensional energy density strongly affects the formation of the melt pool and the presence or absence of the balling phenomenon, keyhole porosity and so on, as discussed extensively in section 4.5.

A very specific addition to the scan strategy is the possibility to apply **laser remelting**. This involves, after scanning a layer (intermediate or top layer) and melting the powder, scanning the same layer again before depositing a new layer of powder. This technique can improve the top surface roughness and eliminate the little residual porosity that might cause problems in applications where high strength and fatigue resistance are required. It also increases the production time substantially, depending on the selected scan speed and scan spacing for the laser remelting step. These parameters can be identical to the SLM parameters or they can be optimized for laser remelting. The increase in production time may be compensated by the fact that laser remelting could eliminate the need for very time consuming post-processes like grinding to improve the surface roughness or Hot Isostatic Pressing (HIP) to remove residual porosity.

Laser remelting can be applied throughout the entire part, for instance for density improvement, but it can also be employed only on the top layer, to reduce the roughness values[134] or to improve other surface properties like micro hardness [129], wear behavior [190], corrosion resistance [167, 177] and wettability [61].

Lamikiz et al. [89] applies laser remelting only on the outer surface of selectively laser sintered parts and reports on surface roughness improvement, whereas Morgan et al. [110] uses laser remelting after each layer to release any entrapped gas and to create a smooth surface finish to every intermediate layer.

Machine Parameters

The machine parameters involve all the parameters that are fixed and are specific to the machine hardware. In this subsection, only the laser and atmosphere parameters are discussed.

A laser (Light Amplification by Stimulated Emission of Radiation) is a suited medium to transfer the heat in this specific process, because it generates a coherent monochromatic radiation with a very low divergence [81], meaning it can transfer a large amount of energy to a very specific location. The **laser parameters** with the most importance to the SLM process are listed in Table 1.3.

Parameter	**Symbol**	**Unit**	**Description**
"' Laser Power	P	W	The applied laser energy per unit time.
Spot diameter	d	μm	Diameter of the laser in the focus spot.
Wavelength	λ	nm	Determines the absorptance of a material.
Intensity	I	J/m^2s	The intensity or energy density of the laser radiation.
Beam Quality	M^2	/	Defines the minimal attainable spot size.
Mode	CW or Pulsed	/	Some lasers can work in both modes: continuous or pulsed.

Table 1.3: Overview of the major laser parameters.

The **intensity I** of the laser beam is defined by the laser power and spot size, as in equation 1.5 with I laser intensity, P laser power and d spot diameter [mm].

$$I = \frac{4P}{\pi d^2} \left[\frac{W}{mm^2} \right] \tag{1.5}$$

This is, however, the right equation for a uniform circular energy pattern. The lasers used in SLM processes usually have a Gaussian intensity profile. To determine how closely the laser approaches the perfect Gaussian shape, the **beam quality** parameter M^2 is defined. The beam quality parameter divides the Beam Parameter Product (BPP) of the laser beam by the BPP of a perfectly Gaussian beam, as defined in equation 1.6.

$$M^2 = \frac{BPP}{BPP_{Gaus}} = BPP\frac{\pi}{\lambda} \tag{1.6}$$

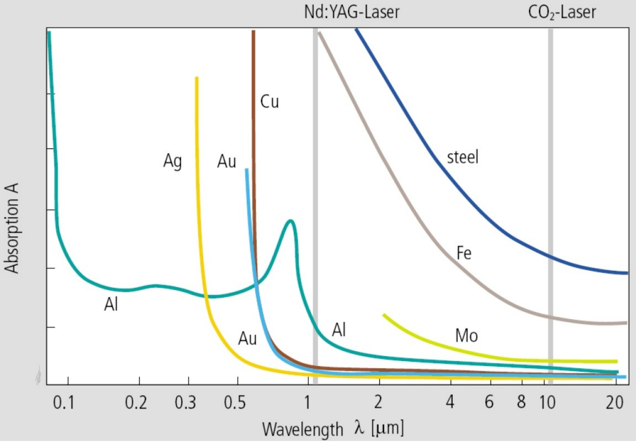

Figure 1.8: Absorption of metals at room temperature at different radiation wavelengths [158].

with

$$BPP = \theta_h r_f = \theta_h \frac{d}{2} \tag{1.7}$$

with θ_h the divergence angle and r_f the focus radius. The closer the beam quality parameter M^2 reaches to 1, the better the beam quality.

Besides from having an important influence on the focusability of the laser beam, the radiation **wavelength** λ of the laser also strongly determines the absorptance of the laser energy by the metal powder. Figure 1.8 shows the absorption coefficient of various metals at different wavelenghts. Most solid state lasers like Nd:YAG lasers and fiber lasers have a wavelength of about 1 μm, being more suited to process most metals [87]. A CO_2 laser has a wavelength of about 10 μm and is therefore a more appropriate laser for the processing of polymers rather than metals. It must be noted that the absorption coefficient for metal powders is generally higher than for corresponding bulk material, due to the internal reflections inside the powder bed [154].

As a last important laser parameter, two different modes for laser operation exist, namely continuous and pulsed **operation mode**. Pulsed laser mode can only be achieved by pulsed switching of the pumping medium (e.g. flash lamps), or by placing a Q-switch module inside the laser cavity, functioning as a kind of shutter while opening and closing at very high frequencies. The Q-switch prevents the optical feedback in its closed state, while the active medium is still being pumped and the electrons jump to a higher energy state. As soon as the Q-switch is opened, the emission of photons takes place, resulting in a high energy laser pulse. Although the mean power of a Q-switched laser is not larger than its continuous equivalent, nanosecond pulses with very high peak powers can be created. Pulsed lasers are used in Selective Laser Erosion, or the hydrid process of Selective Laser Melting and Selective Laser Erosion (SLE) [183]. Some work has been reported on SLM with lasers operating in pulsed mode [1, 112]. This thesis work is focused solely on the SLM process where lasers are operated in continuous mode.

Besides the laser parameters, the composition of the **atmosphere** is also of great importance, as the material in its liquid state can react with elements in the atmosphere. In general, preference is given to an inert gas like argon. For materials who are not inclined to form nitrides, the use of a protective atmosphere like nitrogen is sufficient, and more cost-friendly. However, one must keep in mind that the use of a different gas can also have other implications: Ar gas is heavier, more viscous and thermally insulating compared to N_2 [36]. The absolute pressure in the atmosphere influences the amount of evaporation that occurs during processing [137]. The lower the pressure in the build chamber, the more material will be evaporated. Partial (only a few alloying elements) evaporation can take place, leading to changes in the part's chemical composition and resulting part properties. Moreover, the vapor deposition on the optical components in the build chamber is detrimental for the hardware setup [105]. Besides the atmosphere's composition and absolute pressure, also the temperature inside the build chamber influences the process. The temperature of the gas, the powder bed and the baseplate influence the entire heat extraction profile during processing. In a high ambient temperature, thermal gradients are lower and less energy is needed to fully melt the powder. However, hardware problems might occur at high ambient temperatures (thermal expansion, optics, ...), the powder bed might start to sinter together or the material might undergo an unwanted heat treatment.

Material Parameters

Modeling of the SLM process is extremely complex not only due to the great variety of thermal, mechanical and chemical phenomena taking place, but also metallurgically. The presence of three aggregation states (solid, liquid, vapour) makes the process complicated to understand and analyze, let alone model and simulate. Consequently, a very long list of material properties influences the different process aspects in their own way. While previous work at the University of Leuven gives a detailed overview of these material properties and their role in the SLM process [150][137], this section will only give a brief overview of the material parameters with the most relevance to this thesis work. A summary is made in Table 1.4, at the end of this chapter.

Since SLM is a powder-based process, an extra factor of complexity is added, compared to using bulk material. The powder characteristics define to a great extent the final part quality. In order to deposit a homogeneous powder layer with a high packing density, the **particle shape**, **particle size** and **particle size distribution** should be carefully selected. A spherical particle shape (resulting from a gas atomization process) is preferred, because of the flowability of the powder and the attainable packing density. The packing density can also be improved by using very small powder particles, however that is not always favorable concerning safety regulations and flowability. The upper limit of the particle size is determined by the layer thickness. In order to obtain a smooth layer with a maximum packing density, a bimodal size distribution with a ratio of 1 to 7 is favorable [72]. A trade-off must be made since a wide range of powder particle sizes leads to a higher packing density, while a smaller range leads to a better flowability [104].

The **absorptance** A_{abs} determines the amount of energy of the laser radiation which is absorbed. Whereas often in literature the absorptance for bulk material is given, keep in mind that the absorptance for powder is about twice as high due to the scattering of the laser light between the powder particles [137][87].

During heating of the material, most of the heat is transferred to the surrounding environment through convection, conduction and radiation. This is why material-specific heat transfer parameters are very relevant to the process behaviour. The **thermal diffusivity** a_{therm} determines how rapidly a material accepts and conducts thermal energy, and is defined as:

$$a_{therm} = \frac{\lambda_{therm}}{c_p \rho} \left[\frac{m^2}{s}\right] \tag{1.8}$$

with λ_{therm} the **thermal conductivity** (the rate in distance and temperature at which heat flows through a material), ρ the **part density** (mass per unit volume) and c_p the **specific heat capacity** (the energy required to raise the temperature of 1 kg of material by 1K at a constant pressure). Note that the thermal conductivity for powder is much lower than that of bulk material, due to the isolating effect of the air entrapped between the powder particles. The **convection coefficient h** describes the heat flow per unit area and per temperature difference between a solid and a fluid. And finally **the emissivity**

ϵ is the amount of radiated energy compared to the heat radiated from an ideally black body.

As high temperature gradients arise during the SLM process, high thermal stresses may arise, which are determined by the material's mechanical properties and their **thermal expansion coefficient** α. Chapter 7 will elaborate on the effect of thermal stresses in SLM parts.

1.2.4 Melt pool formation

The SLM process depends on adding material by melting powder particles to form a liquid melt pool on top of previously solidified material. Therefore, the process is very dependent on the shape and size of the melt pool. This subsection discusses some influential parameters for the formation, dynamics and heat transfer (consolidation) of the melt pool.

Wetting

The wetting behavior of a liquid on a solid is defined by the **contact angle** θ, as depicted in Figure 1.9. When the contact angle is low, there's a good spread of liquid over the solid. The contact angle is determined by the **surface tensions** associated with the solid-vapor γ_{SV}, the liquid-vapor γ_{LV} and the solid-liquid γ_{LS} interface through Young's equation given in 1.9.

$$cos\theta = \frac{\gamma_{SV} - \gamma_{LS}}{\gamma_{LV}} \tag{1.9}$$

The equation holds for a smooth surface at a constant temperature and constant pressure, however in the SLM process, the surface is not perfectly smooth. There is a top surface roughness leading to the actual contact angle that differs from the theoretical one.

Besides that, the SLM process includes more complexities since the liquid and solid consist of the same material [41], and because different phenomena take place simultaneously: heat transfer, fluid flow, solidification, melting, ...

Balling

Balling is defined as the fragmentation of the melt pool into droplets due to capillary instability and surface tension. It occurs when the total surface of

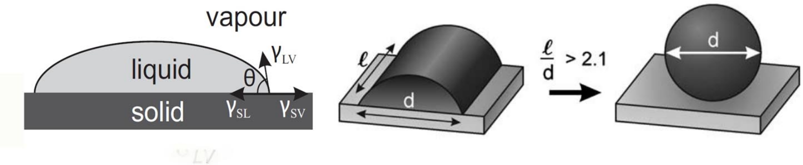

(a) (b)

Figure 1.9: (a) Wetting of a liquid on a smooth, solid substrate as described by the equation of Young with γ_{SV} , γ_{LS} and γ_{LV} the surface tensions associated with respectively the solid-vapor, the solid-liquid and the liquid-vapor interface. (b) Transition from half cylinder to sphere , depending on the dimensions of the melt pool. [84]

the melt pool becomes larger than that of a sphere with the same volume, as demonstrated in Figure 1.9b [84].

The instability criterium according to Plateau-Rayleigh states that a circular cylinder of liquid becomes unstable when an axial harmonic disturbance of its radius has a wavelength less than the circumference of the cylinder (equation 1.10).

$$\frac{\pi D}{L} \geq 1 \tag{1.10}$$

For a melt pool that partially penetrates the underlying layers or substrate, the liquid is only a segmental cylinder (which has a cross section as a circular segment), and the stability condition changes, as deducted by Yadroitsev et al [180], and given in equation 1.11, with symbols as indicated in Figure 1.10.

$$\frac{\pi D}{L} \geq \sqrt{2}\sqrt{\frac{\phi(1+cos2\phi)-sin2\phi}{2\phi(2+cos2\phi)-3sin\phi}} \tag{1.11}$$

Note that this last equation only holds for $\phi > \frac{\pi}{2}$; for $\phi < \frac{\pi}{2}$, the segmental cylinder is always stable. For $\phi = \pi$, the cylinder is circular again, and the stability condition is $\frac{\pi D}{L} \geq \sqrt{\frac{2}{3}}$. This latter condition differs from Plateau-Rayleigh because this cylinder is still attached to the substrate by one line.

Furthermore, it can be seen from Figure 1.11 that the stability region increases for a larger contact width. As a result, the stability of the melt pool can be improved by reducing the length-to-width ratio of the melt pool or by increasing the contact width.

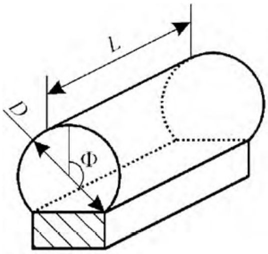

Figure 1.10: Segmental cylinder of a liquid on a substrate [180].

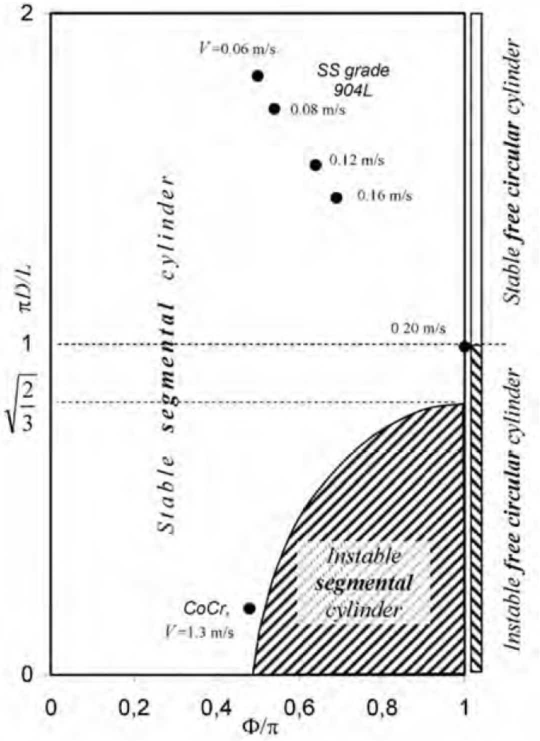

Figure 1.11: Stability map for segmental and free cylinders. [180]

Marangoni flows

For SLM, typically radial temperature gradients $\frac{\Delta T}{\Delta x}$ in the order of 10^2-10^4 K/mm develop between the center of the melt pool and the cooler solid/melt interface. Since the surface tension is temperature-dependent, surface tension gradients arise and convective flows are caused, called Marangoni flows. The strength of these Marangoni flows is defined by the Marangoni number M_a, of which the equation is given in 1.12.

$$M_a = \frac{d\gamma_{LV}}{dT} . \frac{\Delta T}{\Delta x} . \frac{L^2}{\eta . a_{therm}} \tag{1.12}$$

with γ_{LV} the surface tension of the liquid/vapour interface, L the length of the melt pool and η the viscosity. For laser melting processes, this Marangoni number varies between 10^3 and 10^6 [65]. The sign of the Marangoni number indicates the direction of the flow, and thus the shape of the melt pool, as illustrated in Figure 1.12. When the surface tension gradient is negative, a wide and shallow melt pool is formed. A rather deep melt pool is formed when the surface tension gradient is positive [109].

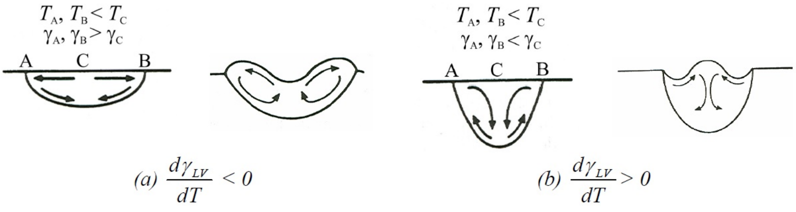

(a) $\frac{d\gamma_{LV}}{dT} < 0$ (b) $\frac{d\gamma_{LV}}{dT} > 0$

Figure 1.12: Schematic diagram illustrating Marangoni flow due to a temperature gradient in a liquid pool for a material with (a) negative and (b) positive surface tension gradient.

Consolidation

Like in all consolidation processes, the part microstructure is determined by the solidification process. Due to the high thermal gradients in SLM, non-equilibrium solidification conditions exist. Moreover, the laser beam is a moving heat source, causing the solidification variables to vary along the melt pool border.

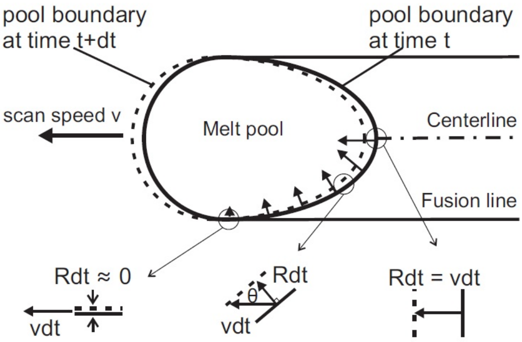

Figure 1.13: Variation in growth rate along the melt pool boundary [150], after [79].

Solidification takes place by cooling of the liquid melt pool below its equilibrium liquidus temperature. Besides that, also the temperature gradient $\overrightarrow{G}$, the growth rate $\overrightarrow{R}$ and the chemical composition of the alloy influence the resulting microstructure.

The **growth rate** $\overrightarrow{R}$ is the rate at which the solid/liquid interface travels in the melt pool. Its direction is therefore always perpendicular to the interface. Because the heat source is moving at scan speed v, the melt pool is elongated and the growth rate varies along the melt pool. Assuming a steady state condition, the absolute value of the growth rate $\left|\overrightarrow{R}\right|$ can be expressed in function of the scan speed vector $\overrightarrow{v}$:

$$\left|\overrightarrow{R}\right| = \overrightarrow{v}.\overrightarrow{n} = |\overrightarrow{v}|\, cos\theta \tag{1.13}$$

with $\overrightarrow{n}$ as the normal to the melt pool border and θ is the angle between $\overrightarrow{n}$ and the scan speed $\overrightarrow{v}$. A schematic illustration of these vectors is shown in Figure 1.13. This results in a growth rate that is maximal in the center line of the melt pool and approaches zero near the fusion line because the growth rate becomes perpendicular to the scan direction.

The **temperature gradient** $\overrightarrow{G}$ determines the heat extraction needed for solidification. Because SLM employs a high energy-density laser source, the heat is concentrated in a very small volume, surrounded by a large colder environment. This results in temperature gradients up to 10^6 K/m. The

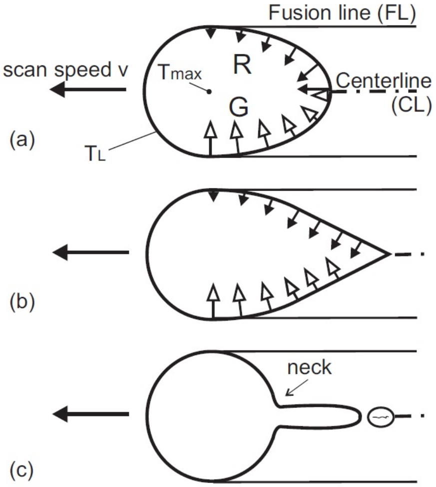

Figure 1.14: Different melt pool shapes at different scanning speeds: (a) elliptical shape at low speed (b) teardrop shape at high speed (c) unstable melt pool at very high speed. [150], after [108].

maximum temperature T_{max} is reached in the middle of the melt pool, as indicated in Figure 1.14. The border of the melt pool is at liquidus temperature T_L. The distance from the maximum temperature to the liquidus temperature is biggest at the center line, making the temperature gradient smallest there. The biggest temperature gradient is where the distance between T_L and T_{max} is smallest, thus on the fusion line.
Combining the thermal gradient $\overrightarrow{G}$ and the growth rate $\overrightarrow{R}$ into one figure (Figure 1.14) shows that as the growth rate increases from the fusion line towards the center line, the temperature gradient decreases.

Due to the lower heat dissipation near the centerline compared to near the fusion line, the **melt pool shape** differs at different scan speeds. The melt pool elongates at higher scan speeds, and at a critical speed, the heat can not be dissipated sufficiently fast, and a tear-drop shaped melt pool is formed as shown in Figure 1.14b. The transition from elliptical to tear-drop shape depends on the material's heat conductivity and heat capacity. The angle $\overrightarrow{\theta}$ between the melt pool border does not reach zero at the back of the melt pool, but it reaches a minimal value, which depends on the scan speed. At even higher scan speeds, the melt pool will form an unstable tail and even result in isolated

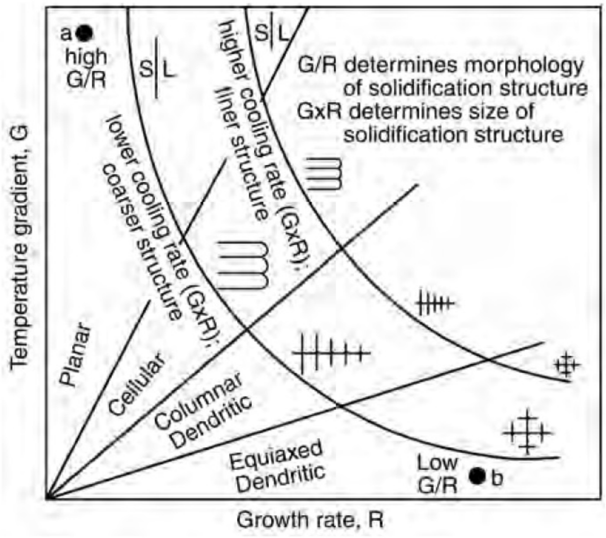

Figure 1.15: The effect of temperature gradient G and growth rate R on the morphology and size of the solidification [79]

molten regions, depicted in Figure 1.14c.

Both the **mode** and the **scale of solidification** are determined by the growth rate $\overrightarrow{R}$ and the thermal gradient $\overrightarrow{G}$. The ratio of $\frac{G}{R}$ determines the mode of solidification. When $\frac{G}{R}$ is very high, a planar solidification mode is formed, with the growth direction perpendicular to the solid/liquid interface and opposite to the heat flux. As the ratio of G to R decreases, the planar solidification front destabilizes and surface pertubations grow out into parallel cells. A group of cells with the same crystal orientation form a grain. Also the lateral surface of the cells might become unstable upon further decrease of $\frac{G}{R}$, resulting in columnar dendrites, which have secondary or higher order side branches. At the very lowest G to R ratio, equiaxed dendrites form, in which every equiaxed dendrite forms a single grain. Between celullar and dendritic solidification mode, a cellular-dendritic mode can be defined. The effect of the temperature gradient G and growth rate R on the solidification mode are depicted in Figure 1.15. In welding of Aluminum alloys, the effect of the solidification mode on tensile properties has been shown [5].

Whereas the ratio of G to R defines the mode of solidification, $G \cdot R$ represents the cooling rate and gives an indication of the size of the solidification structure.

The cell size or dendrite arm spacing is defined by the local solidification time t_F, as given in equation 1.14 where $\Delta T'$ is the non-equilibrium solidification temperature. A shorter solidification time reduces the diffusion length of the solid in the liquid, resulting in a finer substructure.

$$t_F = \frac{\Delta T'}{(G \cdot R)} \tag{1.14}$$

Combining the effect of thermal gradient G and growth rate R on the mode and scale of solidification into one diagram, results in Figure 1.15. The straight lines for constant $\frac{G}{R}$ indicate the different solidification modes, varying from planar to equiaxed dendritic. The hyperboles for constant G $\cdot$ R represent the influence of G and R on the size of the solidification structure.

Parameter	**Symbol**	**Unit**	**Description**
Powder parameters			
Particle shape	/	/	Determines the packing density and flowability.
Particle Size	$d_{v,x}$	μm	Particle diameter for which x vol% of the particles is smaller.
Particle Size Distribution	/	/	Determines the packing density and flowability.
Packing density	ρ_{pack}	%	Indicates the amount of air trapped in the powder volume.
Heat absorption and transfer			
Absorptance	A_{abs}	/	The amount of input energy that is absorbed.
Thermal diffusivity	a_{therm}	m^2/s	Determines how fast a material accepts and conducts heat.
Thermal conductivity	λ_{therm}	W/mK	The rate in distance and temperature at which heat flows through a material.
Specific heat capacity	c_p	J/kgK	The energy required to raise the temperature of 1 kg of material by 1K at a constant pressure.
Convection coefficient	h	W/m^2K	The heat flow per unit area and per temperature difference between a solid and a fluid.
Emissivity	ϵ	/	The amount of radiated energy compared to the heat radiated from an ideally black body.
Melt pool formation			
Contact angle	Θ	°	Determines the wetting of the melt pool.
Surface tension	γ_{SV}, γ_{LS}, γ_{LV}	J/m^2	Determines the shape of the melt pool.

Table 1.4: Overview of the most relevant material parameters.

Chapter 2

Scientific Objectives

This second chapter gives an overview of the current state-of-the-art in SLM, and what the major limitations are, refraining the technique from further evolving as an established process in the production industry. In section 2.1 several roadmaps defined by international experts all over the world are compared. It is through these roadmaps that a clear perspective is given into what should be prioritized in the field of Additive Manufacturing research and development. It is shown that the objectives for most roadmaps concur. In the second section 2.2, a more in-depth description is given of the current limitations and drawbacks of the SLM process, that have restrained it from overcoming the barriers defined in the international roadmaps. The overall goal of this thesis work is defined in such a way that it contributes to overcome the most important barriers in SLM like thermal stresses and processability of highly reflective materials. Section 2.3 gives an overview of the current state-of-the-art in these developments: which materials are processed, how thoroughly they have been characterized and which solutions have been proposed?

There is significant need for research to overcome the major problems and barriers in Selective Laser Melting. This is why, the overall objective of this thesis is defined as followed:

The overall goal of the thesis is to expand the materials palette in an empirical way, with high-demand materials fulfilling the prerequisites like full density and conventional mechanical properties. Along the way, barriers need to be overcome that characterize the SLM process, but prohibit it from reaching a higher technology readiness level, like thermal stresses, cracks and poor dimensional accuracy.

The scientific question to be answered is: What are the similarities and differences in processing different materials by SLM and is there a way to fasten the parameter optimization process?

2.1 Barriers in SLM

To identify the main shortcomings of Additive Manufacturing in general, and to find the bottlenecks that prevent AM from becoming a major player in production industry, roadmaps were defined all over the world by internationally renowed experts in AM. The goal here is to compare some of the most influential roadmaps to find the common denominators and really pin down the most important barriers in AM and SLM.

- Roadmap for Additive Manufacturing: Identifying the Future of Freeform Processing, Dave Bourell et al. (United States) Roadmap defined by 65 experts from industry and academia [18]
- Additive Manufacturing: Strategic Research Agenda - A Future Vision for AM, authors from the AM platform, Europe [149]
- Additive Manufacturing Technology Roadmap for Australia, Wohlers Associates [173]
- Generic Roadmap for AM spare parts market, W.J. de Wolf, within the framework of the FP7-project 'Direct Spare' [43]
- Roadmap for AM in Flanders, T. Craeghs, within the framework of the SIM-program 'STREAM' [22]

All roadmaps agree that capturing the full benefit of AM and overcoming current barriers, which prevent AM from breaking through on a larger scale, requires a more in depth understanding. These barriers are categorized into three groups, as indicated in Figure 2.1;
i) Barriers for material production,
ii) Barriers for launching AM as a mainstream manufacturing technology for part production,
iii) Barriers for production of advanced machine tools in AM.

Comparing the different roadmaps, a priority level can be set for the different barriers. It shows that the most important barriers to overcome are:

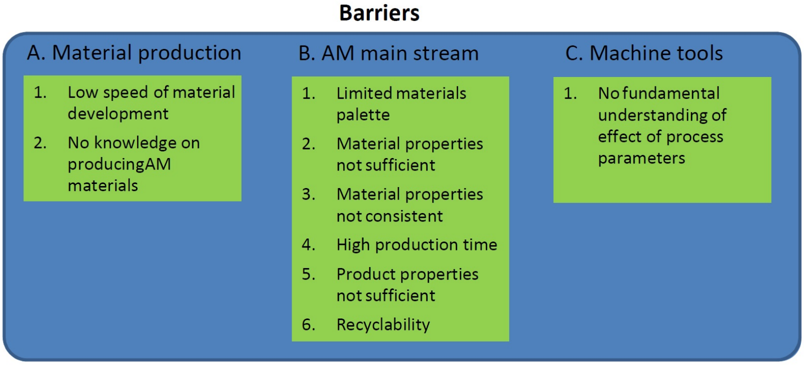

Figure 2.1: Barriers to overcome to achieve the industrial roadmap that was set-up for Flanders. [22].

- *Barrier A1: High lead time for material development.* There is a need to reduce the lead time of material development for AM. Screening methodologies are needed for advances manufacturable materials to answer the question why some materials are processable by AM and some are not.
- *Barrier B1: Limited material palette.* Currently, roughly 15 metallic materials are available for usage in structural applications. At the beginning of this thesis work, it was only about 8 metallic materials. There is still a very strong industrial demand for other materials with mechanical properties comparable to those of conventionally produced parts.
- *Barriers B2 and B5: Material and part properties not sufficient.* Both material properties and part properties do not comply with industrial standards. For instance: fatigue behavior of Ti6Al4V is not sufficient for use in aerospace, surface roughness of SLM parts is too high, residual stresses cause deformation or cracks, ...
- *Barrier B4: High production time.* The cost of the production process is too high, which is mainly caused by the low production speed. The maximal production speed is however often function of material behavior. For instance, faster scanning increases the thermal stresses in the material, due to higher cooling rates.

The focus of this thesis is to contribute to overcome these barriers, primarily focusing on barrier B1. Barriers A1, B2 and B5 will also be handled for a limited set of materials. Barrier B4 is not the focus of this thesis work, but will be taken into account during interpretation and discussion of results.

2.2 SLM process limitations and drawbacks

In order to find a way to overcome the general barriers as defined in the roadmaps above, a more in-depth analysis has to be made to find the core of the problem. In the following subsections, some of the most detrimental limitations and drawbacks of the SLM process are elucidated. These are the problems that will be analyzed and eliminated or compensated for in this thesis, in order to reach the higher goals, defined in the barriers above.

2.2.1 Porosity leading to bad mechanical properties

The SLM process distinguishes itself from the SLS process as it fully melts the powder particles, instead of merely sintering them together. As a result, nearly fully dense parts can be produced by SLM. However, any remaining porosity can severely deteriorate the part's mechanical properties, like ductility or crack propagation. This is why part density is the main physical property to be optimized in this work.

Although the achieved density in SLM is relatively high (> 97 %) , reaching 100 % density is still very difficult by merely optimizing process parameters like laser power, scan speed and scan spacing. An in-depth evaluation of the remaining porosity is needed to determine its cause and to find a proper solution for every type of porosity.

2.2.2 Stresses and cracks

Another major problem encountered in SLM is related to high thermal gradients due to full melting, fast solidification and further cooling to room temperature in a very short amount of time. Stresses are built up throughout the layers and can lead to cracks when reaching values higher than the material's yield strength [171]. Also, the loading capacity of the final part can be reduced by residual stress pre-loading. Therefore, special measures need to be taken to avoid cracks or delamination from the baseplate [143].

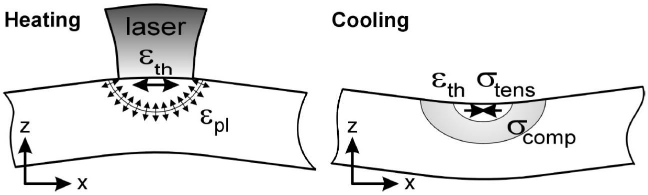

Figure 2.2: The Temperature Gradient Mechanism (TGM) as applied in laser bending processes [164].

Cause of residual stress

Residual stresses are stresses that remain inside a material, when it has reached equilibrium with its environment. Laser based processes in general are known to induce large residual stresses, because of the large thermal gradients that occur when using a high-intensity laser beam. In processes like laser bending, these stresses are used for their advantage, to deform sheet metal plates into their desired shape [46, 164].

Two mechanisms cause the formation of residual stresses in SLM parts. The first is similar to the Temperature Gradients Mechanism (TGM) in laser bending [164]. A scheme hereof is given in Figure 2.2. Due to the rapid heating of the upper surface by the laser beam and the rather slow heat dissipation (low heat conduction), a steep temperature gradient develops across the thickness of the plate. Since the expansion of the heated top layer is restricted by the underlying material, elastic compressive strains are induced. When the material's yield strength is reached, the top layer will become plastically compressed. In absence of mechanical constraints, a counter bending away from the laser beam is observed. During cooling the plastically compressed upper layers start shrinking and a bending angle towards the laser beam develops.

In the SLM process however, the baseplate forms a constraint, and thus the built up material won't bend in a concave or convex way. Also note that in SLM a liquid, and thus stress-free melt pool is formed. The Temperature Gradient Mechanism from laser bending has some similarities with the mechanism in SLM, but is not entirely the same. In chapter 7, a better approach to the SLM process will be made.

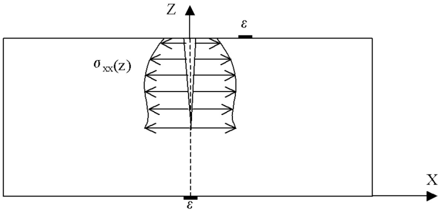

Figure 2.3: Schematic representation of measurement by the Crack Compliance Method [105].

A second mechanism causing residual stresses in SLM parts, is the cool-down phase of the melted top layers. Thermal expansion and contraction cause material shrinkage upon cooling. The shrinkage is prohibited by the underlying layer, causing tensile stress in the added top layer.

Measuring residual stresses

Up to today, there is no clear non-destructive way to quantify residual stresses in SLM parts. A few methods that were explored in previous research are summarized in this paragraph.

A **first method** is the Crack Compliance Method (CCM) [132, 121]. It is based on the part deformation after stress relief. Figure 2.3 shows a sample with an unknown stress distribution. One or more strain gauges are attached to the sample in known positions (indicated as ϵ in Figure 2.3). During measurement, the part is cut in half by Electric Discharge Machining (EDM), in small subsequent steps. After each step, the strain is measured in every strain gauge. The total stress profile is divided into a set of basic functions, for each of which the resulting strain can be calculated using the Finite Element method. From the measured total strain the actual residual stress profile can be calculated.

This method was validated for some test cases, but still has some drawbacks to be taken into account. Most importantly, it is a destructive measurement as the parts are cut by EDM. Furthermore, stresses are only measured in the position of the cut and it is unknown how much stress the EDM process itself induces.

A **second method** for stress measurement is by X-Ray Diffraction (XRD) [49, 122]. X-ray diffraction can be used to measure residual stress using the distance between crystallographic planes, i.e., d-spacing, which depends on the strain. When the material is in tension, the d-spacing increases and, when under compression the d-spacing decreases. Stresses can be determined from the measured d-spacings. X-rays diffract from crystalline materials at known angles 2θ (as indicated in Figure 2.4) according to Bragg's Law:

$$n\lambda = 2dsin\theta \tag{2.1}$$

where n is the order of diffraction, λ is the wavelength of the X-ray beam, d is the distance between lattice planes inside the material and θ the angle of the diffracted beam.

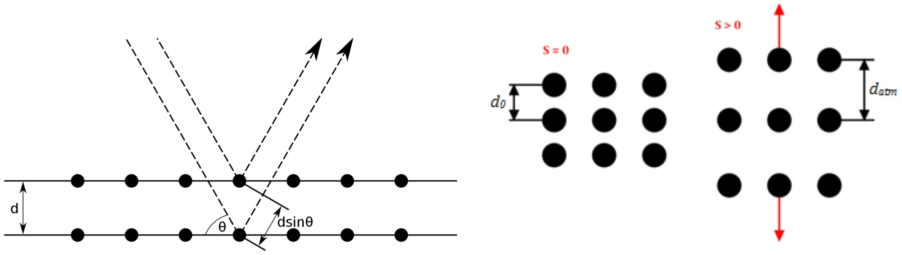

Figure 2.4: Working principle of XRD according to Bragg's law (left) ; Indication of a shift in lattice planes due to stresses. (right) [19]

The downside of this measurement technique is that the size of the test samples is limited, and stresses are only measured at the part's top surface.

Reducing residual stresses

There are several ways to either reduce the residual stresses, or to minimize the consequences:

- One way to reduce stress related problems is to decrease the thermal gradients that occur. This can be done by pre-heating the baseplate. A residual stress model by Shiomi et al. showed that theoretically, by heating the baseplate up to 250° the residual stress can be reduced to less than 50 % [143].
- Another method to reduce residual stress levels and/or part deformation is to divide the scanned area in a grid of small zones that are scanned in a random order [159]. This scan strategy was patented by Concept Laser GmbH and is called the 'island scanning strategy' [63]. The total surface to be scanned is divided into smaller squares, which are scanned

in a zigzag manner. The scan track in the adjacent squares are scanned, rotated over 90 degrees. A clarifying sketch is depicted in Figure 1.7.

- Shiomi et al. indicated with a theoretical model on residual stresses in SLM parts, that residual stresses can be reduced by 55% by remelting [143]. This hasn't been validated, but will be investigated in the course of Chapter 7 of this work.
- A post-process stress relief heat treatment also reduced or even eliminates the residual stresses in a part. The part is heated in a furnace, while still attached to the baseplate. Stress-relief heat treating is a uniform heating to a suitable temperature below the transformation range, holding at this temperature for a predetermined period of time, followed by uniform cooling. Care must be taken to ensure uniform cooling, particularly when a component is composed of variable section sizes. If the rate of cooling is not constant and uniform, new residual stresses can result that are equal to or greater than those that the heat-treating process was intended to relieve [8, 14].
- Besides the use of a baseplate, which avoids thermal deformation in SLM, support structures can also be added to a three-dimensional CAD model, to prevent the part from warping up during production [69]. The support structures are often designed or built in a more fragile way, so they can be easily removed afterwards. The resulting support structures should still have sufficient mechanical properties to withstand the deposition system and to evacuate heat.

2.2.3 Dimensional accuracy

A third important issue in the field of SLM processing is the accuracy and surface quality of SLM parts which is still lagging behind at conventional manufacturing technologies. Due to the nature of the process, some layer-wise dimensional effects like the **stair-stepping effect** (Figure 2.5) are inevitable [53]. The stair-stepping effect can be minimized by reducing the layer thickness, or applying laser erosion as a finishing step [183].

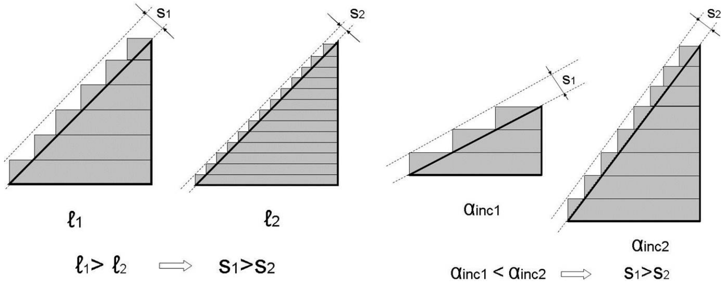

Figure 2.5: Illustration of the stair-stepping effect, as a function of the layer thickness (left) and the slope angle (right) [183].

While SLM provides a nearly complete freedom in design, an important limitation is the manufacturing of **downfacing surfaces**, also defined as 'overhang' or 'bottom surface'. Downfacing surfaces are supported by loose powder instead of solidified material.

Since the heat conductivity of the underlying powder bed is very small compared to bulk material, the conductive heat transport is less, resulting in an overheated melt pool, that consequently becomes too wide and too deep. Subsequently, the melt pool sinks in the loose powder due to gravity and capillary forces, leading to dross formation and resulting in a very poor surface quality and geometric deviations. Moreover, stresses are easily built up and warpage can occur, preventing any new powder layer deposition. A possible solution is to add support structures underneath the downfacing area, as shown in Figure 2.6. Other solutions are proposed further on in this work, in chapter 4.

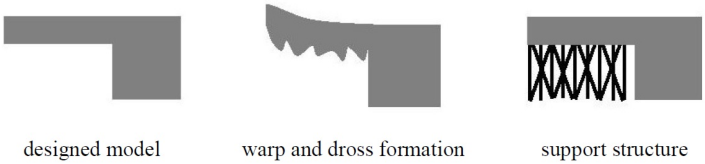

Figure 2.6: The placement of support structures underneath downfacing structures [159].

2.3 State-of-the-art

At the outset of this PhD work, the materials palette for Selective Laser Melting was limited to just a few materials, mainly stainless steel, Ti6Al4V, CoCr, and some Nickel based alloys like Inconel.

Stainless steel was one of the first materials to be fully qualified for use in SLM. Ruidi Li et al. performed a brief investigation on the influence of laser power, scan speed, scan spacing and layer thickness on the density of stainless steel 316L parts. It was shown that gas atomized powder results in a higher density than water atomized powder because of the lower oxygen content and better sphericity, that leads to higher powder packing [93]. The experimental studies on the influence of different processing parameters were also done by Yadroitsev et al. for stainless steel 904L [179], and by Meier et al. for 316L [103], where the part density reached 99 %. Also the mechanical properties of stainless steel 316L were tested in this work, and it was concluded that the part's strength is comparable to conventionally produced parts, but the ductility is much lower. Xue et al. reported similar results on Laser Cladding, where the 316L stainless steel parts had a higher yield strength compared to cast or wrought material, while the ultimate strength and elongation were comparable [178].

Yadroitsev et al. reported on the surface morphology in SLM of stainless steels, and emphasizes the importance of scan spacing and stable scan tracks [181]. In addition, there was also a publication by Yadroitsev et al. on single track formation in SLM of several metal powders, like stainless steel 316L and 904L, but also tool steel H13 and inconel 625 [180]. In the latter work, the emphasis is on the physical phenomena that take place during processing. A model by Gusarov et al. also shows great insights into the heat transfer during the interaction of the laser beam with the 316L stainless steel powder material [57]. The University of Leuven also reported several publications on the basic understanding of melt pool formation [138] and complicating process phenomena like balling and residual stress when processing stainless steel alloys [84][106].

Besides stainless steel and iron-based alloys, **Ti6Al4V** and CoCr have also been leading materials in the research of Selective Laser Melting, because of their bio-compatible nature. Vandenbroucke et al. described in [160] the parameter optimization to obtain nearly-full dense parts in both materials, and performed initial mechanical tests like hardness tests and tensile tests. A more in-depth characterization of the microstructural evolution during SLM of Ti6Al4V was reported by Thijs et al. [153] and a similar range of crystallographic phases was detected by Murr et al. [114]. Murr et al. compared both the Electron Beam Melting process and the SLM process of Ti6Al4V and concluded that their mechanical behavior is similar to and superior to conventional wrought or cast Ti6Al4V products.

To a lesser extent, initial tests were performed on new materials like silver [52], gold [70], copper [130] and magnesium [116], none of which have shown the ability to produce nearly fully dense parts.

Selective Laser Melting of aluminum alloys has proven to be much more difficult, due to the high reflectivity and heat conductivity of the material, on top of the rapid formation of an adherent oxide on any exposed surface. Louvis et al. performed some initial tests on SLM of Al6061 and AlSi12, showing that indeed the formation of oxide films on both solid and liquid metal surfaces leaves oxide residu between the scan tracks. This leads to porosity of over 10 %. To avoid this porosity, the authors recommend that the SLM process must break up these oxides, or avoid the formation of them [96]. Meanwhile, a research group in Nanyang Technological University also started the initial research on SLM of another aluminum alloy: AlSi10Mg. In [95] they indicate that the achievable density is 99.9 %, but that the surface roughness still needs a lot of improvement, by for instance sandblasting. The results however are based on one produced cube, and thus must be interpreted with care.
In parallel with this PhD work, many other research groups saw the urgent need for Additive Manufacturing of aluminum alloys, as can be seen from the numerous publications in the last four years. This emphasizes the important demand for a broader material palette in SLM, and more specifically for aluminum alloys. The results of other research groups will be critically compared to the ones in this work in chapter 4.

The production of fully dense **tool steel** parts has also proven to be challenging, due to the formation of cracks resulting from thermal stresses. For H13 tool steel, the problem of crack formation is less pronounced, because of the relatively ductile nature of the material, compared to other tool steels. Several publications indicate the possibilities of producing high density parts in H13 tool steel [32, 128].
The use of **M2 tool steel** for SLM as a steel with a higher hardness than for instance H13 tool steel, encounters the problem of crack formation due to high thermal stresses. The work of Childs et al. showed that the formation of a stable, crack-free single line track is possible in M2 tool steel, and a process window is defined for low scan speeds and low laser power [31]. Niu et al. [120] showed the influence of scanning parameters on the density of M2 HSS two-dimensional surfaces. Since no three-dimensional parts were built up in

this work, no cracks were formed.

In Abe et al., a dual laser scanning system in which YAG and CO_2 laser beams are offset a small amount from each other is proposed. It is considered that slow cooling or re-heating after melting can eliminate residual stress and improve the part's ductility [2]. The use of a pre-heating system to reduce thermal stresses has also shown its advantages in the work of Alimardani et al. [3], where the residual stresses were reduced by 22 % in a stainless steel wall produced by direct metal deposition, by using a pre-heating up to 800 K. Das et al. at the University of Texas developed a powder bed pre-heating system that reaches up to 1300 °C [40]. Initial tests at pre-heating temperatures of 350°C an 900°C showed that the influence of pre-heating on the wetting behavior is minimal [39].

Numerical models for residual stresses are developed by Shiomi et al. [143] and Mercelis et al. [106]. It is however in measuring and eliminating these stresses that the major shortcomings lie.

Chapter 3

Experimental Set-up and Procedures

This chapter gives a brief but explicit overview of the SLM machines that were employed to build all test parts in this work. The AM-lab in the University of Leuven consists of one machine for SLS of polymers, one for AM of ceramics and four for SLM of metals. Only the three machines that were used in the scope of this thesis are described here in section 3.1. Section 3.2 describes the equipment that was used for material characterization, including density and roughness measurements, macro- and microstructural investigation and mechanical testing.

3.1 SLM machines

Several different SLM machines were operated to produce the test parts in this research. Every SLM machine in the AM laboratory at the University of Leuven (KU Leuven) has different properties and capabilities, making each machine unique and suitable for a special material class. Tool steels were processed on a Concept Laser M3 machine, since its 100 W laser is powerful enough for steels and the machine is suited for implementation of a pre-heating element. An adapted Concept Laser M1 machine is used for processing Aluminum alloys, because this machine is equipped with an inert handling chamber, enabling a safe way to process reactive materials with a higher laser power of 200 W.
In order to have more freedom in research, KU Leuven developed and built its own SLM machine, enabling extensive hard- and software research. This

so called ‘LM-Q machine’ is equipped with a monitoring system, making it possible to do on-line melt pool monitoring and quality control.

3.1.1 Concept Laser M3 Linear machine

The Concept Laser M3 Linear (CL M3) machine is a commercially available SLM machine employing a 100 W diode pumped Nd:YAG laser from Rofin Sinar with a wavelength of 1.064 μm. There are two available aperture settings (big and small), resulting in a laser spot size $\phi_{99\%}$ of 180 μm and 120 μm respectively. The laser can also be used in Q-switched pulse mode for laser erosion, but this function will not be used in this thesis.

The laser beam is deflected onto the baseplate in two directions by a pair of galvano mirrors. The laser scan speed is limited due to the dynamics of these galvano mirrors. In this Concept Laser M3 machine, scan speeds up to 5000 mm/s can be applied.

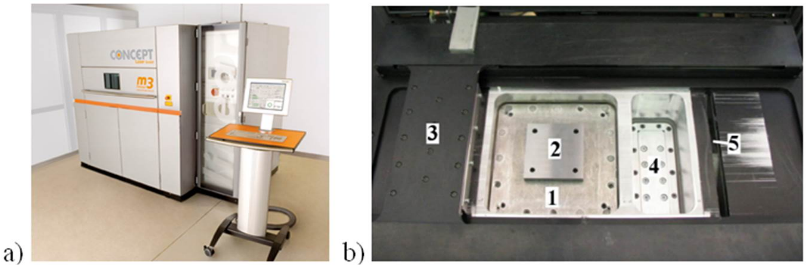

Figure 3.1: a) Concept Laser M3 Linear machine b) cusing module used for SLM with a powder platform(1), a base plate(2), a coater system(3), a powder platform(4) and an entrance to overflow bottles(5) [183]

A general view of the Concept Laser M3 machine is depicted in Figure 3.1. What differentiates this machine from others, is its two different operating modules that can be employed; a "*cusing*" module and an erosion module. Like mentioned before, only the cusing module is used in this research for the production of SLM parts. Its build platform is 250 mm x 250 mm in size. A smaller baseplate of 100 mm x 100 mm is attached on top of it.

The powder deposition system consists of a double steel blade coater, to enable coating from two sides. However, it is also possible to change the deposition settings to coat from only one side.

The lay-out of the cusing module is shown in Figure 3.1. During the SLM build, the cusing module is placed in the machine under a protective argon or nitrogen atmosphere. The chamber is flushed until the remaining oxygen level is below 1 % (for steels). During the entire process, the building chamber is under slight overpressure.

3.1.2 KU Leuven's own-built "LM-Q" : Laser Melting - Quality machine

By developing an own-built SLM machine (Figure 3.2), the University of Leuven gains many research possibilities that commercial machines lack. First, the machine's process chamber is evacuated until vacuum and then flushed with argon. This cycle repeats twice, resulting in a closed machining area with an oxygen level below 0.1 %.
Secondly, because the software was developed at the University of Leuven as well, the laser scanner can be controlled to follow any defined scanning strategy, and not just the limited amount of available strategies on commercial machines. Finally, the LM-Q machine contains a monitoring system, applying a photodiode and a high-speed CMOS camera. This enables online melt pool monitoring and quality control. Dimensional properties like length, width and surface area of the melt pool can be measured, as well as its intensity. By linking these properties to the position of the laser spot at that time, an 'intensity map' can be created, showing the melt pool intensity at every position on the baseplate during scanning. Further details on the monitoring system and quality control during SLM can be found in [33].

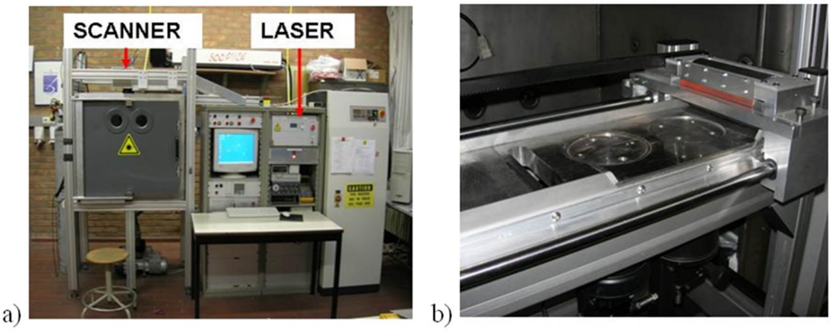

Figure 3.2: a) A general overview of KU Leuven's LM-Q machine; b) The building platform with powder deposition system [183]

3.1.3 Concept Laser M1 (medical) machine

Compared to the Concept Laser M3 Linear machine, the M1 machine (CL M1) has a smaller building platform of 200 mm x 200 mm, but a more powerful fiber laser of 200 W. The laser beam has a wavelength of 1.064 μm and a spot diameter of 150 μm ($\phi_{99\%}$). The Concept Laser M1 machine in the AM laboratory at the University of Leuven is a modified version, in that sense that it is extended with an inert handling chamber, as shown in Figure 3.3. In all other machines in the lab, job preparation and powder handling is done in ambient air. The handling chamber attached to the Concept Laser M1 machine permits the use of reactive powder materials, as the job preparation and powder handling can be done in a protective atmosphere where the oxygen level is kept below 0.3 %.

Figure 3.3: The modified Concept Laser M1 machine at KU Leuven.

An overview of the machines employed in this thesis work is summarized in Table 3.1

	P [W]	v_{max} [mm/s]	$\phi_{99\%}$ [μm]
Concept Laser M3 Linear	100	5000	100 or 180
Concept Laser M1	200	2000	150
LM-Q	300	8000	80

Table 3.1: Overview of the SLM machines that were employed in the scope of this thesis work.

3.2 Material Characterization

3.2.1 Density measurements

Part density was measured in two ways: the main principle is measurement by Archimedes' method. The part density is determined by weighing the sample in air and subsequently in ethanol. The method is fairly fast and simple, but it is not suitable for parts with open porosity and very low density. In those cases, a lacquer is applied to avoid ethanol infiltration.

A second, but more intensive method to confirm the Archimedes density, is by optically checking the part's cross section. Several cross sections are made and first ground and polished before inspection under a light optical microscope (LOM). A software program in Matlab then analyzes the microscope image. Every pixel is compared to a certain threshold value. Every pixel darker than the threshold is considered porosity. Every pixel lighter than the threshold value is interpreted as solid material. In that way, the software calculates the total percentage of porosity in that image.

This technique is only used as a verification for the Archimedes method, since it has some drawbacks and limitations. It is a destructive measuring method and it is very sensitive to changes in the threshold value. The threshold value determines the accuracy of the measurement. For all optical density measurements in this thesis, a fixed and calibrated threshold value was used. Moreover, the porosity is only evaluated in these cross sections, and not in the entire part.

3.2.2 Roughness measurements

To determine the surface quality of a part, roughness measurements are conducted on a Taylor Hobsson Talysurf 120L roughness meter, which has

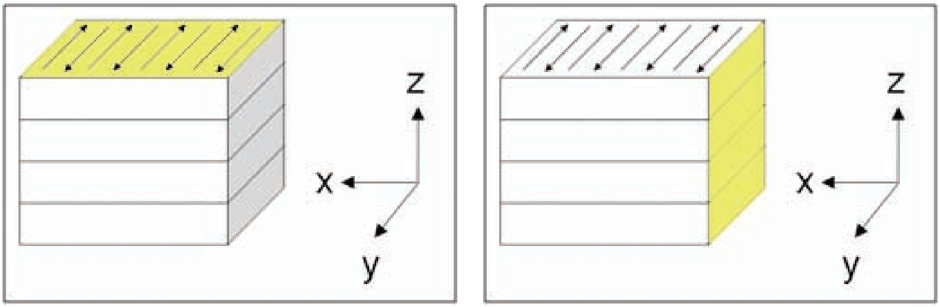

Figure 3.4: Top view is shown in the XY plane, cross sections are shown in the YZ plane.

a diamond stylus with a tip radius of 2 μm. The total evaluation length reaches from 10 mm for the aluminum parts to 15 mm for the tool steel parts. According to ISO standard 4288-1996, a cut-off filter is needed for average roughness values between 2 and 10 μm. Since that is not the case in these tests, no cut-off filter is used and average roughness values are indicated as P_a (primary roughness) instead of R_a. To get a more clear indication of the surface profile, also the peak-to-peak roughness value P_t is measured.

By analyzing multiple two-dimensional lines that are parallel to each other (with a spacing of 0.1 mm), a three-dimensional surface map is created to help visualize the entire surface morphology. In this case, S_a and S_t values are obtained.

3.2.3 Macro- and microstructural investigation

For investigation of the macro- and microstructures, samples were cut along the XY and XZ plane (Figure 3.4) for observation of respectively a top view and a cross sectional view.

Then, they are prepared according to standard techniques of embedding in a thermoharding polymer. After grinding on SiC grinding paper and polishing with a 3 μm and 1 μm diamond suspension, most samples were etched in order to reveal scanning patterns and grain boundaries. The different etchants that were used for the different materials are summarized in Table 3.2.

Material	Etchant	Duration
18Ni300 maraging steel	15 ml H_2O ,15 ml acetic acid, 60 ml HCL , 10 ml HNO_3)	10 s
M2 High Speed Steel	Vilella's	10 s
AlSi10Mg	Keller's Barker's	10 - 15 s 5 s at 5 V
Al 7075	Keller's	10 - 15 s

Table 3.2: Summary of the etchants used for different materials.

Light Optical Microscopy (LOM) images were made on an Axioskop 40 Pol/40 A Pol microscope, while a FEI Scanning Electron Microscope (SEM) XL 40 equipped with a lanthanum hexaboride (LaB6) electron gun and Energy Dispersive X-Ray Spectroscopy (EDX) system was used to make the secondary (SE) and back scattered (BSE) images and the composition measurements. For higher magnifications, the Philips Scanning Electron Microscope XL30 was used. This SEM is equipped with a Field Emission Gun (FEG) and an Edax energy dispersive X-ray Detector for micro-analysis of light elements. The EDX spectrometer is used to quantify the local compositions of the different phases.

Since conductive samples are required, a thin layer of carbon is sputtered on the embedded parts. Another way to make the samples conductive is by removing the thermoharding polymer or to apply a conductive carbon glue circuit.

X-Ray Diffraction (XRD) patterns from the different materials are obtained from a Siemens D500 goniometer with a Cu or Cr tube.

3.2.4 Mechanical testing

To determine the mechanical properties of all materials, several tests like tensile, charpy and hardness tests were conducted on most materials. Flat tensile test parts with a gauge length of 32 mm and a thickness of 5 mm, according to ASTM standard E8 are produced and tested on an Instron 4505 testing machine. A dynamic extensometer was mounted on the samples to measure the elongation during testing.

Micro-hardness was measured according to the Vickers hardness scale. The parts were measured on a Leitz-Durimet apparatus, according to the ASTM E92-65 standard. A 0.5 kg load is used for all materials and at least five indentations are made in each sample. The average hardness and a confidence interval of 95% are calculated. Macro-hardness measurements are performed on the tool steel materials, according to the Rockwell C scale, which employs a 150 kg load that is applied with a conical diamond indentor.

The Charpy impact test was used to determine material fracture toughness by hitting a test specimen with a hammer mounted at the end of a pendulum. The specimen is broken by a single hit from a pendulum that strikes the middle of the specimen on the un-notched side. The height of rise subtracted from the height of fall gives an indication of energy absorption involved in deforming and breaking the specimen [9]. A V-shaped notch is used in the impact specimen in order to control the fracture process by concentrating stress in the area of minimum cross-section. In this study, Charpy tests were done according to ASTM E23-96 standard. Charpy impact test samples were produced with a V-notch and have the standard dimensions of 10 x 10 x 55 mm, conform ASTM E23. They were tested on a Tinius Olsen pendulum impact testing machine.

Although the Young's modulus E can be determined from the tensile test results, a more detailed impulse excitation test (IET) is done for verification on a Grindosonic set-up. Rectangular shapes with a dimension of 50 x 4.4 x 3 mm are tested in two different directions, to measure the flexural mode in-plane and out-of-plane. The corresponding Young's moduli are calculated using the formula according to ASTM E1876-09.

For all mechanical tests, at least three, but usually five test parts were produced and tested, to indicate an average value and a 95% confidence interval.

Part I

Aluminum Alloys

This first part introduces new process capabilities for SLM of two types of aluminum alloys. The first is a casting alloy, commonly denoted according to the DIN standard by AlSi10Mg, or according to the American ANSI denotation as A360.0 (Chapter 4). Its near-eutectic composition makes it possible to process the A360.0 aluminum alloy by laser applications like SLM. However, the high reflectivity of aluminum alloys could lead to problems like reflection and bad absorption. Surplus, aluminum alloys are known for their high thermal conductivity, which might lead to the need for higher laser powers to fully melt the powder particles.

The second alloy, discussed in Chapter 5 is a wrought aluminum alloy 7075 that has been selected for its good combination of high thermal conductivity and high strength. This alloy has a larger solidification range and worse castability, which is expected to result in some difficulties in processing by SLM. The thermal expansion coefficient of this alloy is high which may lead to problems upon heating and/or cooling.

Chapter 4

Cast aluminum alloy A360.0 (AlSi10Mg)

In this chapter, the most relevant material properties are summarized, and a short overview of the challenges in processing this material by SLM is given. In section 4.4, a comparison is made between two batches of powder material based on chemical composition and powder properties. In section 4.5, single track scans are made, in order to determine a process window in which a stable melt pool is formed. By evaluating the single track scans, a lot of information on melt pool formation and stability can be gained [31, 180]. A range of laser powers and scan speeds will be determined for which the formed scan track meets the requirements. Next, the optimal parameter set for the production of almost fully-dense parts will be determined within the previously defined process window. In section 4.7 the microstructure and related mechanical properties of the high-density parts are taken under investigation. In section 4.8, an optimal heat treatment for SLM produced parts is defined, which differs from the standardized heat treatment for this alloy. The final section 4.9 describes some challenges in this material regarding dimensional accuracy, specifically the production of parts with internal channels and downfacing areas. The chapter ends with a summary of the main conclusions in 4.10.

4.1 Introduction

In the ANSI (American National Standards Institute) numbering system for cast aluminum alloys, major alloying elements and certain combinations of elements are indicated by specific number series, as indicated in Table 4.1.

Number Series	Alloy Type
1XX.X	99.0% minimum aluminum content
2XX.X	Al + Cu
3XX.X	Al + Si & Mg, or Al + Si & Cu, or Al + Si & Mg & Cu
4XX.X	Al + Si
5XX.X	Al + Mg
7XX.X	Al + Zn
8XX.X	Al + Sn

Table 4.1: The ANSI numbering system for cast aluminum alloys

In this work, the A360.0 alloy is employed for processing by SLM. As a member of the 3XX.X group, it is an aluminum-silicon & magnesium alloy. Aluminum-silicon alloys are characterized by sound castability, good weldability and outstanding corrosion resistance. Due to their excellent combination of low weight, high heat conductivity and good mechanical properties, these alloys find a large number of applications in aerospace and automotive industries, as well as conventional manufacturing industries. The combination of the material's properties and the advantages of the SLM process, like the high geometrical freedom, can lead to new opportunities in applications that require complex structures and internal cavities like complex heat exchangers or lightweight structures [161]. The relatively low cost of the material also makes it appropriate for metallic prototyping.

4.2 Material Properties

The **chemical composition** of A360.0 aluminum alloy according to ASM handbooks and ANSI is shown in Table 4.2 [75].

The major alloying elements in A360.0 are silicon and magnesium. **Silicon (Si)** is the most important single alloying element in the vast majority of aluminum

	Al	Si	Cu	Mn	Mg	Zn	Fe
wt%	Bal.	9-10	≤ 0.6	≤ 0.35	0.4-0.6	≤ 0.5	≤ 1.3

Table 4.2: Chemical composition of A360.0 aluminum alloy, according to ASM [75]

casting alloys. Silicon is primarily responsible for good castability i.e. the ability to fill dies and to solidify castings without hot tearing or cracking.

The binary Al-Si phase diagram is depicted in Figure 4.1. At 12.5 wt% Si, the alloy is eutectic. The alloys with less wt% Si, like A360.0, are hypo-eutectic. The near-eutectic Si-content in A360.0 results in a small solidification range, which is favorable for processing by SLM.

Besides that, the role of silicon is several-fold:

- silicon improves the alloy's fluidity,
- the more silicon an alloy contains, the lower its thermal expansion coefficient and specific density,
- silicon is a hard phase, leading to a higher wear resistance,
- in combination with other elements, silicon can improve the alloy's strength and hardness.

Adding **magnesium (Mg)** to the Al-Si alloy enables the precipitation of Mg_2Si which significantly strengthens the matrix without compromising other mechanical properties. The maximum useful limit of Mg for hardening corresponds to 0.7 % Mg. The addition of more magnesium can contribute to softening of the matrix [75].
Increasing **copper (Cu)** above 0.6 % lowers the resistance to corrosion, while increasing **iron (Fe)** above 1 - 3 % lowers the ductility.

Heat treating in its broadest sense, refers to any of the heating and cooling operations that are performed for the purpose of changing the mechanical properties, the metallurgical structure, or the residual stress state of a metal product. When the term is applied to aluminum alloys, however, its use is frequently restricted to the specific operations employed to increase strength and hardness of the precipitation-hardenable alloys [8]. Cast products of heat-treatable aluminum alloys have the highest combination of strength and ductility when produced in T6-type tempers. This T6 temper includes three steps:

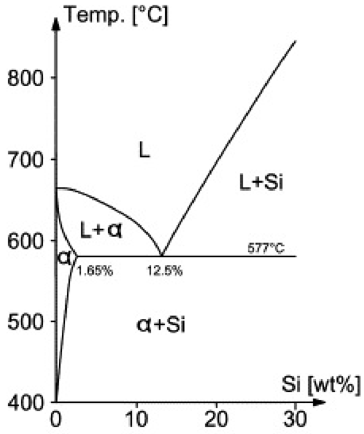

Figure 4.1: The aluminum - silicon alloy phase diagram [115]

1. **Solutioning** : 10 min at 480 - 505 °C : Heating the alloy to a temperature range wherein all of the solute is dissolved, so that a single-phase structure is attained.
2. **Quenching** : in water : To retain the formed single-phase structure at ambient temperatures, rapid cooling is needed.
3. **Aging** : 16 - 24h at 150 °C : Precipitation is achieved by re-heating the alloy below the solvus (T_S) at a suitable temperature for a certain time. During this time, at localized regions (for instance grain boundaries), the precipitates nucleate.

The T6 heat treatment is employed for cast A360.0 parts to increase hardness and strength.

The **physical and mechanical properties** of A360.0 are summarized in Table 4.3. An overview is given of the mechanical properties of conventionally cast [75], high pressure die cast (HPDC) [50], high pressure die cast and T6 heat treated [50] and Selective Laser Melted A360.0, as reported by SLM machine constructor EOS[47].
From the tensile properties of the A360.0 SLM parts that were produced by EOS, it can be seen that the as-built properties exceed or at least meet those of High Pressure Die Cast parts. Buchbinder et al [24] found similar UTS results for vertically built samples (about 420 MPa), but only 360 MPa for diagonally oriented samples and even about half (240 MPa) for horizontally built test bars.

Brandl et al. [20] performed high cycle fatigue tests on SLM built A360.0 parts, showing that the fatigue strength for horizontal oriented parts is higher than for diagonally or vertically built ones. The fatigue limit for as-built parts didn't show any anisotropy at about 100 MPa, but in the T6 heat treated condition however, the fatigue limit for horizontal samples was about double (200 MPa) than for vertical samples (115 MPa).

The physical properties that are reported are those of conventionally cast A360.0 [75]. A360.0 aluminum alloys are lightweight materials (2.68 g/cm^3), compared to for instance pure iron (7.874 g/cm^3) or even M2 Tool Steel (8.16 g/cm^3). In combination with the good mechanical properties, it is a favorable alloy in automotive and aerospace industries.

	Conventionally Cast	**HPDC**	**HPDC + T6**	**SLM (according to [47])**
Young's modulus E [GPa]	71	71	71	70 ± 5
Ultimate Tensile Strength UTS [MPa]	315	300 - 350	330 - 365	445 ± 20
Elongation at break ϵ [%]	5	3 - 5	3 - 5	3.5 ± 2
Hardness Vickers [HV]	86	95 - 105	130 - 133	140
Density ρ [g/cm^3]	2.680			
Solidification Range [$°C$]	595 - 555			
Thermal conductivity λ_{therm} [W/mK]	113			
Thermal expansion coefficient α_L [$10^{-6}/K$]	20.5			

Table 4.3: Mechanical and physical properties of cast, High Pressure Die Cast, High Pressure Die Cast and T6 heat treated, and SLM produced A360.0 aluminum parts (as indicated by SLM machine provider).

4.3 Challenges

Earlier studies on the feasibility of producing Aluminum alloy parts by SLM have shown that the process is more difficult to control than for example in the case of processing stainless steels or titanium alloys [56]. This is mainly attributed to the high reflectivity of the aluminum powder for the laser beam, the high thermal conductivity, and the formation of oxide layers on top of the melt pools [23, 24]. Bulk aluminum reflects about 90 % of the Nd-YAG laser light and this is why a higher laser power input is required to melt the aluminum powder [96]. Furthermore, Table 4.3 indicates the high heat conductivity for aluminum, which is about twice as high as for instance for steels. The heat is conducted away from the melt pool, causing the surrounding material to heat up, instead of melting the powder material. In addition, aluminum has a high oxygen affinity, leading to oxide formation on top of the melt pool. This worsens the wetting behavior and decreases the laser absorptivity [157].

4.4 Powder material comparison

An initial phase of this research includes the comparison of two different A360.0 powder materials. The powders are supplied by LPW [97] and Concept Laser [35] and will further on be referred to as *LPW* and *CL* powder. The main goal here is to characterize the powders, check for quality aspects and find the influence of the powder properties on the processability by SLM.

4.4.1 Chemical Composition

At first, the chemical composition of both powders was determined by ICP-AES measurement and compared to the composition determined by the ISO 3522 standard, see Table 4.4. The measurements show that the LPW powder has a silicon content of only 8 wt%, which is about 1 wt% lower than the CL powder, and out of the range for this alloy according to the ISO 3522 standard [165]. According to the literature, the lower Si content may cause less absorption of laser energy, a lower hardness and a larger difference between solidus and liquidus temperatures which will influence the solidification phenomena [174].

Element	**ISO 3522** [wt%]	**CL powder, based on ICP-AES** [wt%]	**LPW powder, based on ICP-AES** [wt%]
Si	9-10	9.02	8.05
Mg	0.45 - 0.6	0.471	0.542
Fe	<1.3	0.123	0.455
Cu	<0.6	0.006	0.096

Table 4.4: Chemical composition of two A360.0 powders by LPW and by Concept Laser, measured by ICP-AES.

4.4.2 Powder properties

The particle size distribution has an important influence on the powder layer deposition and melting behavior [127]. By both quantitative stereology on the cross section of embedded powder particles and particle size measurements by a Mastersizer measurement machine, the average particle size and the particle size distributions were measured. For CL powder the average particle size $\mathrm{d}_{(v,0.5)}$ is 16.3 μm, while for the LPW powder, $d_{(v,0.5)}$ was determined to be 48.4 μm. This indicates that 50 vol% of the powder particles have a smaller diameter than 48.4 μm for LPW powder.

The quantitative stereology and the mastersizer results indicate that the distribution of the CL powder particle size is wider, while the range of particle sizes of the LPW powder is much smaller. The SEM images of both powder batches confirm these results, as shown in Figures 4.2 and 4.3. In the CL powder, there is a great variety of both bigger and smaller particles, while in the LPW powder, all particles have about the same size.

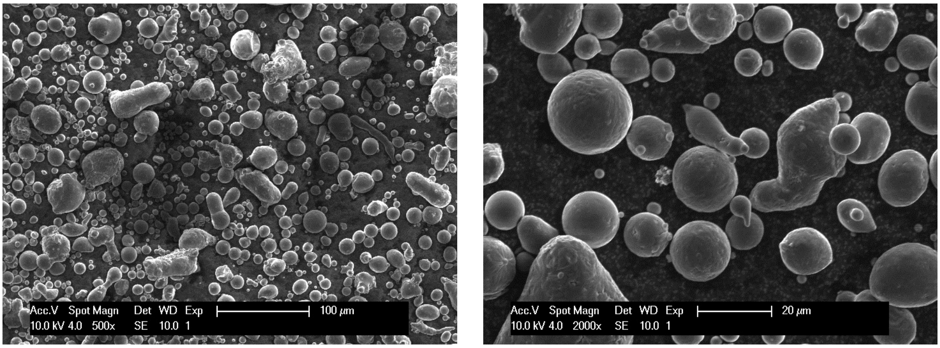

Figure 4.2: Concept Laser A360.0 aluminum powder observed by SEM in two magnifications.

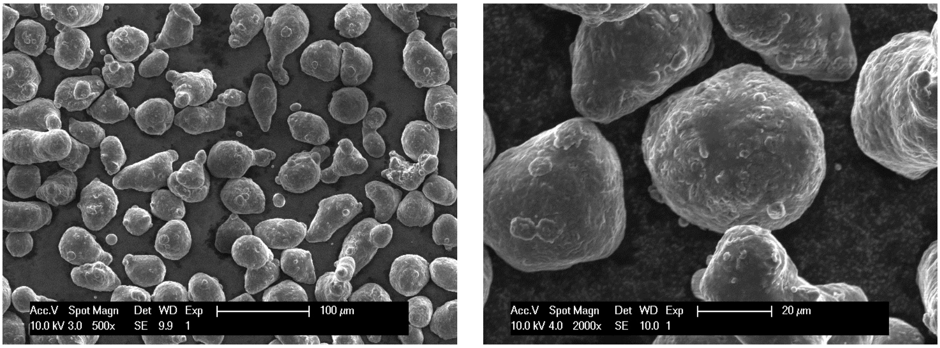

Figure 4.3: LPW A360.0 aluminum powder observed by SEM in two magnifications.

These pictures show that the CL powder has a more spherical morphology and a smoother surface, while having less satellite-particles. These properties result in a better flowability and a more homogenous powder layer deposition for CL powder compared to LPW powder which was also evident during processing.

4.4.3 3D Part production

When producing parts with identical process parameters from these two powder batches, there is a noticeable difference in density. Relative density results (measured by the Archimedes method, with an absolute density of 2.68 g/cm^3) are depicted in Figure 4.4. The parts were produced with scan parameters as advised by Concept Laser for this material, on a Concept Laser M1 machine: laser power of 170 W, scan spacing of 105 μm and scan speed varying from 800 mm/s to 1600 mm/s (200 mm/s was advised by Concept Laser, in combination with 200 W laser power, leading to failing samples). The discrepancy of about 1% between density results of CL and LPW powders may be due to powder morphology and material composition as explained above. The powder comparison indicates more promising results for CL A360.0 powder for SLM. For this reason, further research described in this work was conducted with the A360.0 powder supplied by Concept Laser.

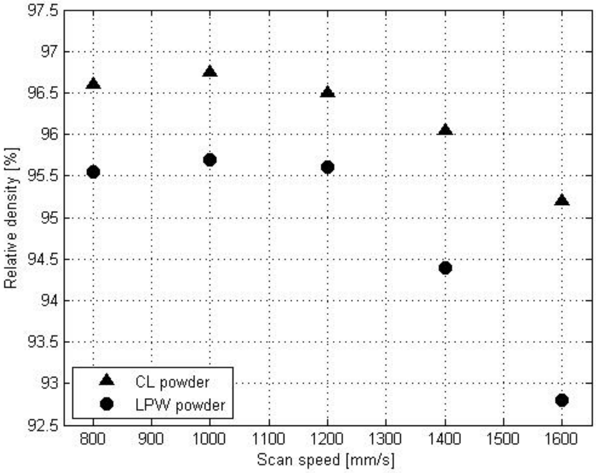

Figure 4.4: Relative density results for parts produced with identical scan parameters, but different powders (CL and LPW).

4.5 Process window through single track scans

Single track scans are formed when a powder layer of a certain thickness (30 μm in this case) is deposited, and the laser scans one single line in the powder bed. Single track scans clearly indicate the nature and the shape of the melt pool, depending on the scan speed and laser power. These single track scans are a fast and simple way to determine the process window in which the melt pool meets the set requirements. In this study, a laser power ranging from 170 W

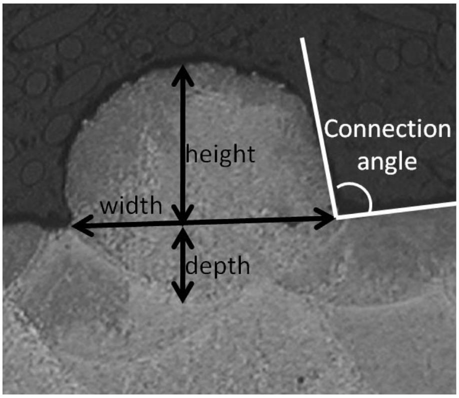

Figure 4.5: Requirements for single scan tracks: measurement protocol.

to 200 W is used in combination with a scan speed varying between 200 and 1400 mm/s. The requirements for the melt pool, that are set for a parameter combination to be submitted to the process window are:

1. The scan track must be uninterrupted, to avoid pores and irregularities in the part.
2. The scan track must slightly penetrate the previous layer, in order to get a good connection between the subsequent layers (good wetting of the layer underneath).
3. The scan track must have a sufficient height, in order to be able to build up three-dimensional parts.
4. The connection angle between scan track and previous layer should be close to 90°, to ensure good dimensional accuracy and high density. Larger connection angles will require a larger overlap between adjacent scan tracks.

The measuring protocol for these three last requirements is clarified in Figure 4.5.

Single track scans were evaluated by Scanning Electron Microscope, both by top view (to check the continuity of the scan track) and by cross section (to check the depth, height and width of the melt pool and the connection angle). As these tests only consider one scan track instead of a surface or volume, the results are analyzed in function of the laser energy per unit length E_l. The

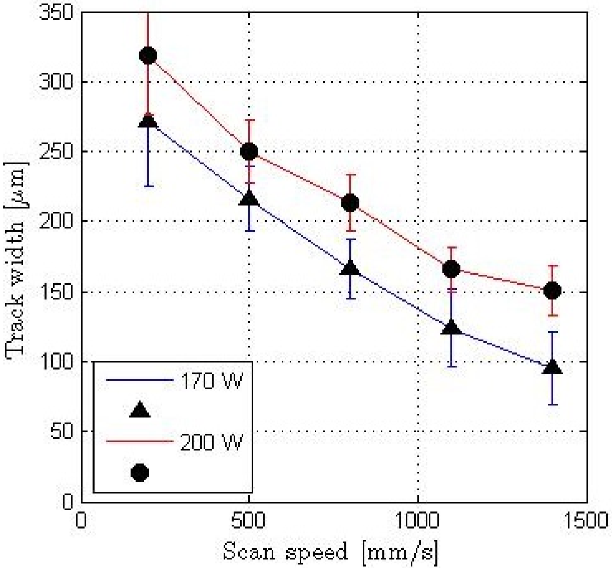

Figure 4.6: Measurement of the track width for single track scans produced with varying laser power and scan speed.

definition of E_l is given in equation 4.1 with E_l = laser energy per unit length [J/mm], E = laser energy [J], l = length of the scan track [mm], P = laser power [W], v = scan speed [mm/s].

$$E_l = \frac{E}{l} = \frac{P}{v} \tag{4.1}$$

From the cross sectional views, the **width and depth** of the single track scan were **measured**. For one parameter set, four single track scans were analyzed, and the results of the measurements are depicted in Figures 4.6 and 4.7 with a 95% confidence interval.

The width of the single track (Figure 4.6) significantly decreases for increasing scan speed, while it increases for increasing laser power. As was expected, the melt pool width increases for increasing energy per unit length. The more heat being transferred to the powder bed, the more particles will melt and the bigger the melt pool will be. For materials with a lower thermal conductivity, this effect of the energy input on the track width is expected to be even more pronounced.

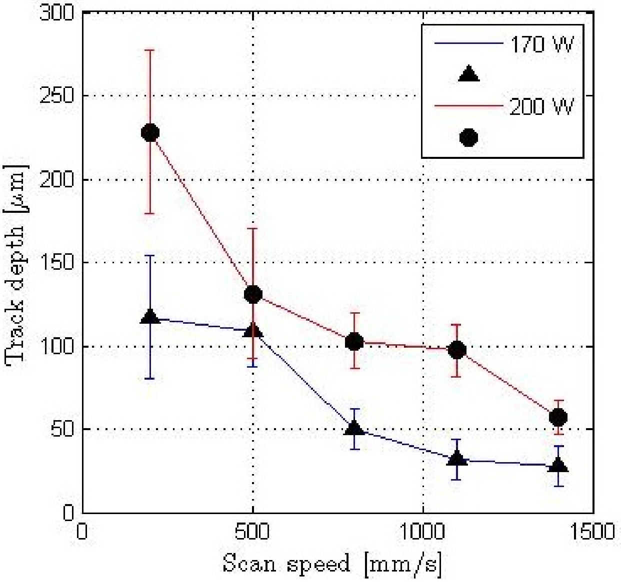

Figure 4.7: Measurement of the track depth for single track scans produced with varying laser power and scan speed.

A similar trend is expected and observed for the depth of the melt pool (Figure 4.7). The higher the energy per unit length, the deeper the melt pool. For a very high energy input (v = 200 mm/s, P = 200 W), the depth of the melt pool increases significantly. This is because there is a transition to keyhole mode laser melting. This will be discussed in detail further on in this section.

Upon **visual inspection** of both the top view and the cross sectional view of the single track scans, a **process window** is defined in which the single track scan meets all the set requirements. Figure 4.8 and Figure 4.9 plot the single track scans in function of the laser power and scan speed that were employed.

When the **laser energy per unit** length is **too high**, for instance by increasing the laser power or decreasing the scan speed, the melt pool volume increases, and the temperature increases. The higher temperature results in a lower melt viscosity and a lower surface tension. As indicated in section 1.2.4, this causes very strong marangoni flows, forming a deep melt pool [73, 180].

These deep melt pools can be observed in zone 1 in Figure 4.9.
Besides the changes in melt pool hydrodynamics, the high temperature that is reached also causes more evaporation. The vapor recoil pressure above the melt pool distorts the melt track, as observed in zone 1 in Figure 4.8.

Another observation from the cross sectional images in zone 1 can be made concerning the formed porosity at the bottom of the melt pool. For a very high laser energy input per unit length, the laser melting phenomenon transitions from so-called *conduction mode* into *keyhole mode*, as similarly known and used in laser welding [65]. When the laser intensity is sufficiently high, a deep penetrating vapour cavity is formed inside the melt pool. The stability of this keyhole is based on the equilibrium between the forces which open the cavity (plasma formation, material ablation) and the forces which tend to close it (gravity, surface tension)[192]. A schematic illustration of keyhole mode in laser welding is depicted in Figure 4.10. A small change in scan speed or temperature in the melt pool can cause an instability, resulting in a melt pool collapse, leaving entrapped gas, and thus small pores on the bottom of the melt pool. One of these so-called ***keyhole pores*** is seen in Figure 4.9 in the cross section for a scan track produced at 200 W and 200 mm/s.
The formation of these keyhole pores is widely documented in laser welding, where parameters also have to be optimized to avoid collapse of the keyhole and the resulting porosity [58, 170, 191].

At high scan speed and **low energy input per unit length** (zone 3 in Figure 4.8 and Figure 4.9), the melt pool becomes more and more elongated (rather than spherical) and surface tension breaks the melt pool into droplets, spheriodizing the liquid [155]. This *balling effect* occurs when the total surface of the melt pool becomes larger than that of a sphere with the same volume [85, 137], i.e. for a non-spherical but elongated melt pool.
According to the Plateau-Rayleigh analysis of instability of a segmental cylindrical liquid [180], melt pools with a smaller circumference-to-length ratio show an unstable behavior.
For high scan speeds for instance, the melt pool is very long and narrow. the ratio of $\frac{\pi D}{L}$ decreases for higher scan speeds, and so the melt pool becomes more and more unstable.
As observed in zone 3 in Figure 4.9, there is a very bad wetting and droplets are formed. This balling phenomenon results in insufficient connection to the previous layers. It can lead to a rough and bead-shaped scan track, increasing the top surface roughness and increasing the porosity [92]. Since liquid metals do not wet surface oxide films in the absence of a chemical reaction, it is very important to avoid oxidation. Another way to influence the wetting behavior

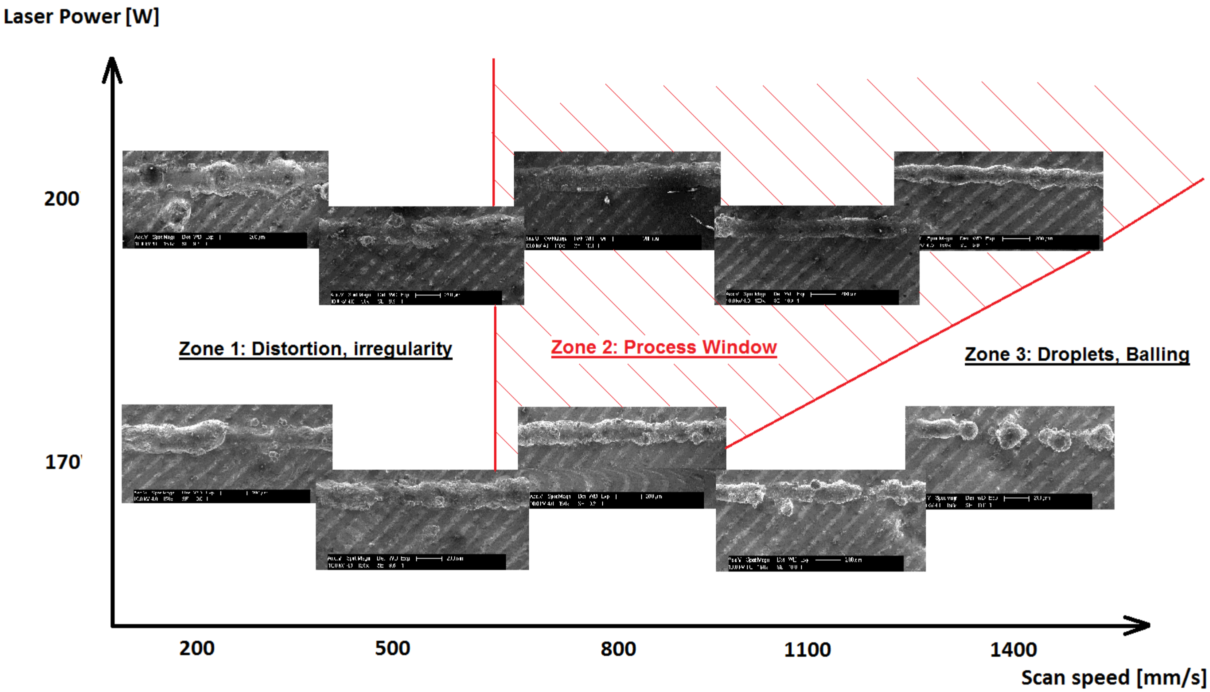

Figure 4.8: Top view images of single scan tracks, produced with different process parameters.

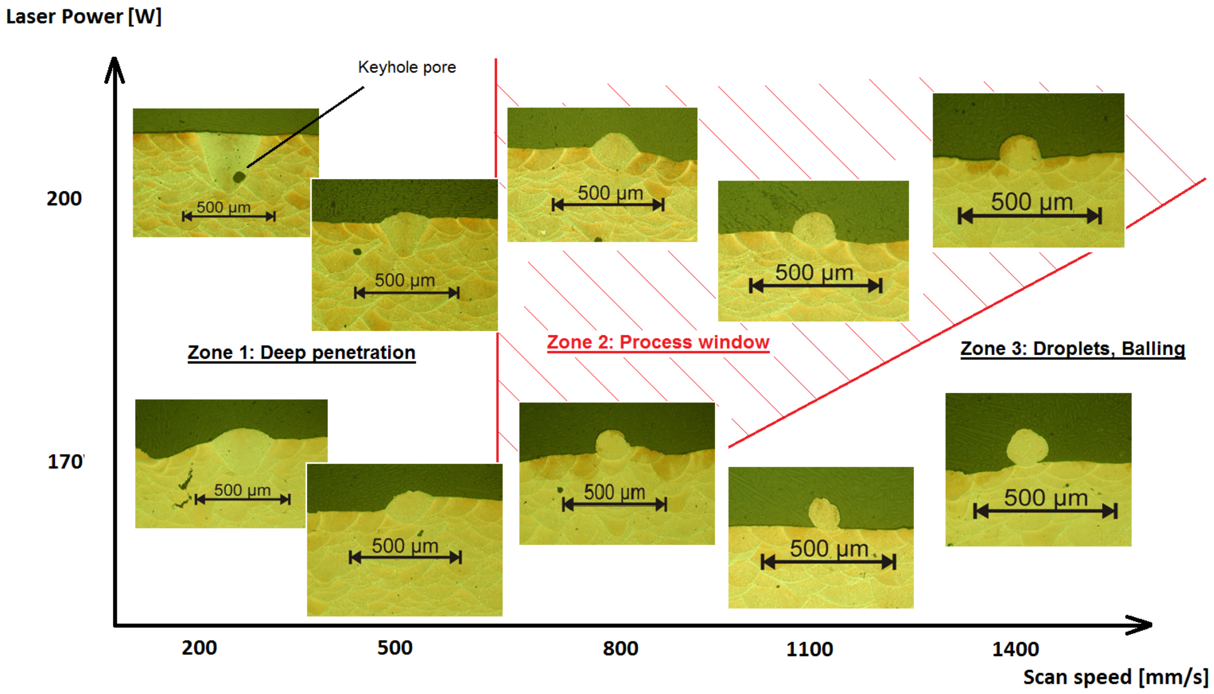

Figure 4.9: Cross section images of single scan tracks, produced with different process parameters.

is by addition of certain alloying elements like phosphor in SLM of iron-based powders [84].

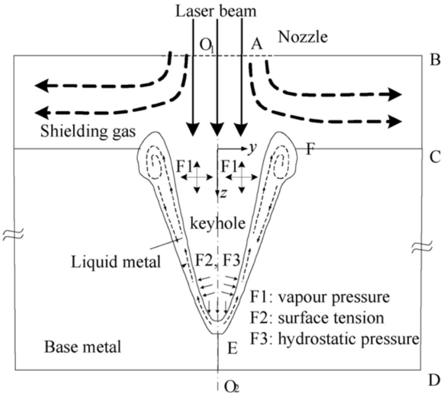

Figure 4.10: Cross sectional sketch of keyhole mode in laser welding [192].

Taking all the set requirements into account, a process window is defined within this range of process parameters, marked with red lines. This zone 2 indicates the stable processing conditions, corresponding to an energy per unit length of about 150 to 200 J/m.

4.6 Parameter optimization

In this section, the effect of the most important scan parameters (laser power P, scan speed v, scan spacing h) on physical properties like density and surface roughness is investigated, as well as the effect of applying laser remelting. It will be shown that, depending on the requirements of the final part (full density, good surface quality, high process productivity) the optimal parameter set will be different.

4.6.1 Density optimization

Part density is one of the most important parameters to optimize, because it has a direct influence on the part's mechanical and physical properties. In this work, relative densities are used as a way to quantify the remaining porosity in the SLM parts. The relative density is obtained through comparison of the

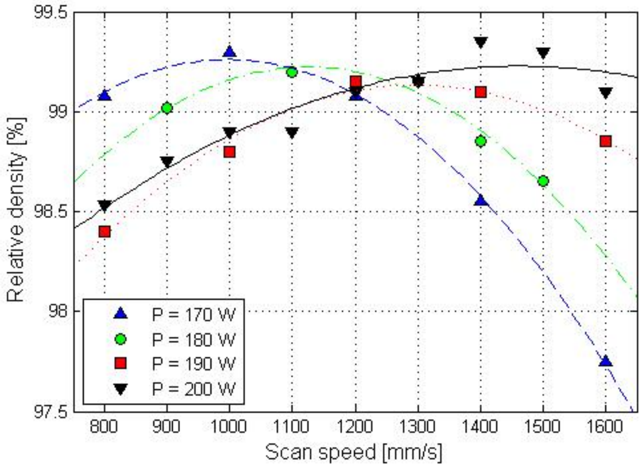

Figure 4.11: Relative density of A360.0 parts produced with different scan parameters.

theoretical density value of the alloy and the measured value of the part. The theoretical density for A360.0 is 2.68 g/cm^3.
The part density depends on many process parameters, while this research focuses only on the most influential ones: laser power P, scan speed v and later also scan spacing h and the effect of laser remelting. Cubic parts of 10 mm x 10 mm x 10 mm were produced with scan parameters as defined within the process window of the single track scans: the laser power varying from 170W to 200W in steps of 10W, and scan speed ranging from 800 to 1600 mm/s in steps of 100 mm/s. The hatch spacing is chosen at 105 μm, being 70 % of the melt pool width, thus resulting in a 30 % overlap between adjacent scan tracks. The density of all parts is measured and depicted in Figure 4.11. No error bars are shown as only one part of every parameter combination was produced. Thus, the absolute values of these density measurements should be carefully interpreted. It is mainly the trend of the graphs that is discussed here.

As was expected from the observations in the single track scans, the density is low for parts produced with a very high energy density (high laser power, low scan speed) and for parts produced with a very low energy density (low laser power, high scan speed) . The highest densities are reached when the energy input per unit length is optimal to produce a stable melt pool, which seems to be 140 - 160 J/m for this aluminum alloy. As a result, and also noticable in Figure 4.11, the point of maximal density lies at low scan speed for low laser

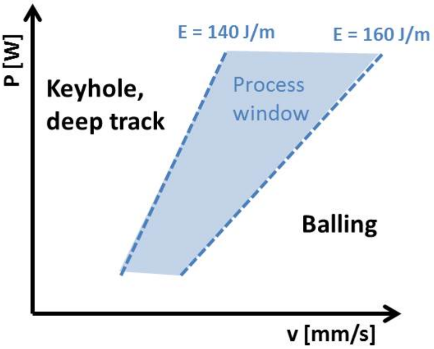

Figure 4.12: A schematic demonstration of the broadening of the process window for high laser power.

power, and at high scan speed for high laser power. Consequently, if production speed is an important factor, the optimal parameter set in these conditions is a laser power P of 200 W, a scan speed v of 1400 mm/s and at a hatch spacing h of 105 μm (coinciding to a well suited scan track overlap of 30 %), because the laser power for this SLM machine is limited to 200W. A higher productivity could be reached with a higher laser power, enabling higher scan speeds [17].

A second observation that can be made from both Figure 4.9 and Figure 4.11, is the broadening of the process window for higher laser power. When defining the optimal laser energy per unit length as $E_{l,opt}$ = P/v, then E_l respresents the slope of the P - v graph. For $E_{l,opt}$ between 140 J/m and 160 J/m, the slopes of the curves indicating the border of the process window correspond to those 140 and 160 J/m (Figure 4.12).
In other words, the process window is defined between two linear boundaries in the P-v graph: $P = E_{l,min} * v$ and $P = E_{l,max} * v$.
This results in a broader process window for a higher laser power. This observation can also be made in Figure 4.11. When employing a higher laser power (for example 200 W), the zone of high density parts is wider (ranging from 1000 mm/s to $\geq$ 1600 mm/s). For lower laser power (for example 170 W), the zone of high density parts is more narrow (ranging only from 800 mm/s to 1200 mm/s). 'High density' in this case is defined as any density above 99%.

4.6.2 Surface Roughness optimization

Surface quality can often be an important requirement for SLM-built parts. Average roughness value P_a of the top surface is measured for all the parts and depicted in Figure 4.13. For a given laser power, the surface roughness value P_a reaches a minimum at a certain scan speed. The minimal average roughness value for every given laser power is indicated with a circle in Figure 4.13. The higher the laser power, the lower the optimal scan speed. For an increasing energy density, the surface quality will improve as long as the melt pool is stable. Once the keyhole instabilities start to take place, the roughness strongly increases. A visual evolution of the top surface roughness for increasing energy input is depicted in Figure 4.14.

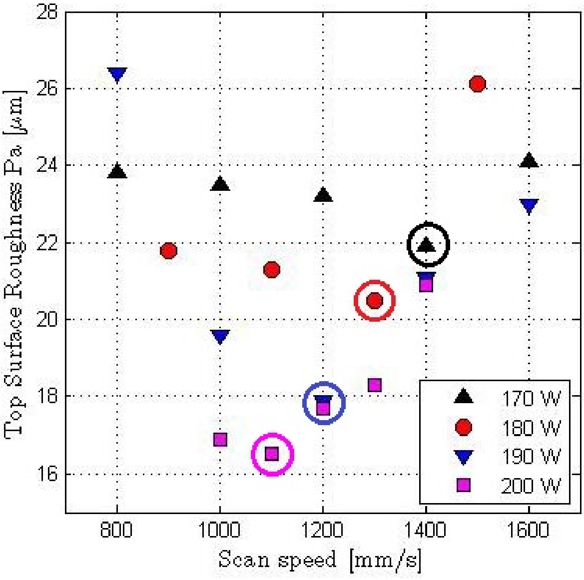

Figure 4.13: Average top surface roughness for different laser power and scan speed. The scan spacing is kept constant at 105 μm. The minimal average roughness value for every given laser power is indicated with a circle.

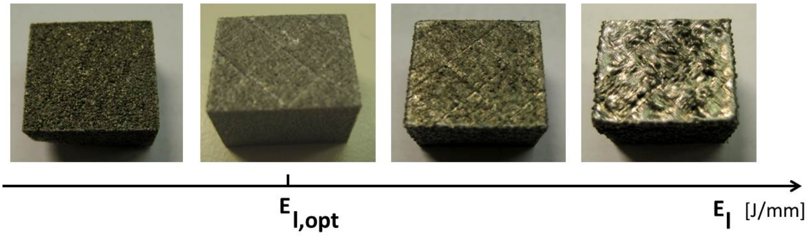

Figure 4.14: Evolution of the top surface roughness for increased energy input.

Combining the density and the surface roughness results, two parameter-sets can be defined, depending on the requirements of the SLM-part. The optimal parameter-set in terms of density and productivity is a laser power of 200 W and a scan speed of 1400 mm/s. Combined with a scan spacing of 105 μm, a scanning productivity $\dot{V}$ of 4.4 mm^3/s is obtained, calculated by the product of layer thickness t, scan speed v and scan spacing h as depicted in equation 4.2 [13, 24].

$$\dot{V} = t.v.h \tag{4.2}$$

The optimal parameter-set in terms of both density and surface quality is a laser power of 200W and a scan speed between 1100 mm/s and 1300 mm/s leading to a density above 99.2 % and a top surface roughness below 19 μm P_a. The density can be further increased to 99.4 % when increasing the scan speed to 1400 mm/s, but it slightly deteriorates the surface quality. Post-processing steps like sandblasting or even milling can still be considered to finish the part to a better surface quality.

Both the optimal density and optimal surface quality parameter sets lie within the process window previously determined by the single track scans.

4.6.3 The effect of scan spacing

Density could be improved by optimizing the scan spacing between the scan tracks. Cubic test parts were produced with the optimal density parameters of 200 W and 1400 mm/s. The scan spacing was varied from 75 to 150 μm in steps of 15 μm. Both density and top surface roughness were measured and plotted in Figure 4.15.

When the scan spacing is **too large**, the scan tracks will not connect, and unmolten powder will remain between the scan tracks. This results in a very

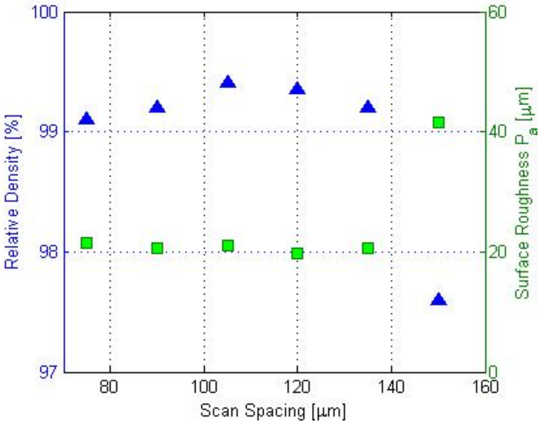

Figure 4.15: Relative density and top surface roughness in function of the scan spacing for parts produced with a laser power of 200W and scan speed of 1400 mm/s.

low density and a rough top surface, as depicted for a scan spacing of 150 μm in Figure 4.15. The width of the melt pool for a single track scan with these parameters is about 150 μm, as was measured and depicted in Figure 4.6.
When the scan spacing **equals** the average width of the melt pool, the tracks remain unconnected in some places because of the somewhat irregular shape of the melt pool. This leads to elongated pores between scan tracks.
For a **very small** scan spacing, the overlap between adjacent scan tracks is great. Not only does it increase the production time significantly, because a surface includes more scan tracks, but it can also lead to porosity. Upon scanning, not only the powder in the laser irradiation zone is involved in the scan vector, but also the powder from adjacent areas. This effect is called *denudation* of the powder bed [179]. If the scan spacing is so small that the neighboring scan track lies completely in the first track's denudation zone, then there is no powder material available there, resulting in porosity. The size of the denudation zone was not measured in these tests. According to the density results in Figure 4.15, the denudation zone is smaller than 75 μm, because no significant decrease in density was measured within this parameter range.

4.6.4 The effect of laser remelting

The term '*laser remelting*' is used to refer to a second pass of the laser beam without additional powder deposition and for different purposes such as further material densification, surface quality and microstructural enhancement of SLM parts [184, 187].

Previous research by Yasa et al. has shown that the remelting scan strategy can improve the **density** of Ti6Al4V and 316L stainless steel parts up to 99.9% [187]. After parameter optimization for A360.0 in function of density, the most dense part still contains 0.6 % porosity. In the following tests, laser remelting is applied with the goal of eliminating the remaining porosity.

In a preliminary test, laser remelting was applied with identical scan parameters and scan strategy. An observation of the top surface applying Scanning Electron Microscopy, depicted in Figure 4.16, reveals that the scan tracks after remelting are not as wide as the tracks in the first scanning step. This part was scanned with a laser power of 200W, a scan speed of 1400 mm/s and a scan spacing of 105 μm, and remelting applied with identical scan parameters.

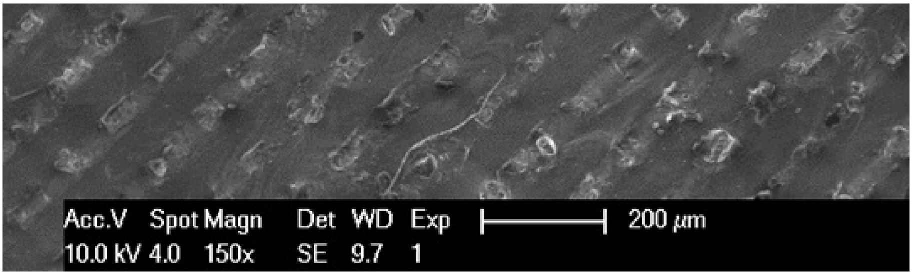

Figure 4.16: Top surface of a SLM part produced with a laser power of 200 W, scan speed of 1400 mm/s, scan spacing of 105 μm, and remelting with identical scan parameters.

In the second scanning step, solid material is melted, instead of powder material like in the first scanning step. This leads to an entirely different heat flow. The thermal conductivity for solid material is bigger, leading to a smaller melt pool. This means that for remelting purposes, the scan parameters have to be adjusted: either a decrease in scan speed, or a decrease in scan spacing. Because the SEM image in Figure 4.16 shows a stable melt pool in the remelting step, the scan speed is kept the same. The width of the melt pool is measured to be 64.12 ± 6.3 μm, so the scan spacing for the remelting step will be adjusted to 60 μm. This results in optimal parameters as given in Table 4.5.

Table 4.5: The optimized parameters for production of a nearly full dense A360.0 part by SLM.

	Laser Power P [W]	Scan Speed v [mm/s]	Scan spacing h [μm]	Layer thickness [μm]	Relative density [%]
SLM	200	1400	105	30	99.4
Remelting	200	1400	60	0	99.8

Upon applying the optimized remelting scan parameters, densities were measured according to the Archimedes principle. The results are shown in Figure 4.17. Within this parameter range, applying the remelting step for every layer increases the density of the final part, up to 99.8 % for a scan speed of 1400 mm/s.

The densities (or porosity) of the samples produced with no remelting (standard SLM parameters) and of samples obtained by applying laser remelting parameters after each SLM layer, were observed with a light optical microscope. Figure 4.18 shows the difference in porosity, that was confirmed by the measurements by Archimedes method. Upon the second scanning step, the solid material is partially melted again. Any unmolten powder from the first scan step can melt now. Any gas bubbles that were entrapped in the melt pool in the first scan step can now rise to the surface and leave the melt pool in the remelting step. The porosity that still remains after remelting are the keyhole pores that are located too deep in the melt pool. This can be seen in the right image of Figure 4.18. If the melt pool of the remelting step does not reach the depth of a random occurring keyhole pore, the entrapped gas bubble can not escape and remains. A bigger (and deeper) melt pool can be formed by using a lower scan speed and/or higher laser power.

To summarize: The optimal density that can be reached by Selective Laser Melting of A360.0 aluminum alloy is 99.8%, by the use of the optimized parameters in Table 4.5. The remelting step however, increases the production

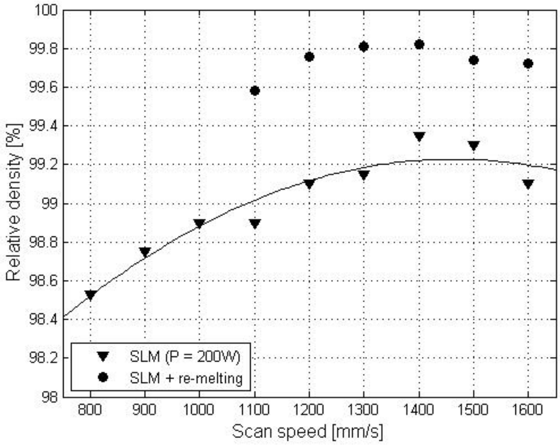

Figure 4.17: The density improvement that is accomplished by laser remelting for parts produced with a laser power of 200 W a scan spacing of 105 μm and a varying scan speed. Laser remelting was applied with identical scan parameters, but a scan spacing of 60 μm.

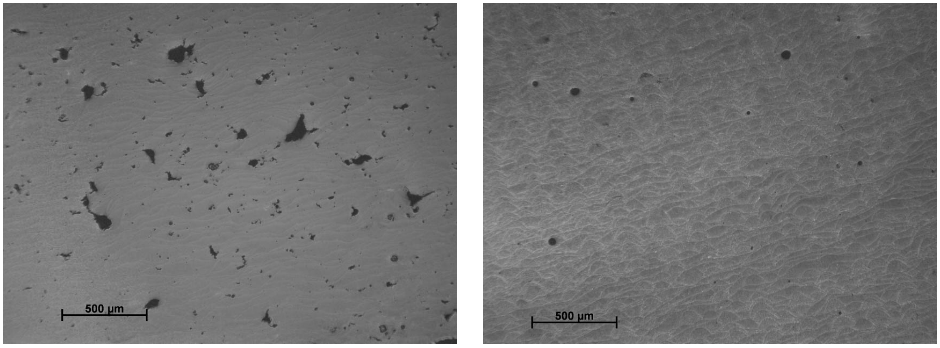

Figure 4.18: Cross-sectional micrographs of A360.0 SLM parts with (right) and without (left) applying remelting with identical scan parameters.

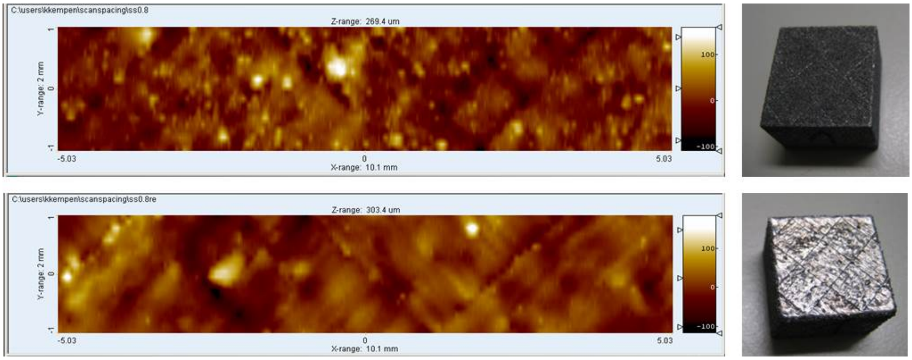

Figure 4.19: Two dimensional surface roughness map (left) and visual inspection of cubic parts (right) for A360.0 parts produced by scanning every layer once (top) or applying remelting for every layer (bottom).

time significantly. If nearly-full density is not a requirement for the final part, the remelting step can be eliminated, still resulting in a 99.4 % dens part.

The **top surface roughness** of SLM parts can be improved by laser remelting [184]. The three-dimensional roughness profile is measured on the top surface of a cubic SLM part produced with and one without remelting. A two-dimensional surface color map is given in Figure 4.19, along with optical images of the as-produced parts for visual inspection. From the photos it is visually clear that after remelting, the part has a more shiny look. Several roughness parameters are calculated from the measured top surface, as given in Table 4.6. Although the surface of remelted parts looks a lot more smooth to the naked eye, the roughness values of P_a, P_y and P_q do not differ very much for both parts. From the color map in Figure 4.19 it can be seen that the as-built SLM part (single scanning) is a surface with some very high (bright) peaks, while the remelted surface is a surface with some very deep (dark) grooves. A sketch of a similar situation is given in Figure 4.20.

A surface roughness parameter that can define the difference for these surfaces is the skewness P_{sk} [60]. The definition of the skewness is given in equation 4.3. Surfaces with high peaks have a positive skewness (like the bottom picture in Figure 4.20). Surfaces with deep valleys have a negative skewness value (like the top picture in Figure 4.20).

$$P_{sk} = \frac{1}{nP_q^3} \sum_{i=1}^{n} y_i^3 \tag{4.3}$$

Table 4.6: Surface roughness parameters for as-built SLM parts and parts produced by remelting every layer.

	P_a	P_y	P_q	P_{sk}
SLM	22.5	289	29.5	0.96
SLM + remelting	23.8	303	31.4	-0.15

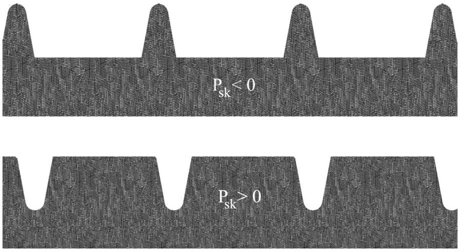

Figure 4.20: Two different surfaces with identical P_a, P_q and P_t values, but a negative skewness (top), and a positive skewness (bottom).

with

$$P_q = \sqrt{\frac{1}{n}\sum_{i=1}^{n} y_i^2} \tag{4.4}$$

The as-built SLM part (single scanning) has a positive skewness, showing that peaks were built up during SLM processing. The remelted part has a negative skewness, indicating a surface with some deep valleys. As both can be observed by visual inspection from the part, and by the measured color map, the peaks that were formed during SLM are flattened upon remelting. This results in a shiny surface compared to the as built SLM top surface. The deep valleys that remain are the island borders from the island scanning pattern that was used to build these parts. Remelting happened with the same scanning strategy, leaving the deep island borders to remain on the top surface. In order to improve the top surface roughness, it would be recommended to change the scanning strategy of the remelting step from the original scan strategy.

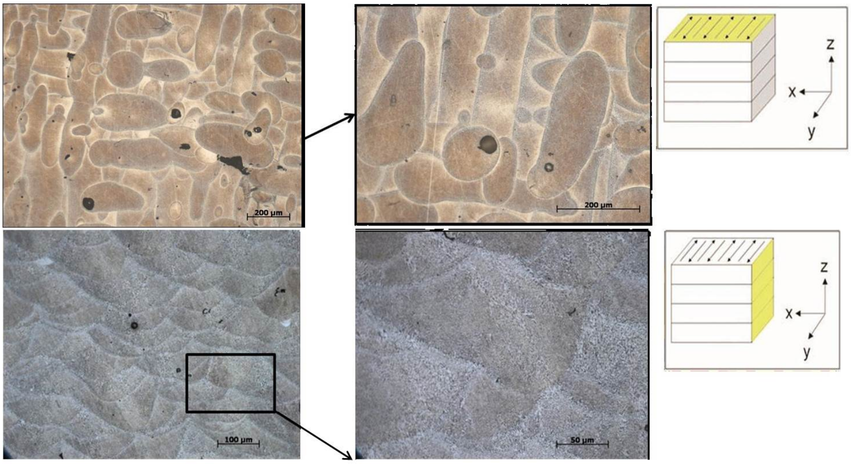

Figure 4.21: The microstructure of SLM produced A360.0 parts, in two magnifications and both in top view and cross sectional view.

4.6.5 Microstructure

The high-density parts were analyzed by optical microscopy (OM). These parts were produced with a laser power of 200W and a scan speed of 1400 mm/s on the Concept Laser M1 machine. Optical microscopy images were taken of the top view (XY plane) and the cross section (YZ plane). The Z direction indicates the building direction.

These microscopy images and the XYZ convention is shown in Figure 4.21. First, these OM images confirm the high density that was measured by Archimedes. The cause of the remaining porosity (0.6 %) is threefold. The **small spherical pores** result from gas that was entrapped during melting and solidification. Entrapped gas is likely to originate from:

1. Gas in the powder bed or gas inside the powder particles, resulting in very small spherical pores.
2. Evaporation of the material/selected elements (e.g. Mg or Si in this case of AlSi10Mg) leads to small spherical pores.
3. Collapse of a keyhole in an unstable melt pool and/or absorbed hydrogen or hydroxide can leave a larger spherical pore behind.

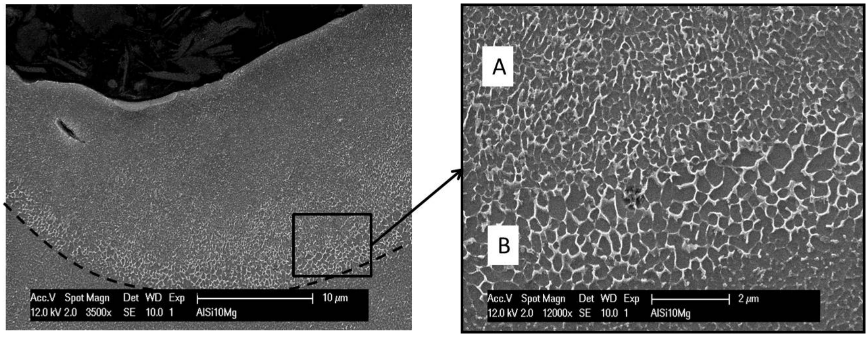

Figure 4.22: Cross section of one melt pool: finer microstructure in the center of the melt pool (A) coarser microstructure on the melt pool boundary (B).

These pores are located within the melt pool , as observed in the top view of Figure 4.21.
The second classification of pores are **irregular** in shape and are located at melt pool boundaries. These pores are formed due to unmelted powder or insufficient overlap between scan tracks. In addition to the pores, also **oxides** may be formed. They usually have a very irregular, flat-like shape.

Etching with Keller's reagent reveals the melt pool boundaries. The images at higher magnification in Figure 4.21 give a first indication of the coarser microstructure at the melt pool boundaries. A more detailed SEM image is depicted in Figure 4.22.

Due to the movement of the heat source, the solidification variables may vary across the melt pool. As discussed in section 1.2.4, the solidification time at the fusion line is longer than at the centerline of the melt pool. As a result, a finer microstructure is expected near the centerline of the melt pool than close to the fusion line. This translates in a finer cellular structure in the center of the melt pool ([A] in Figure 4.22) and a more coarse microstructure at the border of the melt pool ([B] in Figure 4.22). A more in-depth research on the formed microstructure and resulting texture in these parts is reported by Thijs et al. [150, 152]. In laser surface melting of Al- 15wt% Cu, a similar fine microstructural evolution is observed, varying from coarse at the border to fine at the center of the melt pool [129]. In Dinda et al. [44], it is shown that for Direct Metal Deposition of Al-11.28wt%Si, the different layers are also clearly depicted in the microstructure and the morphology is influenced by the laser power and rate of heat extraction.

Table 4.7: Mechanical properties of SLM as-built parts, compared to high pressure die cast (HPDC) parts, with and without T6 heat treatment.

x ± s	E GPa	UTS MPa	Elongation %	Hardness HV
SLM (XY direction)	68 ± 3	407 ± 16	5.1 ± 0.5	127 ± 2
SLM (Z direction)	67 ± 5	396 ± 8	3.5 ± 0.6	126 ± 2
HPDC [50]	71	300 - 350	3 - 5	95 - 105
HPDC + T6 [50]	71	330 - 365	3 - 5	130 - 133

4.7 Mechanical properties

4.7.1 Micro hardness and Tensile testing

Micro-hardness and tensile tests were performed on both as-built SLM parts in the XY-direction, built flat onto the baseplate, and on SLM parts built in the Z-direction, up straight. All parts were produced with the parameters for optimal density, including the remelting step. The results of these tensile tests are summarized in Table 4.7 and compared to values for high pressure die cast parts, with and without standard T6 heat treatment. High pressure die casting is considered as the casting process resulting in the best mechanical properties. All results represent the mean value for 3 specimens with a 95% confidence interval.

A first observation shows that SLM A360.0 parts have mechanical properties higher or at least comparable to the cast A360.0 material. The **Vickers hardness** of the as built SLM parts is much higher (almost 30 HV) than the hardness of the high pressure die cast A360.0 in the as-cast condition and almost as high as the HPDC A360.0 in the aged condition.
Ultimate Tensile Strength values of the SLM parts are higher than the highest values obtained by high pressure die casting with heat treatment. While the range for casting is between 330 and 365 MPa, the ultimate tensile strength of the as-built SLM parts reaches above 400 MPa. In casting, the high strength and hardness is reached by the formation of Mg_2Si precipitates during the T6 temper. In SLM parts, significantly higher hardness and strengths are already reached in the as-built state, i.e. non heat treated condition. These values result

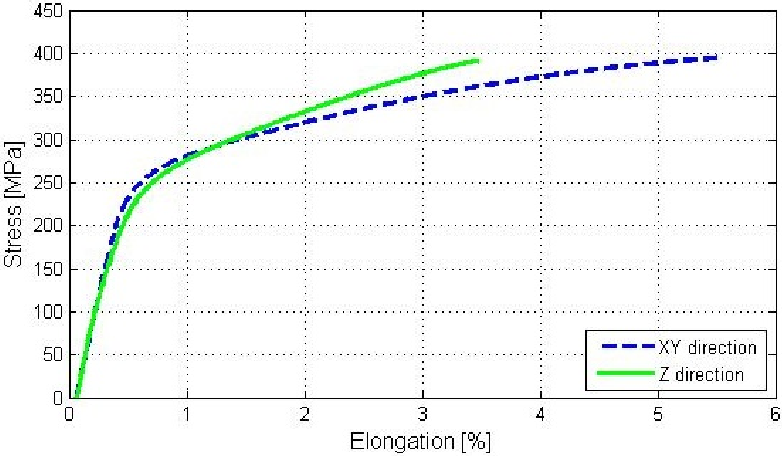

Figure 4.23: Stress-Strain curve for A360.0 SLM parts, produced in different directions.

from the very fine microstructure and fine distribution of the Si phase in A360.0 SLM parts due to the rapid cooling and solidification, and probably also from the presence of Mg_2Si although those precipitates were not observed by XRD analysis. The remarkably fine microstructure consisting of small Al-matrix cells/dendrites decorated with Si phase is shown in Figure 4.22.

The **Young's modulus** does not differ significantly between the different production processes.

The **elongation** of the as-built A360.0 parts in the Z-direction is comparable to the HPDC parts, while the elongation for parts built in XY - direction is almost 2% higher. From these tensile test results, it can be seen that the SLM samples show anisotropy in their properties. A comparison between the stress-strain curves for the two directions in Figure 4.23 shows a different strengthening behavior. The elongation at break is seen to be lower for the XY oriented samples compared to the Z oriented samples. A possible explanation for this anisotropic behavior is given below, in section '*Charpy impact testing*'.

4.7.2 Charpy impact testing

The V-notch Charpy impact test was used to determine material toughness by hitting a test specimen with a hammer mounted at the end of a pendulum. The height of rise of the pendulum gives an indication of the absorbed energy

Table 4.8: The absorbed energy resulting from Charpy impact testing for SLM parts built in two directions, compared to HPDC parts.

x ± s	impact energy [J]
SLM (XY direction)	3.94 ± 0.5
SLM (Z direction)	3.69 ± 0.48
HPDC [50]	2.5 - 3

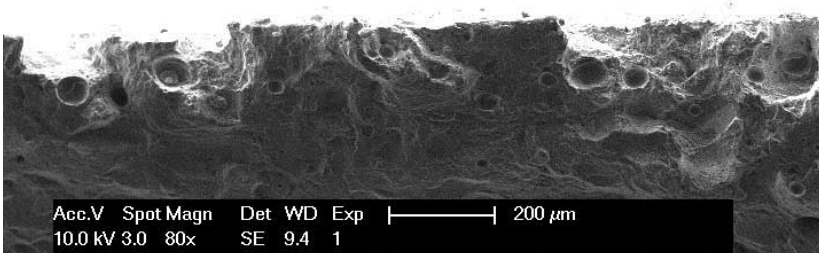

Figure 4.24: Fracture Surface of a SLM-produced A360.0 sample. The border of the broken test sample is shown, where the keyhole porosity initiated cracks towards the side of the sample.

that was needed to deform and break the specimen. The results of the Charpy impact tests are summarized in Table 4.8.

Although the strength and hardness is higher, the Charpy impact energy of the as-built SLM samples is still superior to that of the conventionally cast A360.0 material.

On the other hand, while tensile tests show a significant difference in ductility between parts produced in XY-direction and parts produced in Z-direction, the difference in toughness is not significant for Charpy test results. Furthermore, it is interesting to notice that all tensile test samples were seen to break at UTS. Note that, in tensile tests, deformation is much slower (0.4 mm/min) than for Charpy impact tests.

Upon observation of the fracture surface of a tensile sample (Figure 4.24), it can be seen that larges pores near the border of the sample initiate the fracture. These are keyhole pores, formed at the beginning of a scan vector. As illustrated in the left images in Figure 4.25, these keyhole pores are more numerous in parts produced in the Z direction, compared to parts produced in the XY direction. This was confirmed by the fracture surfaces shown in the right images in Figure 4.25. The keyhole pores are marked by a red circle. These pores are the largest defects present in the part. At a high stress level (i.e. 395 MPa for both testing directions), they will become the critical defects which initiate inhomogeneous deformation. Because of their location close to the sample border, they lack space for extensive deformation and easily cause complete fracture of the sample. Due to the faster strengthening of the Z direction, this high stress level is reached sooner and as a result the elongation in tensile test is lower: 3.47% compared to 5.05% for XY oriented samples.

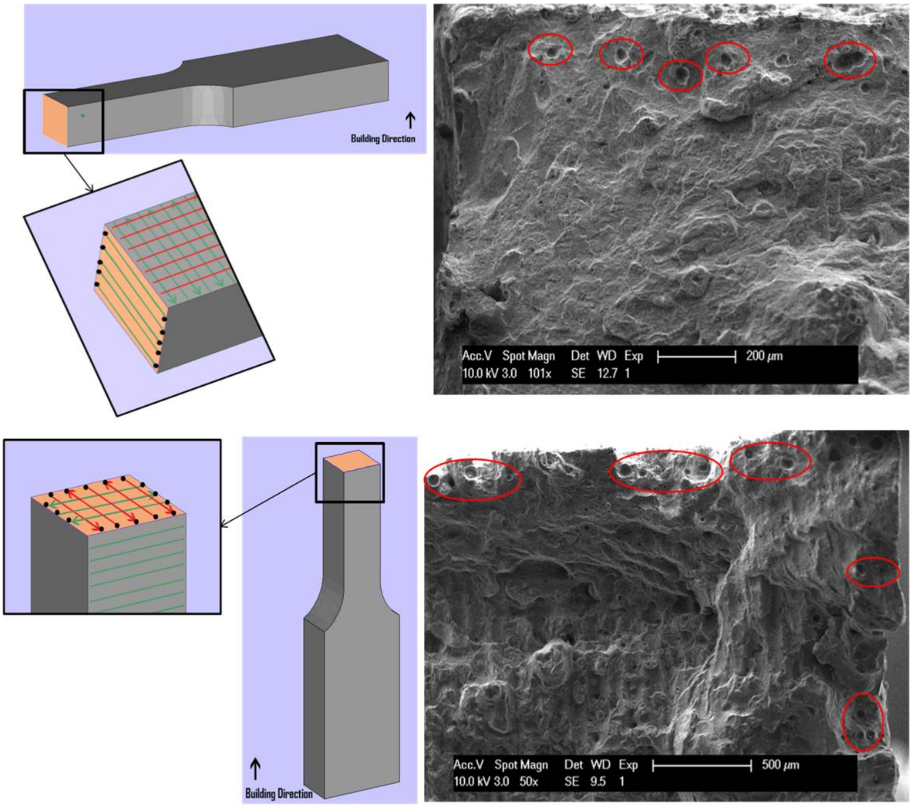

Figure 4.25: Left: Optimal density scanning strategy for tensile samples produced in 2 directions. First zigzag scanning, then remelting of every layer with zigzag pattern rotated over 90°. Keyhole pores are formed at the beginning of every scan vector. Right: Tensile sample fracture surfaces show presence of keyhole porosity at the borderline: in one direction for XY-oriented samples (Top image), in two directions for Z-oriented samples (Bottom image)

It is shown that the keyhole porosity at the borders of the samples are detrimental for the part's fracture behavior. In case the defined remelting step does not eliminate this kind of porosity, other measures have to be taken to avoid or eliminate these pores. Some possibilities are:

- Design and build a bigger part, and finish it to its correct dimensions by milling or another post-processing step. In that way, the pores at the border are removed during milling. For simple geometries this could be a solution, but often Additive Manufacturing finds its applications in complex shapes.

- Alter the parameters of the remelting step so the melt pool during remelting is deeper and the gas bubbles that were formed during SLM can escape during remelting. However, in order to create such a deep melt pool without creating a new keyhole pore, both the laser power and the scan speed have to be increased.
- Avoid keyhole pores in the beginning of a scan vector by changing the scan strategy. If the laser beam already reaches the nominal speed at the beginning of a scan vector, the nominal energy density is applied and keyhole pores are avoided. For the laser to reach its nominal speed at the beginning of a scan vector, so-called '*skywriting*' or '*ghost-vectors*' can be applied. This principle is demonstrated in Figure 4.26. The scan vector is shown by a solid line (blue). The dashed green line presents the ghost vector. A ghost vector is added before every scan vector, in order for the scan speed to reach its nominal value. The laser power is turned off for ghost vectors, and turned on for scan vectors.

Figure 4.26: The principle of ghost vectors.

4.8 Heat treatment optimization

A standard heat treatment for A360.0 is the T6 heat treatment, including annealing and aging, leading to the formation of Mg_2Si precipitates. For SLM parts however, superior mechanical properties (high hardness and strength) are reached in the as-built condition, due to the very fine cellular microstructure which is inherent to the SLM process. As an annealing step would undo this fine microstructure, the T6 temper is not an optimal heat treatment for SLM produced parts. In this section, the influence of annealing, aging and the combination of both at different temperatures and duration, on the hardness of the final part is investigated.

In high pressure die casting of A360.0, the as-cast hardness of 100 ± 5 HV can be increased to 130 HV by the T6 temper. This heat treatment includes 8 hours of solution annealing at 540 °C followed by quenching in air or water and an aging step of 6 hours at 175 °C. In the annealing step, the precipitating elements (Mg, Si) are brought into solid solution. This step takes relatively long, in order to get a homogeneous distribution. Afterwards, the part is quenched in air or water. Because of the rapid cooling, the precipitating elements do not have time to precipitate and the homogeneous distribution in solid solution remains, with a hardness of about 60-70 HV [99]. The final step is the age hardening step. The temperature for age hardening should be high enough for diffusion, but below the solvus temperature to prevent solutioning. Finely distributed Mg_2Si precipitates are formed which harden and strengthen the material. The final hardness is about 130 HV.

In SLM, the as-built parts already have a hardness of 127 ± 2 HV because of the fine distribution of the silicon phase. When a conventional T6 heat treatment is performed on SLM parts, the hardness is lowered to 113 ± 2 HV. Due to the solution annealing, the very fine distribution of Si phase that was created during the SLM process is nullified. It can be concluded that the T6 temper is not the appropriate heat treatment for SLM produced parts. A proper heat treatment for SLM parts is found by applying solely an aging or a solutioning step, and measuring the resulting micro-hardness. The results hereof are depicted in Figure 4.27. The temperatures for aging and solutioning are kept the same as in the conventional T6 temper: solutioning at 540 °C and aging at 175 °C.

When only a solution annealing step is performed, the hardness is lowered from 130 HV to 92 HV for 4 hours of annealing, or even 87 HV for 8 hours of annealing. The silicon particles grow in the aluminum phase and there is no longer a fine Si-distribution, leading to a lower hardness. Figure 4.28 shows the micrographs of SLM parts that were solution annealed for 4 hours and for 8 hours, compared to micrographs of samples just after SLM: Figures 4.21 and 4.22. The scan pattern of the SLM process is no longer present and the

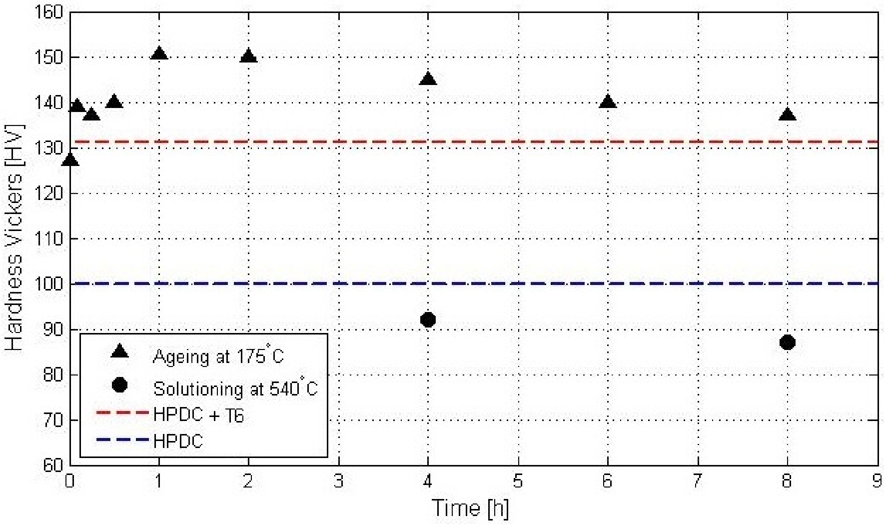

Figure 4.27: Micro-hardness measurements of A360.0 SLM parts with different heat treatments (aging an solutioning), compared to High Pressure Die Cast (HPDC) parts, with and without the T6 temper.

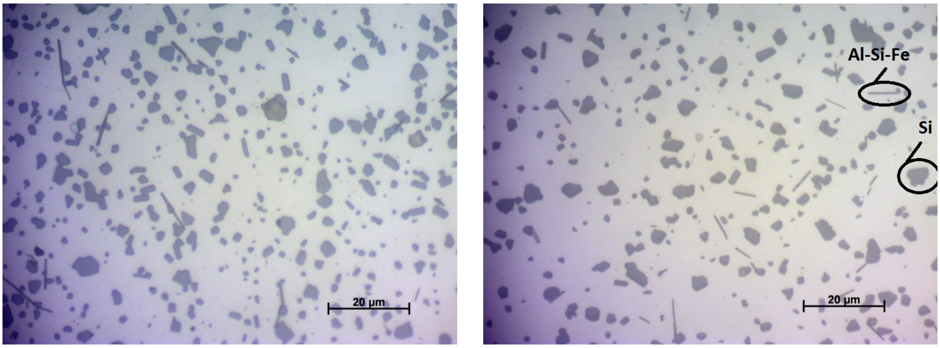

Figure 4.28: The microstructure of SLM-produced A360.0, after solution annealing for left: 4 hours, right: 8 hours

large silicon particles are spread across the aluminum phase. The needle-like phase was determined to be an Al-Si-Fe phase. A minor amount of the phases $Al_9Fe_2Si_2$, $Al_8Si_9Mg_3Fe$ can appear according to [80].

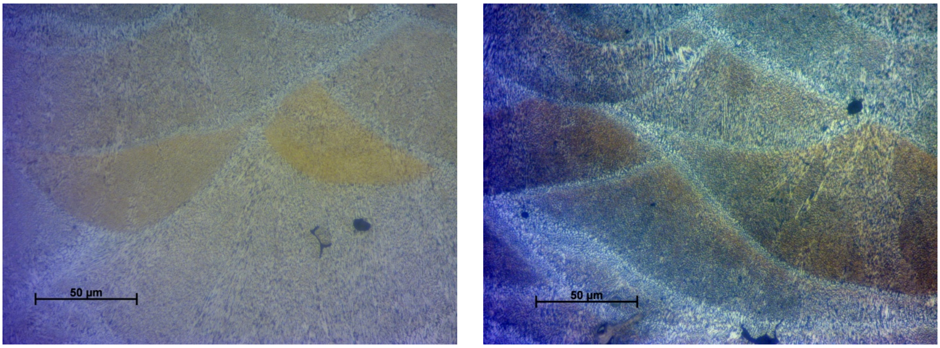

Figure 4.29: The microstructure of SLM-produced A360.0, after aging for 1 hour (left) and 4 hours (right).

Performing an aging step after SLM, without the solutioning can however increase the hardness of the SLM part. Figure 4.27 shows results for an aging step at 175 °C for 5 minutes, 15 minutes, 30 minutes and 1, 2, 4, 6 and 8 hours. The maximum hardness of 150 ± 6 is reached after aging for 1 hour at 175 °C. The microstructure after aging (Figure 4.29), still shows the footprint of the SLM process as no solutioning took place: the laser scan tracks and resulting heat affected zones with coarser microstructure are observed in the cross-sectional view.

Aging for longer than 1 hour results in over-aging. Upon over-aging, the precipitates coarsen and are no longer finely distributed, resulting in a lower hardness [66]. In Figure 4.30, the microstructure is shown for aging at 175 °C for 1 hour, which is the optimum, and for 6 hours, which is an over-aging condition. It is shown that the microstructure in the over-aging condition has coarsened compared to the part that was only aged for 1 hour.

It can be concluded that the optimal heat treatment for SLM parts differs from the conventionally defined heat treatment, because of the very fine microstruture that is reached during SLM processing. For A360.0 aluminum alloy, the as-built hardness of 127 HV can be increased to 150 HV by aging the material for 1 hour at 175 °C.

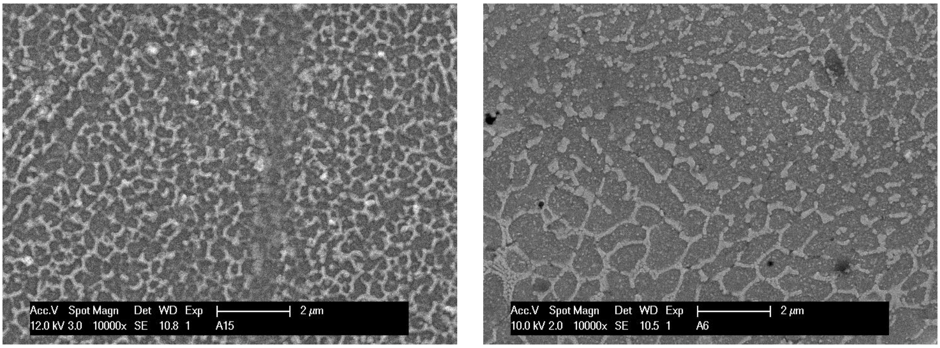

Figure 4.30: The microstructure of SLM-produced A360.0, after aging for 1 hour (left) and 6 hours (right).

4.9 Dimensional Accuracy

In the SLM process, extensive quality control is often required for various high-end applications in medical, automotive and aeronautical industries. By Computed Tomography (CT), internal features can be measured in a non-destructive manner, which makes this measuring technique utterly suitable for SLM-produced parts. This section will indicate the structural error between the dimensions of the design and the final product for internal circular and flat overhanging features in SLM of A360.0.

4.9.1 Stepped circular channels

Test bars with dimensions of 80 x 20 x 10 mm were produced in A360.0, using optimal density parameters, without laser remelting. The test bars contain internal channels with diameters ranging from 0.4 to 4 mm in different steps. A simplified sketch of the cross section of these designed channels is given in Figure 4.32. Note that this sketch is simplified, the final part design has channel diameters ranging from 0.4 mm to 4 mm in steps of 0.2 mm. Test bars were produced in both XY-orientation and Z-orientation (Figure 4.31). For easier interpretation of the final results, laser tool path compensation was turned off for the production of these parts. For standard part production on the LM-Q machine, this laser tool path compensation is set to 40 μm, which is the laser spot radius.

Figure 4.31: Design of test bars, produced in both Z-direction (left) and XY-direction (right).

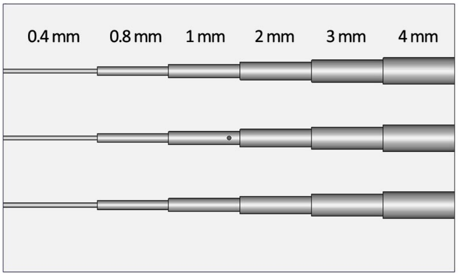

Figure 4.32: Simplified sketch of the cross section of the designed channels. The produced part has channel diameters ranging from 0.4 mm to 4 mm in steps of 0.2 mm.

For dimensional metrology of the inner cavities, a Nikon Metrology XT H450 CT scanner was employed. With a voltage ranging up to 450 kV, this CT scanner is well equipped for penetrating thicker structures and materials with a high attenuation coefficient compared to standard CT scanners for dimensional metrology [83, 169]. As a second measuring technique, a Mitutoyo QuickVision optical coordinate measuring machine was used. This technique is only employed for imaging and verification, since this requires a destructive approach.
By CT metrology, the diameters and roundness of all channels were determined. Later, the test bars were cut perpendicular to the channels. These internal channels were verified by Quick Vision optical measurement. Here the diameters

of the maximum inscribed and minimum circumscribed circles were measured to get an indication of the deviation of the channels from their designed circular shape and dimensions. The peak-to-valley roundness deviation R of the channels was determined by calculating the difference between the radius of the minimum circumscribed circle $r_{min,circ}$ and the radius of the maximum inscribed circle $r_{max,insc}$, according to ISO standard 12181. In this work, the peak-to-valley roundness deviation will be shortly referred to as roundness R, and is indicated in mm.

$$R = r_{min,circ} - r_{max,insc}[mm] \tag{4.5}$$

Figure 4.33 indicates the dimensional error on channels that were produced vertically, measured both by CT and optically. A first observation shows that the results by both measuring techniques correlate very well. The error is independent of the designed diameter. Every channel diameter is about 150 μm smaller than the designed diameter. This is due to the lack of laser tool path compensation on one hand (which is about 40 μm, like we anticipated), and lack of compensation for the melt pool width on the other hand. As the CAD design calculates the laser path to be followed, it does not take the width of the melt pool into account. The contours of the CAD data indicate the path of the center of the laser spot. While the formed melt pool has a width of 120 μm to 150 μm (for A360.0 in these processing conditions), the actual contour of the part will be shifted by 60 μm to 75 μm. For inner circular shaped features, this results in a diameter decrease of 120 μm to 150 μm. For this material and these processing parameters, we can conclude that a total compensation offset (laser spot radius + melt pool width compensation) of 150 μm is needed during contour tool path generation, instead of just the contour offset of the laser spot radius.

Unlike the good correlation between optical measurement and CT measurement in the vertical channels, this seems not to be the case for the horizontal channels, as concluded from Figure 4.34. This discrepancy is elucidated by observing the cross sections for each channel in each building direction in Figure 4.35 (Note that this is only one cross section of a 16 mm-long channel, thus not showing an overall representation of the entire channel).

The horizontally produced channels strongly deviate from their designed circular shape, which is not the case for the vertically produced channels. It is clear that for horizontal channels, another phenomenon has an important influence on the channel's dimensional accuracy.

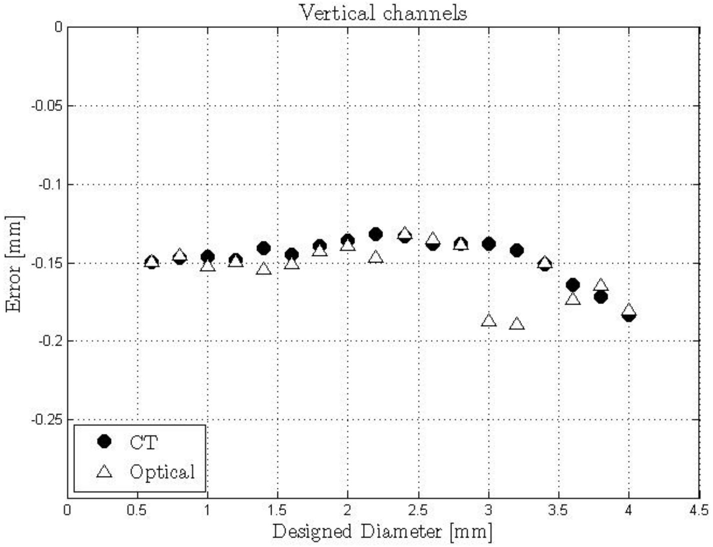

Figure 4.33: Dimensional error on vertically produced channels.

A quantification of this form deviation in horizontal channels was done by optical measurement. The diameters of the maximum inscribed and the minimum circumscribed circle were measured. From Figure 4.34 we can see that the minimum circumscribed circle is about 150 μm bigger in diameter than the maximum inscribed circle. Because this difference in inner and outer diameter is consistent for all designed channel diameters, we can conclude that the dross formation, which is causing this roundness error, is independent of the channel's dimensions. However, as can be seen from the optical images in Figure 4.35, the proportional error becomes smaller for bigger channels.

The origin of this form deviation on horizontal channels is undoubtedly the dross that was formed at the top of the circular hole. Because in horizontal channels, the top layers of the cavity are scanned on loose powder, there is a different kind of heat dissipation than when a layer is scanned on a previously solidified layer. When scanning on loose powder material, the melt pool sinks deep into the powder material and leads to dross formation. This dross formation in so-called '*down-facing structures*' is a phenomenon that is very hard to control due to the random nature of the powder particles' packing, leading to a varying heat conductivity.

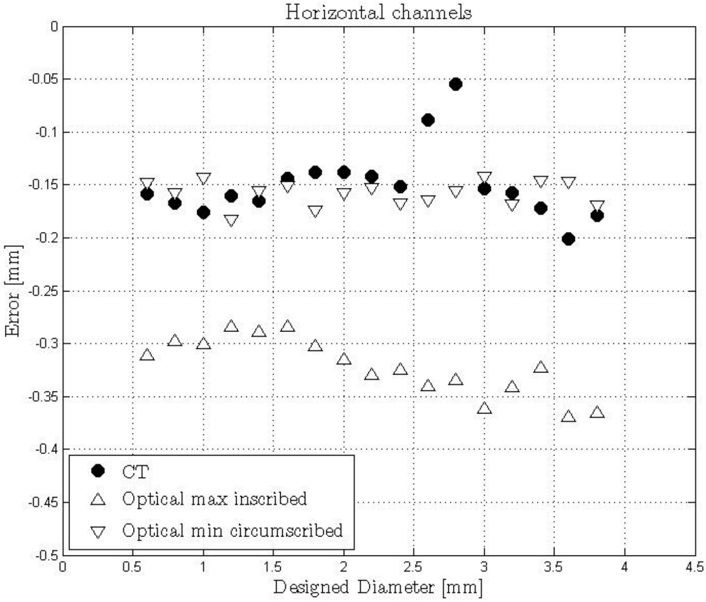

Figure 4.34: Dimensional error on horizontally produced channels.

Compared to the total offset compensation that was used to compensate the dimensional error in vertically built channels, this problem however is harder to solve. Possible solutions are: i) re-orientation of the part, ii) shape compensation, iii) parameter adaptation or iv) re-design of the part.

Re-orientation of the part This does not include any functional changes to the part's design, only a rotation of the part with respect to the baseplate. By re-orientation of the part, the manufacturer can avoid horizontal channels. A good example is the test part in Figure 4.31. Building the part in XY-direction is hard, because then, all channels are built horizontally. By rotating the part 90 ° over the x-axis, all channels can be built vertically, and thus with higher dimensional accuracy.

Shape compensation Because the depth of the dross formation can be measured, and in a further state perhaps even predicted based on process parameters, material, environment, etc., one could compensate for the dross

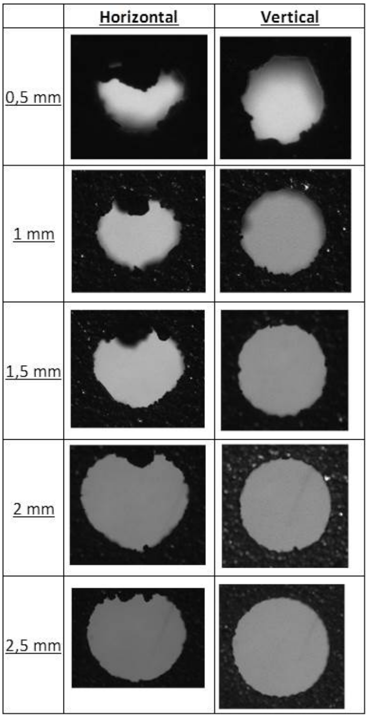

Figure 4.35: Optical cross section of all channels produced in two directions.

formation in the shape design. For instance: design of an egg shape, that with the formation of dross, would result in a circular shape.

Parameter adaptation Another way of tackling this problem is by trying to minimize or avoid the dross formation by parameter optimization. Dross can be minimized by forming a melt pool that is less deep. This can be done by lowering the laser power, or by increasing the scan speed, so that the energy input is lowered. Optimization of parameters for downfacing structures is discussed later in subsection 4.9.2.

Re-design of the part If all other options fail, the designer could re-design the part in such a manner that it still fits the customer's requirements, but that horizontal channels are avoided.

4.9.2 Downfacing areas

Since downfacing areas are scanned on multiple layers of loose powder (instead of on solidified material), their melt pool behavior is different. Due to the lower (and non-uniform) heat conductivity of the powder, the melt pool becomes unstable and deep if the scan strategy is not optimized, resulting in random dross formation. Figure 4.36 shows the design of a horizontal downfacing area (left), and the resulting dross formation if no parameter optimization is applied (right).

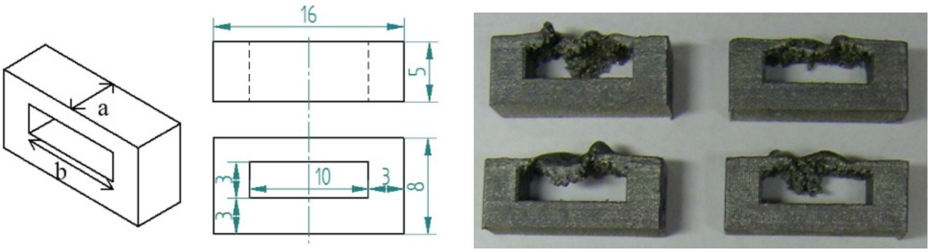

Figure 4.36: The design of a horizontal downfacing area (left), and the resulting dross formation if no parameter optimization is applied (right).

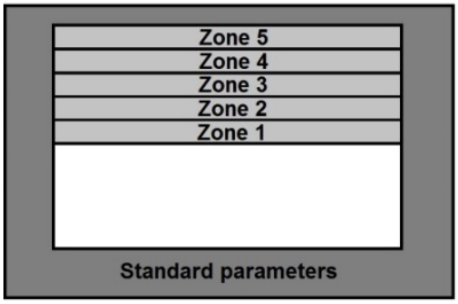

Figure 4.37: Volume above downfacing surface is divided into 5 zones, each allocated with a different parameter set.

The area above the downfacing surface is divided into five zones, as demonstrated in Figure 4.37. Each zone consists of multiple layers and they all have an adapted parameter set, so a stable melt pool can be formed. In order to define the right parameters for every zone, the set for the first zone was estimated based on heat flux simulations and previous research on downfacings in Ti6Al4V [34]. The parameters for the following zones make a smooth transition to the standard parameters for optimal density.

In this approach, the laser power P is optimized, and the scan speed v is kept constant at 1400 mm/s to guarantee a certain level of productivity. The goal is to form a melt pool approaching the same shape, depth and width of a melt pool that was formed during processing on upfacing surfaces [76, 107]. These dimensions were measured in section 4.5. By using a thermal model simulation, developed by Verhaeghe et al. [162], the depth and width of the melt pool were simulated for downfacing structures in A360.0, for different laser powers. The results of these simulations are shown in Figure 4.38. Note that this model does not simulate the melt pool height and contact angle. These requirements are not taken into account here.
A simulation of scanning one power layer on top of solidified material is shown in the left picture. It confirms the dimensions (width, depth) or the melt pool as measured in 4.5.

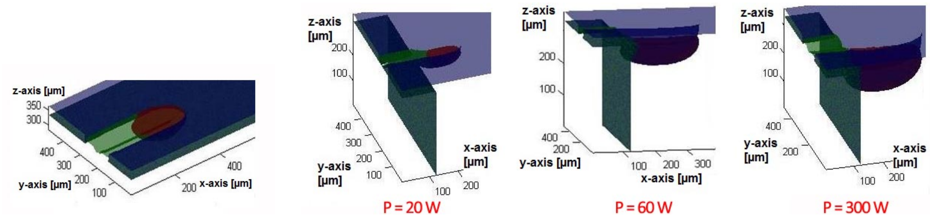

Figure 4.38: Simulation results: Normal scanning situation on solidified material (left), downfacing scanning at different laser powers (right). Green: solidified material; Red: melt; Blue: powder material.

These simulations indicate that a laser power of 60 W and a scan speed of 1400 mm/s on a downfacing surface result in a similar melt pool shape as a laser power of 200 W and a scan speed of 1400 mm/s on an upfacing surface.
By experimental validation, several laser powers between 40 W and 90 W were tested on downfacing surfaces. Outside these values, part production fails due to curling up of the downfacing layers. The downfacings surfaces were cut in longitudinal direction, and analyzed by Light Optical Microscopy. The images for varying laser power are depicted in Figure 4.39.

When the laser power of the first zone is too low, no powder is molten. On the other hand, when power is too high, large irregular lumps are formed. These

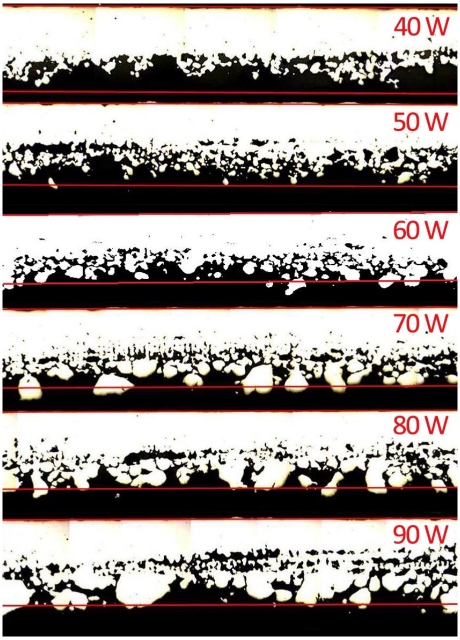

Figure 4.39: Comparison of varying laser power used in zone 1. The red lines indicate the borders of the designed downfacing area. The total length depicted is 10 mm.

lumps lower the surface quality and can cause problems in post-processing like sandblasting or etching. Similar to what the simulations suggest, 60 W appears to be a good laser power for the first zone in a downfacing area. Powder is molten in the first downfacing layers, without large lump formation.

Parameters for the following zones are obtained by making a smooth transition to the optimized parameters for upfacing surfaces. The optimal scan strategy for horizontal downfacing structures is displayed in Table 4.9. The laser power is increased in every zone. As the density of every zone increases, the required laser power can be increased to form a stable melt pool. Because of the increase in laser power, the scan spacing has to be larger in zone 2 in comparison to zone 1. Every zone consists of ten layers to obtain the required process stability.

Figure 4.40 shows the result of building a 10 mm downfacing surface with the adapted parameters. Dross formation is avoided and dimensional accuracy is improved. A horizontal downfacing surface is the most critical situation. Inclined

Table 4.9: Optimized parameter set for downfacing areas in A360.0 aluminum, with scan speed v = 1400 mm/s.

	Z1	Z2	Z3	Z4	Z5	Standard parameters
Laser power P [W]	60	90	120	150	220	300
Scan spacing h [μm]	20	110	110	110	110	110
# of layers	10	10	10	10	10	rest

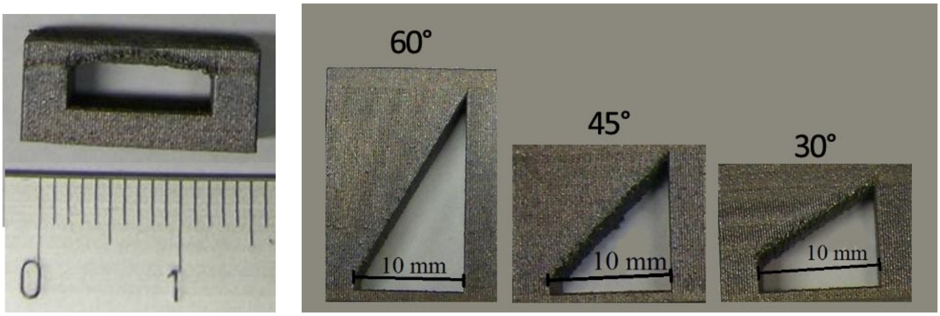

Figure 4.40: Parts with downfacing surfaces, produced with the optimized scan strategy. Horizontal surface (left) and inclined surfaces (right).

downfacing surfaces are overall easier to process. Surfaces with inclination angles above 45 ° are generally known to be feasible by SLM. Inclination angles below 45 ° are produced with a similar scan strategy as described above, but limited to only three zones, as depicted in Figure 4.41

4.10 Conclusions

1. Chemical composition, powder shape and size distribution are critical for the powder layer deposition and thus for the quality of the produced part. The amount of silicon in the A360.0 alloy influences the laser absorption, leading to changes in the melting behavior. Two types of powder material were compared based on chemical composition, particle size distribution and particle morphology. It was shown that the powder with a spherical morphology, a broad particle size distribution and a sufficient amount

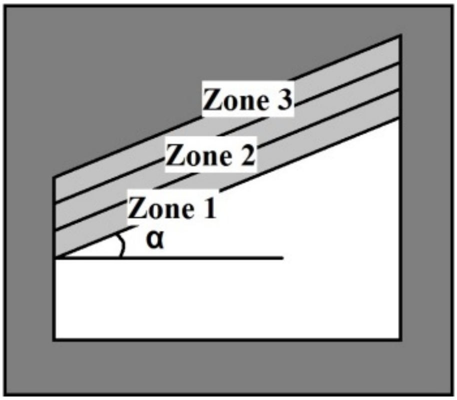

Figure 4.41: Scan strategy of 3 zones for an inclined area with inclination angle α.

of silicon leads to higher density parts. This powder was selected for all further testing.

2. Single track scans offer a great amount of information on the formation of a melt pool and its characteristics. A low energy input per unit length results in droplet formation and a bad wetting to the previous layers or to the baseplate for the first layer. An energy input per unit length that is too high, causes a very deep melt pool and possibly keyhole porosity. The optimal energy input per unit length for SLM of A360.0 in these processing conditions (machine and atmosphere parameters) lies between 140 and 160 J/mm. These borders in the P-v graph mark the process window, where a stable melt pool is formed that meets all the set requirements.
   Similar to results reported by Mumtaz et al. on SLM of waspalloy [112], the melt pool width and height decrease for increasing scan speed. The effect of balling at low energy density in SLM of powder mixtures of Al-12%Si and Al-10%Mg was also reported by Olakanmi et al. [123] and Savalani et al.[116] respectively. Olakanmi et al. also set up a process map based on single track scans, resulting in a graph with 4 zones: no marking, partial marking, good consolidation and excessive balling. The zone of 'no marking' was not noted in this work, as it would be located at lower laser power and lower scan speed. The zone of good consolidation also widens for a greater laser power, as was reported in this work.

3. Optimal density parameters lie within the previously defined process window. As mentioned before, this process window is defined by a zone between two linear boundaries in the P-v graph (Figure 4.12):

$P = E_{l,min} * v$ and $P = E_{l,max} * v$. As E_l represents the slope in the P-v graph, the process window becomes broader for high laser powers. A parameter set is defined for producing high density A360.0 parts by SLM with highest productivity. Parts with a density up to 99.4 % were produced. Similar density values are obtained by Manfredi et al. [100] and Calignano et al. [26] upon processing of A360.0 by SLM. Both report different optimal parameters, but upon calculation, both use an energy per unit length of 133 J/mm, which closely approximates the optimal energy density reported here.

The effect of process parameters like laser power and scan speed on the top surface roughness was investigated. For a given laser power, the surface roughness value P_a reaches a minimum at a certain scan speed (Figure 4.13). The higher the laser power, the lower the optimal scan speed in terms of top surface roughness. For an increasing energy density, the surface quality will improve as long as the melt pool is stable. Once the keyhole instabilities start to take place, the roughness strongly increases. The parameter set for optimal density only differs slightly from the optimal parameter set for good top surface quality.

Density could be improved by optimizing the scan spacing between the scan tracks. When the scan spacing is too large, the scan tracks will not connect, and unmolten powder will remain between the scan tracks. This results in both a very low density and a rough top surface. For a very low scan spacing, the production time strongly increases and it could lead to pores if the scan track lies within the denudation zone of the adjacent track.

Calignano et al. [26] have shown that the scan spacing influences the surface roughness in SLM of A360.0, but to a lesser extent than the scan speed which influences the roughness the most. In the work of Calignano et al, the average roughness values of as-built A360.0 parts range between 14 and 24 μm for similar process parameters to this work. These results are in line with the results reported here. In Buchbinder et al. [24], high density parts are produced at very high laser power (500 - 700 - 900 W). The range of applied scan speed doesn't differ very much from the range reported here, but the layer thickness, scan spacing and beam size are much larger. The volumetric energy density is comparable leading to stable processing conditions, but the productivity is strongly improved.

The effect of scan spacing on part density was also investigated by Yadroitsev et al [182] and Louvis et al. [96]. As was also concluded here, the part density reaches an optimum at a certain scan spacing.

Remelting every layer has proven to significantly increase the density up to 99.8%, and improves the surface roughness, if remelting parameters are chosen properly. A lower scan spacing is needed because the melt pool is more narrow due to a different heat flux. Remelting however has serious implications on the total production time.

4. The mechanical properties like Ultimate Tensile Strength, elongation at fracture and micro-hardness in the as-built condition are comparable or even exceed those of high pressure die cast parts which underwent a heat treatment. Performing an aging step of 6 hours at 175°C can even further increase the hardness of the SLM parts to 152 ± 5 HV.
   In Manfredi et al. [100], a hardness of only 108 HV and UTS of 303 MPa was reported, which could be attributed to the lower density in their work. Buchbinder et al. [24] reports hardness values of 147 HV and UTS of 400 MPa, similar to this work.
   Not only in SLM of aluminum alloys, but also in other materials like Ti6Al4V [114] and 316L stainless steel [103] the mechanical properties meet or exceed those of conventionally produced parts due to the high thermal gradients and resulting fine microstructure that are inherent to the SLM process.

5. Macrostructural analysis showed that both irregular and smaller spherical pores remain in the nearly full dense parts. The cellular microstructure was shown to be finer in the center of the melt pool and more coarse at the melt pool boundary. Manfredi et al. [100] and Ma et al. [98] observed a similar microstructure after SLM of A360.0.

6. The standard heat treatment for A360.0 is the T6 heat treatment, including annealing and aging, leading to the formation of Mg_2Si precipitates. For SLM parts however, superior mechanical properties (high hardness of 127 HV and strength) are reached in the as-built condition, due to the very fine cellular microstructure which is inherent to the SLM process. As an annealing step would undo this fine microstructure, the T6 temper is not an optimal heat treatment for SLM produced parts. It lowers the hardness to 113 HV. The proper heat treatment for SLM parts is found by applying solely an aging step of 1 hour at 175 °C. It increases the hardness of the as-produced SLM parts from 127 HV to 150 HV. Aging for a longer time results in over-aging, decreasing the hardness. This was also reported by Vojtech et al., on casting of high-strength aluminum alloys [163].
   Brandl et al. [20] also performed heat treatments on SLM produced A360.0 parts. It was also shown that aging does not change the microstructure; the dendrites, laser tracks and Heat Affected Zone are still distinguishable. Just like shown in the micrographs in this work, the T6 temper results in a homogeneous microstructure with coarsened silicon particles.

7. Vertically produced channels have to be compensated by both the laser radius and the width of the melt pool, since the contours of the CAD

data indicate the movement of the center of the laser beam, and not the border of the melt pool. This compensation factor depends on the melt pool width, and thus on the process parameters and the powder material. For horizontally produced channels, the same compensation factor for the laser radius and the width of the melt pool has to be applied. On top of that, a form error is induced by dross formation. The amount of dross formation is dependent on the base material and the applied process parameters, but dross formation is irregular in shape and thus hard to compensate.
   Four possible ways to deal with dross formation are: re-orientation of the part, shape compensation, parameter adaptation and re-design of the final part.

8. For the production of horizontal downfacing areas, parameters have to be optimized in order to prevent dross formation. A melt pool with a similar shape and size as during standard processing is formed at a lower laser power of 60 W, due to the difference in heat flow in powder, compared to solid material. To ensure a good transition from downfacing parameters to standard parameters, the volume above the downfacing area is divided into five different zones, with transitioning scan parameters. The method has shown to be successful for both horizontal downfacings, and inclined downfacings, where three zones are sufficient.
   A similar strategy for parameter optimization for downfacing areas is employed by Clijsters et al. [34] for Ti6Al4V.

Chapter 5

Wrought aluminum alloy 7075 (AlZnMgCu1.5)

The second aluminum alloy is a wrought aluminum alloy 7075 that was selected for its good combination of high thermal conductivity and high strength. This alloy has a larger solidification range and worse castability, which is expected to result in some difficulties in processing by SLM. The main goal of this chapter is not to do a full characterization of the SLM-produced material like in the previous chapter, but to emphasize the difference in processing cast and wrought aluminum alloys.

The most relevant material properties of 7075 are summarized in section 5.2, and a short overview of the challenges in processing this material by SLM is given in section 5.3.

For 7075, the production of fully dense parts has proven to be more challenging, as shown in section 5.4.2. Solutions are proposed to avoid the crack formation in the parts. The conclusions of this chapter are summarized in section 5.5.

5.1 Introduction

In this work, an aluminum alloy of the 7000 series is selected for its combination of high strength and high thermal conductivity. The 7075 alloy can find its applications in aircraft fittings, gears and shafts, missile parts, regulating valve parts, worm gears, heat exchangers, keys, aircraft, aerospace and defense applications, bike frames, etc . . . and other highly stressed structural applications.

5.2 Material Properties

The **chemical composition** of the aluminum 7075 alloy according to ASM handbooks and ANSI is given in Table 5.1.

	Al	Si	Cu	Mn	Mg	Zn	Fe
wt%	Bal.	0.4	1.2 - 2	0.3	2.1 - 2.9	5.1 - 6.4	0.5

Table 5.1: Chemical composition of 7075 aluminum alloy, according to ASM [9]

The major alloying elements are **zinc** and **magnesium**. Magnesium in combination with silicon forms the hardening phase Mg_2Si. The low amount of silicon in this alloy predicts a high thermal expansion coefficient and a reduced fluidity.
Zinc as an alloying element has no real effect on its own, but in combination with copper and magnesium, natural aging can occur or the alloy becomes heat treatable.

Al 7075 is typically hardened by the T6 temper cycle, similar to the A360 cast alloy discussed in the previous chapter. For Al 7075, annealing happens at 415 °C and aging at 120 °C.
The physical and mechanical properties of Al 7075 are summarized in Table 5.2. A comparison is made between conventionally wrought and wrought + T6 heat treated material.

	Conventionally Wrought	**Wrought + T6**
Young's modulus E [GPa]	71	71
Ultimate Tensile Strength UTS [MPa]	228	572
Elongation at break ϵ [%]	17	11
Hardness Brinell [HB]	60	150
Density ρ [g/cm^3]	2.80	
Solidification Range [$^\circ C$]	635 - 477	
Thermal conductivity λ_{therm} **[W/mK]**	130	
Thermal expansion coefficient α_L [$10^{-6}/K$]	21.6	

Table 5.2: Mechanical and physical properties of wrought and T6 heat treated, 7075 aluminum parts [9]

5.3 Challenges

Production of 7075 SLM parts could open new application possibilities, for example in high-strength lightweight components in aeronautic industries. This alloy however is not a casting alloy and is thus not designed to be shaped in a liquid state.

Preliminary tests of SLM of 7075 with scan parameters similar to the optimized parameters for SLM of A360 aluminum alloy, showed that only 95 % density can be obtained because of crack formation. A cross section of these parts in the YZ plane is shown in Figure 5.1.

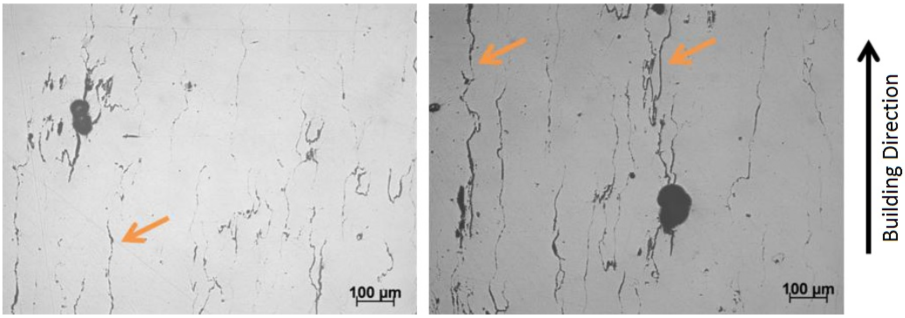

Figure 5.1: The YZ cross section of 7075 parts produced with laser power P = 200 W, scan spacing h = 105 μm and scan speed 1400 mm/s. The arrows indicate the cracks that form in the building direction.

The presence of cracks has been seen in other materials produced by SLM such as M2 HSS [95], which will be discussed in Chapter 7 and Tungsten [145]. In Chapter 7 cracks are avoided by use of a pre-heating system. In this chapter, cracks will be avoided by adding silicon. The goal is to eliminate cracks by lowering the material's thermal expansion coefficient and/or narrowing it's solidification range.

5.4 Parameter optimization

5.4.1 Addition of Si

In many aluminum alloys, silicon is added to reduce the solidification range and lower the melting temperature, which makes the alloy suitable for casting. Moreover, silicon additions are also accompanied by a reduced thermal expansion coefficient [75]. In some welding applications silicon is used as a filler material to reduce hot cracking, as it provides more eutectic to heal the cracks [176]. Moreover, the addition of an alloying element to a pre-alloyed powder has shown great advantages in SLM of Ti6Al4V where metal matrix composites are formed after addition of Mo powder [166].

In this work, pre-alloyed 7075 powder, supplied by LPW technology [97], was mixed with pure silicon powder. The 7075 powder does not have a spherical morphology(Figure 5.2 left) and has an average particle size of $d_{(v,0.5)} = 53.17$

μm. The silicon powder had an average particle size of 2.64 μm and is depicted in the right picture in Figure 5.2.

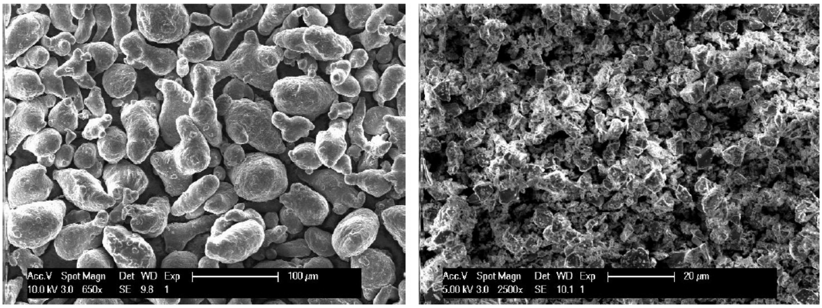

Figure 5.2: SEM image of 7075 powder (left) and pure Si powder (right).

5.4.2 Density optimization

Varying quantities of Si powder (1 - 4 %) were added to the 7075 powder to see the influence on the crack formation in the SLM produced parts. For every powder mixture, parts were produced with a range of scan speed (1000 - 1600 mm/s) and laser power (225 - 300 W), and a hatch spacing of 105 μm, on the LM-Q machine. For the powder mixtures with 3% and 4% of silicon, the 300 W parts were scanned with an island scanning strategy. All other parts were scanned using a zig-zag scanning strategy.
The evolution of the part density (measured by Archimedes method) and cracks were observed. The primary goal is to produce crack-free parts, the secondary to produce fully dense parts.

The following images (Figure 5.3 - Figure 5.10) show the micrographs of the YZ cross sections and the measured density values for different powder mixtures: 1%, 2%, 3% and 4% of Si.

7075 + 1% Si

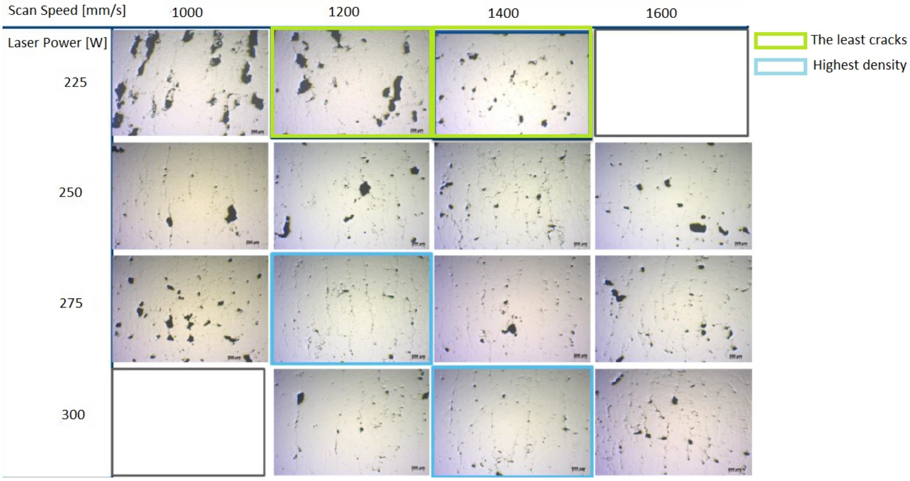

Figure 5.3: Micrographs of the YZ cross sections for 7075 + 1 % Si, produced with different laser power and scan speeds.

Figure 5.4: Relative density for 7075 + 1 % Si, produced with different laser power and scan speeds.

7075 + 2% Si

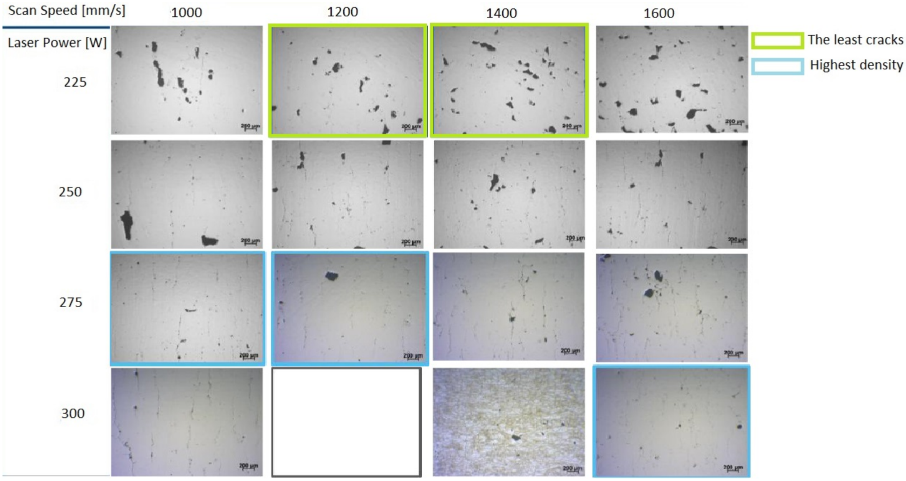

Figure 5.5: Micrographs of the YZ cross sections for 7075 + 2 % Si, produced with different laser power and scan speeds.

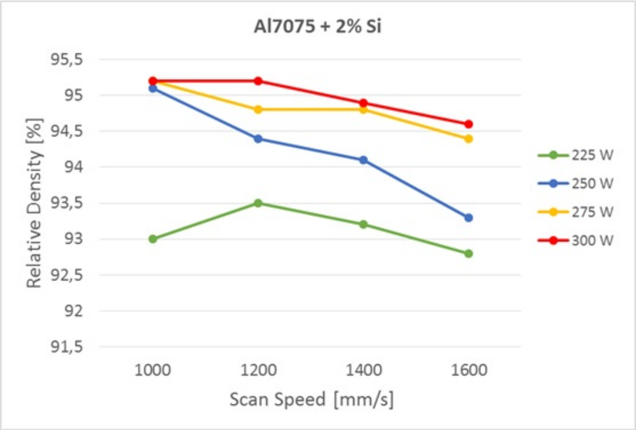

Figure 5.6: Relative density for 7075 + 2 % Si, produced with different laser power and scan speeds.

7075 + 3% Si

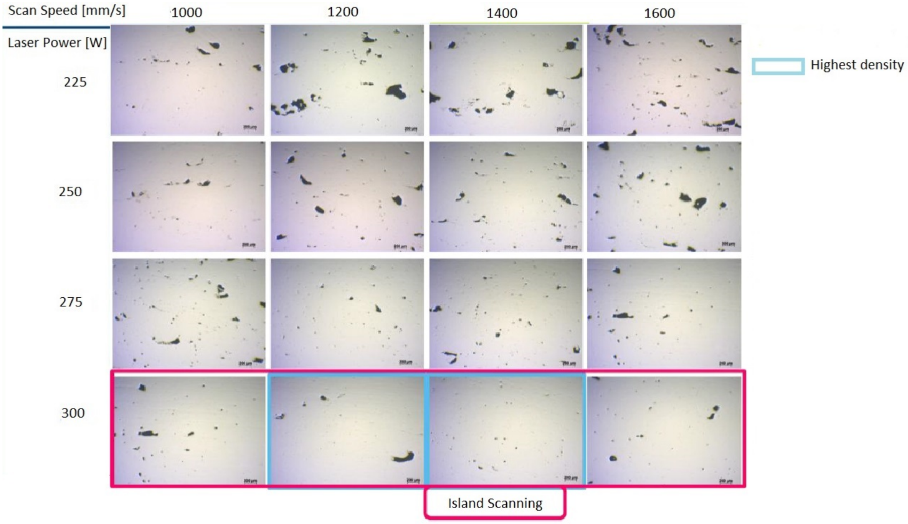

Figure 5.7: Micrographs of the YZ cross sections for 7075 + 3 % Si, produced with different laser power and scan speeds. The blue square indicates the parts with the highest density.

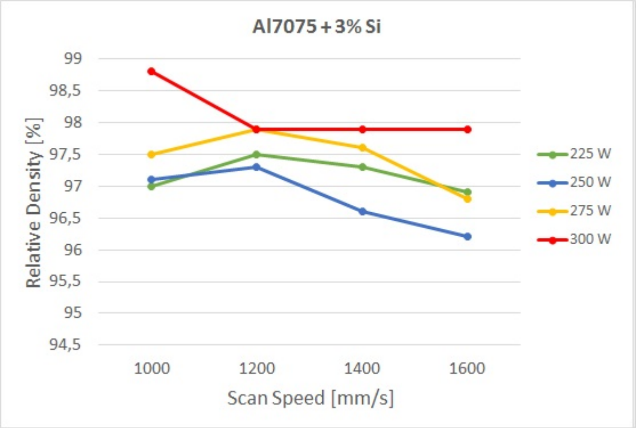

Figure 5.8: Relative density for 7075 + 3 % Si, produced with different laser power and scan speeds.

7075 + 4% Si

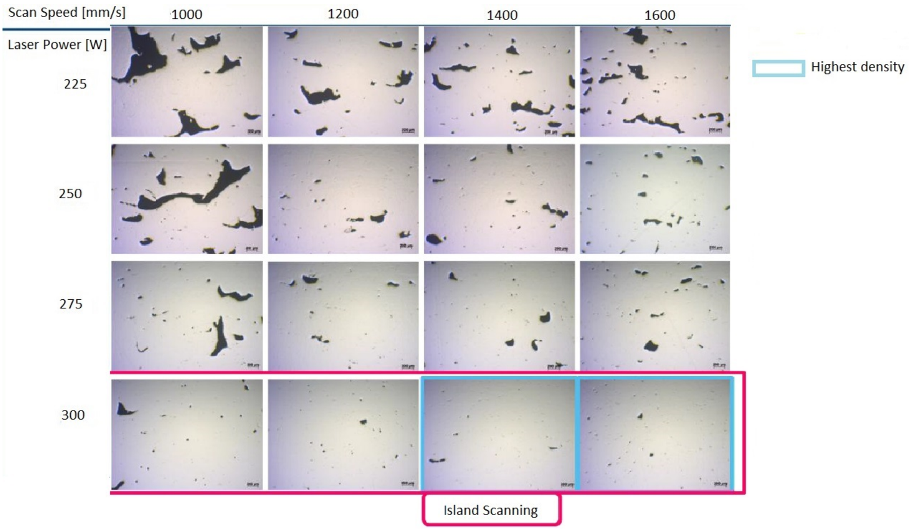

Figure 5.9: Micrographs of the YZ cross sections for 7075 + 4 % Si, produced with different laser power and scan speeds.

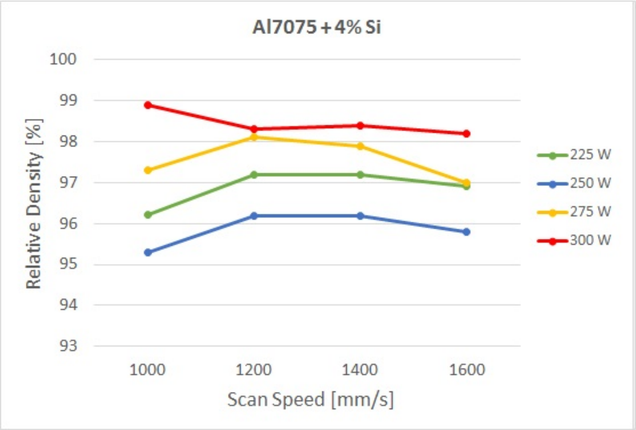

Figure 5.10: Relative density for 7075 + 4 % Si, produced with different laser power and scan speeds.

The parts produced with **1% of silicon** show an increasing density for higher laser powers, but are still very porous as they only reach a maximal density of about 95 %.
Cracks are still present in all the produced samples. The parts produced with low laser power show less cracks, but the amount of porosity is highest. The many pores are connected by the vertical cracks which suggests that the stresses are released through them.

After adding **2% of silicon** to the 7075 powder, the maximal reached density is 95.2 %, which is slightly higher than the maximal density reached in the parts produced with 1% of Si, but is still too low for qualitative part production. In these density graphs as well, a higher energy density (high laser power, low scan speed) results in less porosity.
All the parts still contain cracks. High porosity parts have fewer cracks as the stresses are released through them.

Like in the parts with 1% and 2% of silicon, the highest density in parts with **3% of silicon** is also reached for the part produced with the highest energy density (300 W and 1000 mm/s). However, the addition of 3% of Si leads to a relatively much higher density of 98.8 %.
Also, no cracks were detected in any of these parts with 3% of silicon, which is an important difference between 2% and 3% of Si.

The **4% silicon** parts reach a maximal density of 98.9%, which is slightly higher than the 3% Si parts. For a scan speed of 1000 mm/s, large pores are formed due to bad laser alignment, causing a reduced laser power. No cracks were observed in any of the parts produced with 4% of silicon.

5.5 Conclusions

Low additions of silicon (1%, 2%) showed a high percentage of cracks parallel to the building direction. In addition, the maximum density reached was about 95 %.
For higher additions of silicon (3% and 4%), the cracks are no longer observed and the density increases to 98.9%.

This research of the 7075 aluminum alloy has shown the capability to process this alloy by SLM. No cracks were observed after adding 3% and 4% of silicon powder to the powder mixture. The density of the parts however, can still be improved, which is crucial for the production of mechanical test parts or high quality applications. Further densification could be obtained by for instance laser remelting after every or a few layers, optimization of the hatch spacing or further decrease of scan speed (below 1000 mm/s).

Mechanical properties were not tested in the scope of this thesis , but are expected to be influenced by the addition of silicon. The high strength for which this material was selected will be lower after the addition of silicon, making the addition of silicon an important trade-off between high strength and crack-free production. It is for this reason that silicon additions over 4 % are not recommended.

Part II

Tool Steels

The second part of this thesis work describes the processing of two types of tool steel by SLM. The first is a maraging steel which is known for possessing high strength and toughness and good weldability. It is a low carbon steel which derives its strength from precipitation of inter-metallic compounds. Chapter 6 discusses how this material is processed by SLM to achieve nearly fully dense parts, and how the process affects the mechanical properties and microstructure of the final part.

The second tool steel is a High Speed Steel (HSS) which owes its hardness up to 65 HRC to the carbides that are formed due to the high carbon content. The research for this material is driven by the demand of industry for a very hard material, being processed by SLM. The high hardness however, goes hand in hand with a low toughness. Chapter 7 will show that processing of this high-carbon tool steel will involve more problems than processing of low-carbon maraging steels.

Chapter 6

Maraging Steel 18Ni300

Maraging steels (**mar**tensitic **aging** steels) are iron alloys which are known for possessing high strength, high toughness, good weldability and dimensional stability after aging heat treatment. These properties make the material suitable for injection molding and die casting applications. SLM of this material could enable the production of mold and dies with conformal cooling channels [117, 135] or complex shapes.

Previous work at KU Leuven by colleagues Dr. E. Yasa and Ir. S. Vandenbroeck has shown the change of part density and surface quality when the process parameters (scan speed and layer thickness) are varied. An optimal parameter set in terms of high density and productivity was defined for two different SLM equipments.

This work aims to investigate the influence of the process parameters like scan speed and layer thickness, on macro- and micro-hardness of as-built parts, as well as the effect of laser remelting. As maraging steels obtain their superior mechanical properties after heat treatment, different aging conditions were tested to obtain the highest hardness.

6.1 Material Properties

Maraging steels are a special class of low carbon high strength steels which derive their strength not from carbide formation, but from precipitation of inter-metallic compounds. The principal alloying element is 15 to 25% nickel. Secondary alloying elements are added to produce inter-metallic precipitates, which include cobalt, molybdenum, and titanium. The chemical composition of maraging steel 18Ni300 is given in Table 6.1

	Fe	Ni	Co	Mo	Ti	Al	Cr	C
wt%	Bal.	17-19	8.5-9.5	4.5-5.2	0.6-0.8	0.05-0.15	≤ 0.5	≤ 0.03

Table 6.1: Chemical composition of maraging steel 18Ni300, according to DIN 1.2709

The amount of carbon is very limited in this type of tool steel. Carbon in this alloy, is an impurity as it forms titanium carbide (TiC) films on the border of the austenite grains. This lowers the toughness, strength and corrosion resistance. In high-carbon tool steels like M2 High Speed Steel, carbides are formed, contributing to the high hardness and strength. These carbides however, lower the ductility of the material.

The term '*maraging*' is an abbreviation for '*martensitic age hardening*'. The aging of martensite is based on a uniform distribution of fine inter metallic $Ni_3(Ti, Mo)$ and Fe_2Mo precipitates that strengthen the martensitic matrix from about 35 HRC before aging to about 52 HRC after aging.
A second goal of the aging treatment is minimizing the reverse transformation of the metastable martensite to austenite. The reversion of austenite occurs after precipitation, so it is crucial to find the right temperature and time-window for hardening, in order to initiate precipitation, without starting the austenite reversion.
The cause of this reversion is the thermal hysteresis of the phase transformation between austenite and martensite. The reversion of martensite to austenite during heating occurs at a higher temperature than the transformation of austenite to martensite upon cooling. Figure 6.1 shows the metastable diagram for heating and cooling on the left hand side and the equilibrium state on the right hand side.

Martensite formation (upon cooling) Upon cooling, the fcc structure of austenite transforms to a metastable martensitic bcc structure. This transformation starts at the martensite start temperature M_s. In order to achieve a fully martensitic structure at room temperature, the M_s temperature has to be high enough. For maraging steel 18Ni300, this is about 300°C.
The alloying elements greatly influence the martensite start temperature. Most of the alloying elements in maraging steel like nickel, molybdenum and titanium lower the M_s temperature, but are necessary for age hardening of the material.

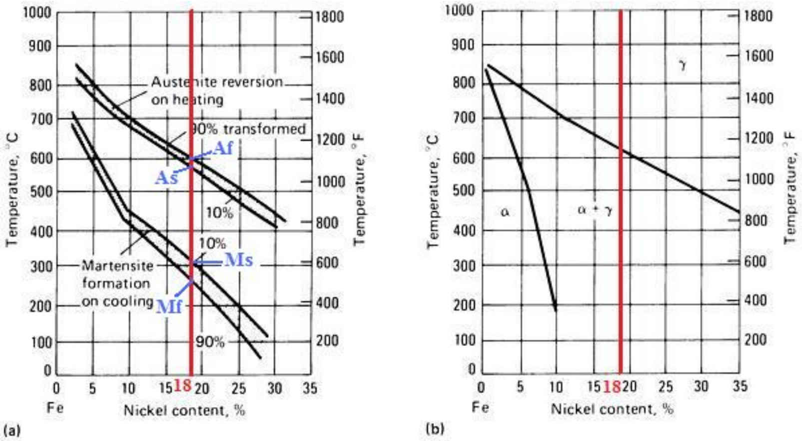

Figure 6.1: Phase transformation upon heating and cooling of maraging steel: metastable (left) and equilibrium (right) [8]. The red line indicates the composition of maraging steel 18Ni300.

Cobalt increases the M_s temperature and thus forms an important alloying element for the formation of a fully martensitic structure.

Age hardening (upon heating) Upon heating of maraging steel at low temperatures (< 450°C), the material is strengthened by forming the coherent phases. Ni-rich and Fe-rich areas arise. At higher temperatures, an intense hardening occurs due to the precipitation of $Ni_3(Ti, Mo)$ and Fe_2Mo. Heating above the austenite start temperature A_s causes a reversion to austenite.

6.2 Challenges

The material is selected for its high strength and hardness. The challenge lies in processing this material by SLM in order to make complex shapes, while keeping the superior hardness and toughness that it was selected for.

6.3 Powder Material

In the scope of this thesis, the powder material that was used was supplied by Concept Laser (CL 50 WS). The powder can be distinguished from others by granulometric properties like average particle size and particle morphology. Table 6.2 shows the average powder particle diameter $d_{v,50}$. This was determined by Malvern Mastersizer.

Particle size	**CL 50 WS**
$d_{v,50}$ [μm]	34.7

Table 6.2: Average particle size for Concept Laser's CL 50 WS powder.

The Scanning Electron Microscope (SEM) images show the morphology of the powder in Figure 6.2. There is a clear spherical morphology with small satellite particles which influence the powder fluidity. The spherical morphology is beneficial for the powder packing density and powder fluidity which is important for a good powder deposition [118].

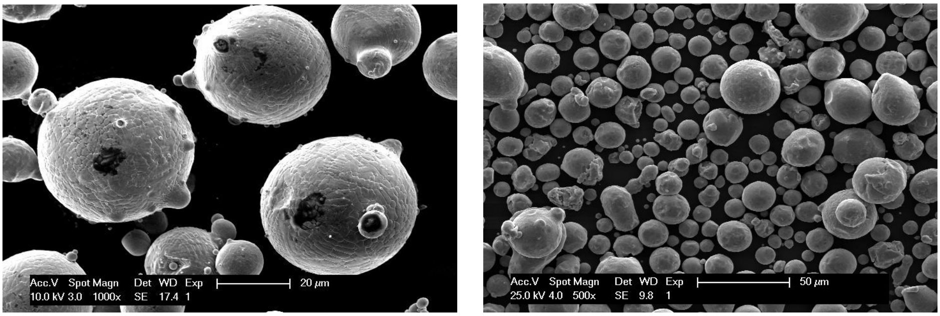

Figure 6.2: Concept Laser CL 50 WS powder, observed by SEM under two different magnifications.

6.4 Parameter optimization

Initial research at KU Leuven on SLM of maraging steel, performed by Yasa et al [183], showed that relative density reaches a maximum at a certain range

of scan speed, for all four different layer thicknesses that were tested. This trend is expected, as the delivered energy density decreases with increasing scan speed. For very low scan speeds, density is also lowered due to the formation of a rough surface as a result of excessive energy density, which in turn prevents the coater from depositing a homogeneous powder layer.
Using the CL 50 WS powder on the Concept Laser M3 machine the highest density obtained was 99.2%, using the following scan parameters: laser power 100 W (which is the maximum power of the CL M3 machine), scan speed 150 mm/s, scan spacing 111.6 μm. This thesis will continue on the work on SLM of maraging steel, using these optimized scan parameters.

6.4.1 Remelting

Influence on part density In this research, two scan strategies were researched in order to determine the best scan strategy for laser remelting. The SLM parameters (the parameters for the first scanning step) are identical for all test parts. The first set of cubes was built only by SLM (no laser remelting was applied). Upon building the second batch of test parts, laser remelting was applied by an island scanning strategy, with scan parameters as described in Table 6.3. The third set of test parts were also built applying laser remelting, but with long zig-zag scan vectors.

Figure 6.3: Macrographs of the XY cross section of a produced sample in every batch.

Figure 6.4: Macrographs of the YZ cross section of a produced sample in every batch.

As expected, the laser remelting step slightly improves the part density from 99.1 % up to 99.4 %. The difference is more clear upon observation of the macrographs in Figure 6.3 and Figure 6.4. The black dots in the images indicate the pores that are formed during processing. In observation of both the XY plane and the YZ plane, it can be seen that less porosity is formed when applying remelting.

	SLM Parameters	**Remelting Parameters**	**Relative Density**	**Micro-Hardness (HV)**
Batch 1	v=150mm/s, P=105W, a_1=0.62, a_2=0.35, a_3=0.5	no remelting	99.1 %	395.8
Batch 2	v=150mm/s, P=105W, a_1=0.62, a_2=0.35, a_3=0.5	island scanning, parameters identical to SLM parameters	99.4 %	412.6
Batch 3	v=150mm/s, P=105W, a_1=0.62, a_2=0.35, a_3=0.5	zig-zag scanning, v=100mm/s, P=105W, a_1=0.3	99.2 %	390.3

Table 6.3: Relative density and micro-hardness for parts produced with differing laser remelting strategy.

The laser remelting step after each layer also has an effect on the micro-hardness, which will be discussed in subsection 6.5.2.

6.4.2 Microstructure

The produced samples were observed under both Light Optical Microscopy (LOM), to observe the general macrostructure and the effect of the scanning strategy, and under Scanning Electron Microscope (SEM), to have a more detailed look into the microstructure. The samples are observed in two views: a top view (XY plane of the building platform), and a side view, perpendicular to the building platform (YZ plane). Both are schematized in Figure 6.5. Notice that the samples were built using a zig-zag scanning strategy, with rotation of the scan orientation by 90 ° for each successive layer.

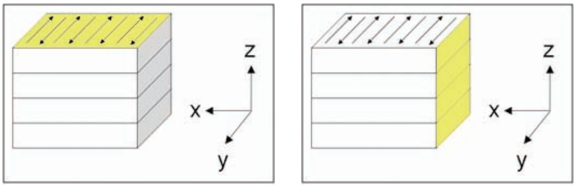

Figure 6.5: A schematic indication of both microscopic views: XY plane (left) and YZ plane (right). The Z-axis indicates the building direction in the SLM machine.

Light Optical Microscopy After etching, the footprint of the SLM process is revealed under the form of melt pool borders. Figure 6.6 shows the XY cross section of a maraging steel part produced with a scan speed of 200 mm/s and a laser power of 105 W. The semi-circular shapes show the melt pool borders, indicating the movement of the laser. As the melt pool is pushed backwards, the direction of the scan vectors can be revealed, as indicated by the white arrows in Figure 6.6.

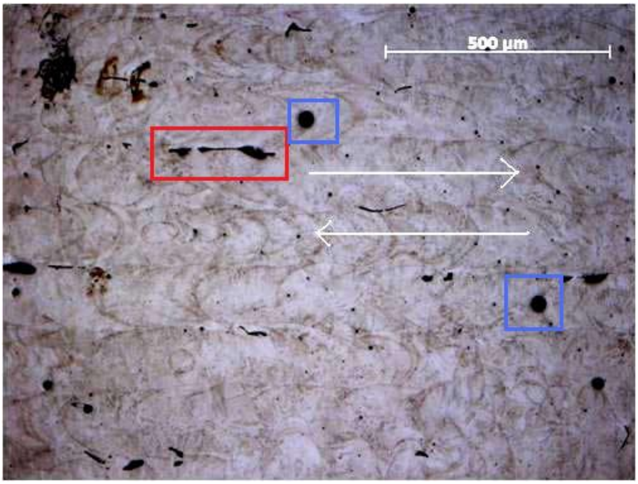

Figure 6.6: Macrograph of the XY cross section (top view) of a part produced with a scan speed of 200 mm/s and a laser power of 105 W. The red box indicates a pore due to insufficient overlap. The blue box indicates a pore due to evaporation or gas formation.

The black spots in the image indicate porosity that was formed during processing. Similar to the pores that were observed in the processing of aluminum alloys, two types can be distinguished: (i) The pores due to evaporation and gas, which are spherical in shape, and indicated in blue in Figure 6.6 and (ii) Pores due to insufficient overlap of neighbouring scan tracks, which are irregular in shape and are marked in red in Figure 6.6.

Figure 6.7 shows a macrograph of the YZ cross section of the same part. The melt pool borders are also distinguished in this side view. It can be seen that the scanning direction was rotated over 90° between alternating layers. Also the remaining porosity is detected in this image.

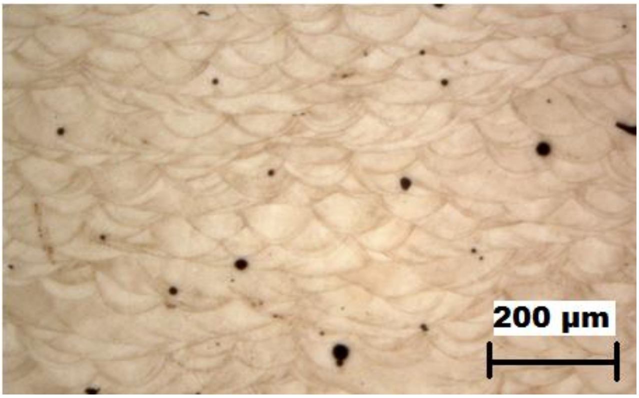

Figure 6.7: Macrograph of the YZ cross section (side view) of a part produced with a scan speed of 200 mm/s and a laser power of 105 W.

The influence of an increase in scan speed can also be seen upon observation of the macrostructure. Figure 6.8 shows the macrograph in the YZ plane of two parts produced with identical parameters, but different scan speeds. For a scan speed of 120 mm/s, the melt pool is stable and a dense part can be produced. For a scan speed of 280 mm/s, the melt pool becomes narrow and unstable. Porosity is formed throughout the enitire part.

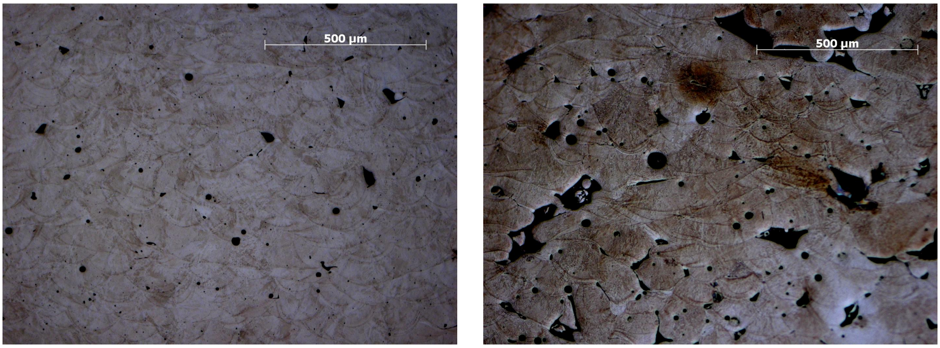

Figure 6.8: Macrostructure of parts produced with P = 105 W, t = 60 μm and v = 120 mm/s (left), v = 280 mm/s (right).

Scanning Electron Microscopy The top and side cross-sections observed by SEM are depicted in Figure 6.9. The micrograph on the left shows bi-directional

scan tracks while the one in the center depicts the cellular/dendritic solidification morphology and epitaxial growth of the grains on a section perpendicular to the layer build sequence.
In SLM, the cooling rate is very high and rapid solidification prevents formation of lath martensite. The intercellular spacing is less than 1 μm for the cellular structure and this contributes to the excellent strength and hardness. These statements are also validated by other researchers working on direct metal laser sintering of maraging steel 300 processed on an EOS machine [146].
In Figure 6.9 in the middle picture, one can observe a large inclusion with a size of about 10-20 μm, visible as a dark spot in the cross-section. The EDX analysis carried out on this inclusion confirmed that this was a titanium and aluminum combined oxide (Al_2TiO_5). Also other oxides containing a combination of Ti, Mo, Al and Si in other ratios were present in the sample. A more in depth study of these impurities was reported by Thijs et al [151].

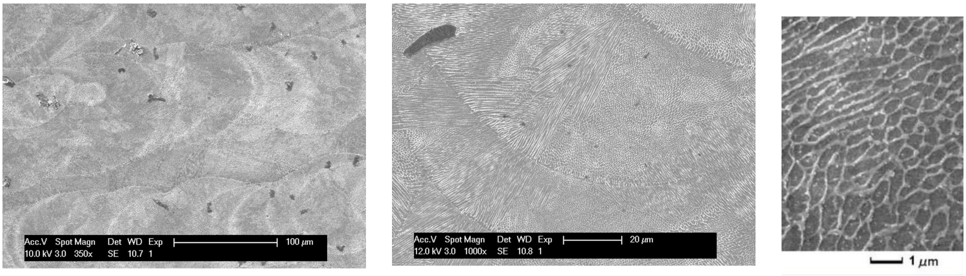

Figure 6.9: SEM pictures of the XY view (left) and XZ view (middle) of a sample produced with a scan speed of 120 mm/s and a layer thickness of 60 μm. Right: Formation of a fine dendritic structure due to rapid solidification. A complex oxide can be observed as a dark spot in the middle picture.

6.5 Mechanical properties

This section describes the effect of the process parameters on hardness, both on micro and macro scale.
Tensile and charpy test results are discussed later in section 6.6, where tensile properties and impact toughness are compared for parts with and without heat treatment.

6.5.1 Macro-hardness

Macro-hardness was measured on samples produced on a Concept Laser M3 machine, with different scan speed and layer thickness. For all parts, a laser power of 100W was employed, and a scan spacing of 126 μm. the scan speed ranged from 100 to 600 mm /s, while the layer thickness was varied between 30 and 60 μm in steps of 10 μm. The Rockwell A hardness measurement is chosen, as Rockwell C hardness measurements result in a very deep penetration into the material, where the indentor holder touches the measurement sample, making the measurement unreliable. Rockwell A hardness measurements use the same diamond cone indentor, but only employ a load of 60 kg, instead of 150 kg in Rockwell C.

The results of all Rockwell A macro-hardness measurements are depicted in Figure 6.10. The macro-hardness decreases for increasing scan speed, and for increasing layer thickness. The results show the same trend like observed in density graphs by Yasa et al.[186] and Badrossamay et al. [13]. The macro-hardness is mostly affected by the density. At low scan speeds, where the obtained densities don't differ much, there is a slight change in the measured macro-hardness. As the scan speed increases, the hardness values significantly decrease due to more porosity. To clarify the direct link between density and macro-hardness, the density graph by Yasa et al. is given in Figure 6.11.

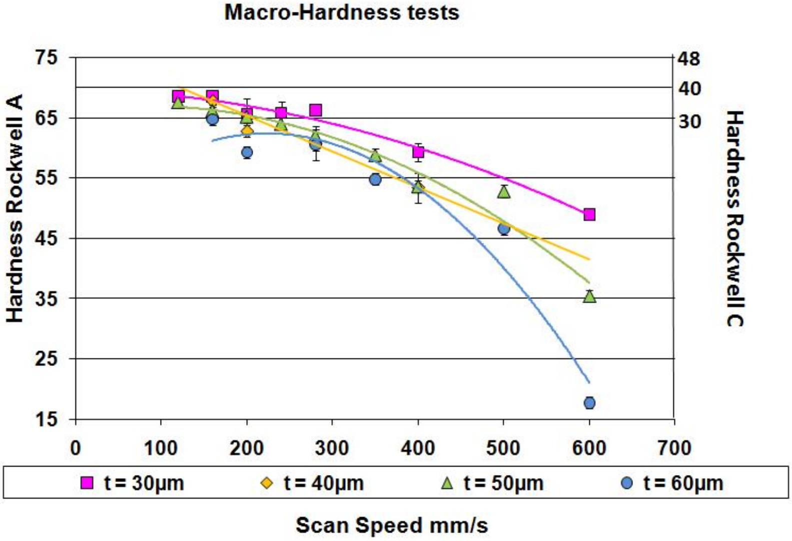

Figure 6.10: Rockwell A macro-hardness measurements for maraging steel parts produced with laser power P = 100W, scan spacing h = 126 μm and varying scan speed and layer thickness.

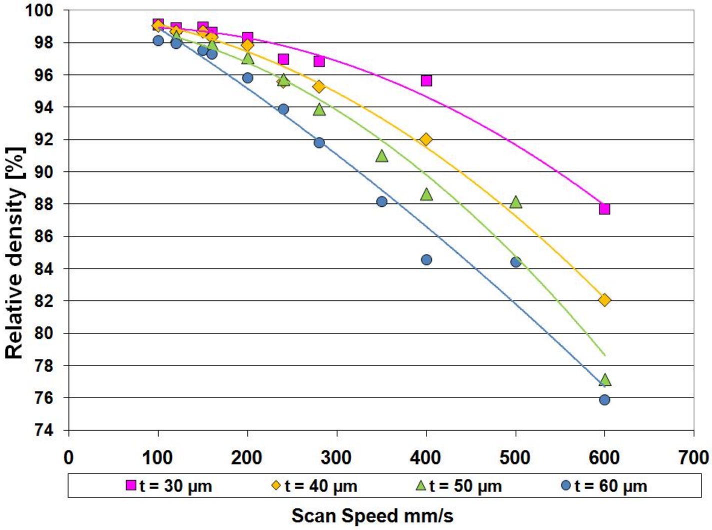

Figure 6.11: Relative density for maraging steel parts produced with laser power P = 100W, scan spacing h = 126 μm and varying scan speed and layer thickness, as reported by Yasa et al. [186].

6.5.2 Micro-hardness

Micro-hardness measurements are conducted on a Vickers hardness measurement device with a load of 0.5 kg and a pyramidal indenter. Each sample was measured in eight different places. The results depicted in Figure 6.12 indicate a 95 % confidence interval of these measurements. At high scan speeds, there is too much porosity to correctly perform any micro-hardness measurements. At lower scan speeds, the change of the scan speed or layer thickness does not significantly influence the material's hardness.

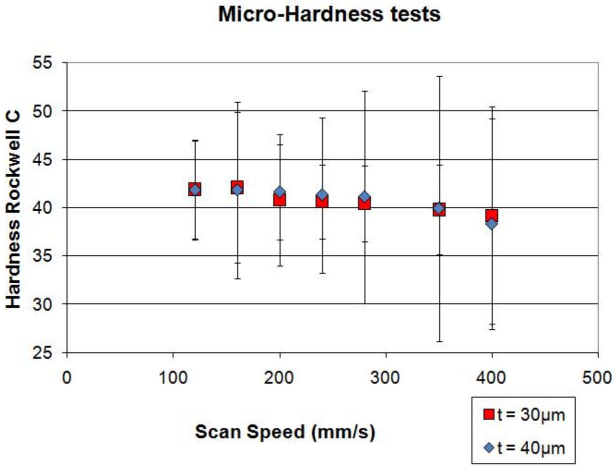

Figure 6.12: Rockwell A micro-hardness measurements for maraging steel parts produced with laser power P = 100W, scan spacing h = 126 μm and varying scan speed and layer thickness.

Laser remelting Besides the increase in density, also an increase in micro-hardness is observed by applying laser remelting after every scanning step. Table 6.3 shows that the material's hardness improves from 395.8 HV up to 412.6 HV and 414.0 HV for the first and second remelting strategy respectively. In conventionally produced bulk maraging steel 18Ni300, the material reaches hardness values of 280 to 300 HV without aging treatment [27, 125, 146]. The micro-hardness of the as-built SLM parts reaches a hardness of nearly 400 HV, which is about 30 % higher. This phenomenon is referred to as natural aging, taking place during processing by SLM. Due to the high temperatures and high cooling rates a very fine microstructure is formed, contributing to the high hardness.

Upon laser remelting, the material is heated up again and a second natural aging takes place, increasing the micro-hardness even further up to 414 HV.

Campanelli et al. [27] also investigated the influence of process parameters on hardness in SLM of maraging steel, however only on a limited range for scan speed, and only on a macro scale. The results of that study are consistent with this work: the macro-hardness of 18Ni300 maraging steel decreases with increasing scan speed due to the decrease in density.

6.6 Post-processing

6.6.1 Conventional heat treatment

The superior properties of the maraging steels, i.e. good strength and toughness, are achieved by the age hardening of a ductile, low-carbon body-centered cubic (bcc) martensite structure with relatively good strength. Therefore, the aging heat treatment is standard for maraging steels. It is aimed to form a uniform distribution of fine nickel-rich inter metallic precipitates during the aging of the martensite. These precipitates serve to strengthen the martensitic matrix. A detrimental side effect is the reverse transformation of metastable martensite into austenite and ferrite [8]. However, the kinetics of the precipitation reactions of iron-nickel maraging steels are such that a significant age hardening of about 20 HRC points already occurs before the start of this reverse transformation.
The aging heat treatment for maraging steels can be performed for different durations at various temperatures providing that the temperature is lower than the austenite start temperature. For maraging steel 300, the values recommended by the ASM Handbook are 3 to 8 hours at a temperature between 460 and 510°C [8]. In this study, a duration between 1-8 hours and a maximum temperature between 460°C and 500°C are tested.

6.6.2 Optimized heat treatment

The micro-hardness of the samples was measured and plotted in Figure 6.13. When the maximum aging temperature is 460°C, the hardness shows a linear relationship with aging time. When one keeps the part longer at this temperature, the hardness continues to increase without any sign of overaging. However for other temperatures tested in the scope of this study, at prolonged durations, the hardness starts to drop slightly. This is an indication of overaging meaning that the reversion of metastable martensite and coarsening of the inter metallic precipitates takes place. These two phenomena together decrease the hardness as the part is kept at elevated temperatures for a prolonged time.

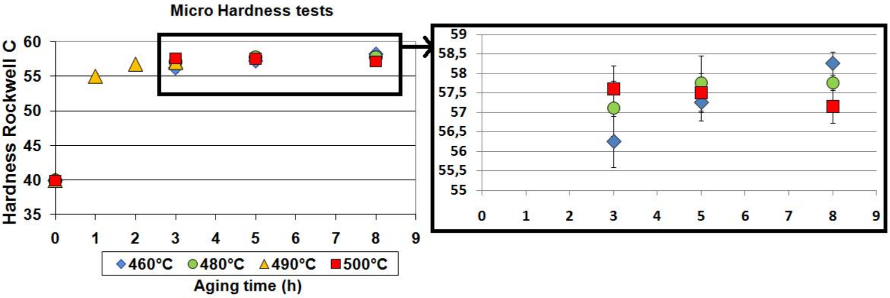

Figure 6.13: Micro-hardness for samples with identical process parameters and different aging parameters

Optimal heat treatment in terms of hardness and aging time is selected as aging 5 hours at 480°C. After this heat treatment a hardness of 58 HRC is achieved, which means an increase of 18 HRC compared to the as-built part using laser remelting. Higher hardness can be achieved for lower aging temperatures, but the increase in hardness is not significant in terms of the additional aging time.

In order to determine the volumetric percentage of austenite (fcc, face cubic centered) and martensite (bcc, body cubic centered), that are present before and after aging, XRD measurements were performed. The results are shown in Figure 6.14. The applied heat treatment causes an increase of the austenite phase. The austenite reversion is inevitable for long aging times, because the martensite is metastable and transforms to the stable austenite. The release of Ni into the Fe matrix which accompanies the transformation from $Ni_3(Mo,Ti)$ to the more stable Fe_2Mo precipitates promotes the austenite reversion [124].

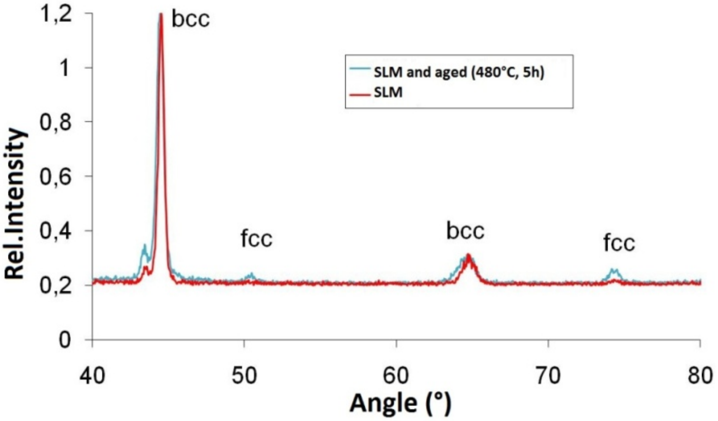

Figure 6.14: Results of XRD measurement before (red) and after (blue) applying heat treatment of 5h at 480°C.

As-built parts are not fully martensitic: also an austenitic phase is present (about 5.8%). The aging causes an increase of the austenite phase to about 9.4%, indicating that austenite reversion has taken place. Since the presence of austenite was found under all aging conditions (not only overaged samples), it may be assumed that reversion is taking place before the re-dissolution of the $Ni_3(Ti, Mo)$ precipitates. In SLM maraging steel parts, Ni-rich zones (caused by the segregation that is coupled with the cellular-dendritic growth) make an early austenite reversion possible [141]. These Ni-rich zones were detected by APT (Atom probe Tomography) [67].
Although some austenite is already present, the hardness could still be increased over the hardness values normally found for wrought maraging steel.

6.6.3 Tensile testing

Inclusions deteriorate the mechanical properties of the maraging steel, especially in the aged conditions where this steel grade is more brittle than in the as-built condition. Therefore, the specimens for mechanical testing were produced in order to obtain maximum density. Every layer was remelted according to the island scanning strategy with the same SLM parameters.

The mechanical properties that result from the tensile tests are given in Table 6.4, for as-produced and age hardened test specimens. For comparison, Table 6.4 also summarizes these properties for wrought maraging steel 300 [9, 90]. The values show the mean value for 4 specimens with 95% confidence intervals. The aging treatment for SLM specimens not only causes and increase in hardness, but also severely effects the fracture behavior. The presence of oxides in the SLM parts can become detrimental after aging. These oxides are not expected in wrought parts and thus the fracture behavior does not differ much in wrought parts after aging.

x ± s	E	$R_{p0.2}$	UTS	ϵ_{break}	HRC
	GPa	MPa	MPa	%	
SLM-produced	163 ± 4.5	1214 ± 99	1290 ± 114	13.3 ± 1.9	39.9 ± 0.1
SLM + aging	189 ± 2.9	1998 ± 32	2217 ± 73	1.6 ± 0.26	58 ± 0.1
Wrought	180	760-895	1000-1170	6-15	35
Wrought + aging	190	1910-2020	1951-2041	11	54

Table 6.4: Mechanical properties of maraging steel 300, SLM-produced and wrought

with:
E = Young's modulus
$R_{p0.2}$ = 0.2% proof stress
ϵ_{break} = Elongation at break
HRC = Hardness Rockwell C

Aging for 5 hours at $480°C$ leads to an increase in hardness and strength through the precipitation of $Ni_3(Mo,Ti)$ and Fe_2Mo intermetallics. The presence of these precipitates is measured by APT [67]. The ultimate tensile strength increases from 1290 MPa to 2216 MPa, which is an increase of 72%. The Rockwell C hardness increases with 45% to reach a value of 58 HRC, however the elongation was reduced from 13% to 1.6% by age hardening the maraging steel. The presence of these precipitates embrittles the material.
Tensile tests also show an increase in Young's modulus to 189 GPa after applying the heat treatment. The formation of the $Ni_3(Mo,Ti)$ precipitates lower the share of Nickel in the martensite matrix, leading to an increase in Young's modulus, which is consistent with the study presented in [54].

A comparison of the mechanical properties of the SLM-specimens and wrought maraging steel, indicates the very fine cellular microstructure resulting from the SLM process, leading to higher hardness and strength. In SLM with laser remelting after each layer, this phenomenon is more pronounced due to the larger heat sink when melting solidified material instead of powder material.

The embrittlement that is caused by the heat treatment is also shown in the fractography. The specimen without heat treatment broke after substantial plastic deformation. Typical for a ductile fracture is the formation of dimples (left in Figure 6.15). In the part of the test specimen that undergoes a large deformation, micro-cavities arise where there are imperfections. These cavities cause large stresses which lead to more micro-cavities. Eventually these cavities conjoin and the tear grows fast. A ductile fracture is always trans-granular [88]. For the age hardened specimen, the fracture is very brittle. There was hardly any plastic deformation before rupture. Both trans-granular and inter-granular fractures appear as shown in the right picture in Figure 6.15. The precipitates in the age hardened samples act as imperfections and initiate micro-cavities.

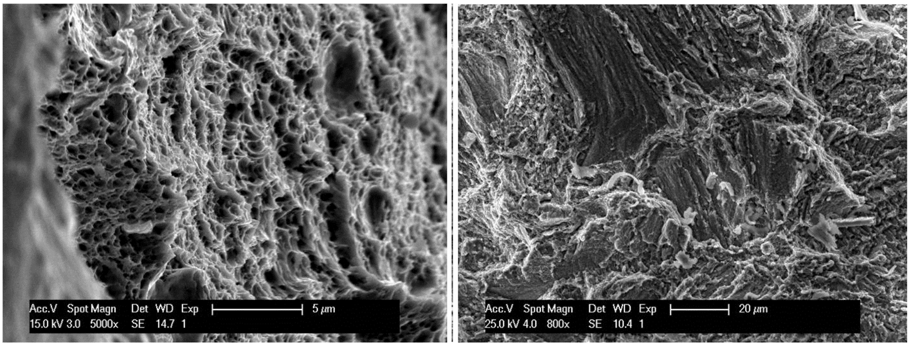

Figure 6.15: Formation of dimples at ductile fracture for as-produced specimens (left). Inter- and trans-granular fracture for brittle age hardened specimen (right).

6.6.4 Charpy impact testing

The Charpy impact test is a common method used to determine material toughness by hitting a test specimen with a hammer, mounted at the end of a pendulum. The specimen is broken by a single blow from the pendulum that strikes the middle of the specimen on the un-notched side. A V-shaped notch is generally used in the impact specimen in order to control the fracture process by concentrating stress in the area of minimum cross-section. In this study, Charpy tests are done according to ASTM E23 standard [10]. The size of the standard specimen is 10 x 10 x 55 mm with a notch as defined in the same standard.

After the parts were produced by SLM, they were sand-blasted in order to remove the loosely sticking powder to the specimens' walls. Some of the samples were then heat treated while some were kept as-built for a comparison. The impact energies are plotted in Figure 6.16.

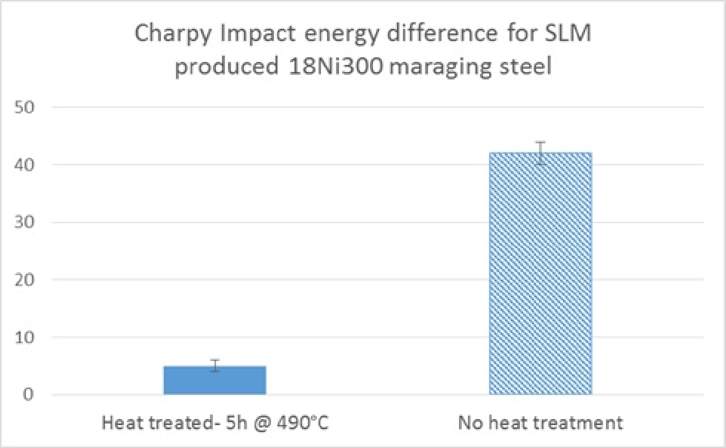

Figure 6.16: Results for Charpy impact tests on maraging steel 300.

Charpy tests show a significant decrease in toughness when an aging heat treatment is applied. The reduction in the toughness depends on the aging conditions. These conditions lead to higher hardness and result in lower toughness. The intermetallic precipitates promote the brittle fracture, so less energy will be needed to cause a complete rupture for a higher hardness. The comparison of the fracture surfaces shown in Figure 6.17 also indicates the brittleness of the heat treated specimens.

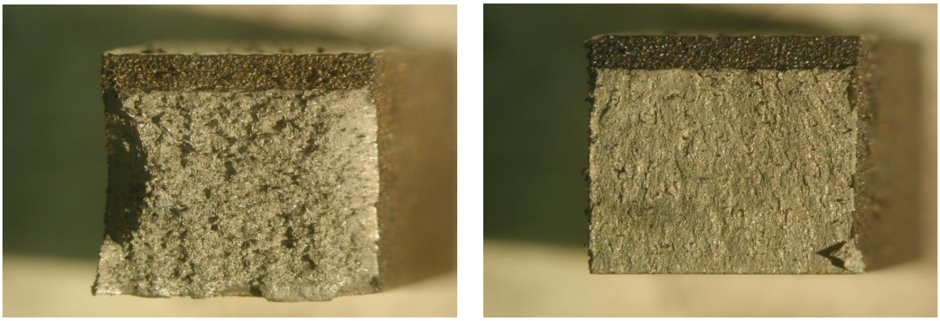

Figure 6.17: Fracture surfaces of Charpy samples: as-built (left) and after heat treatment (right).

When compared to conventionally produced maraging steel 300, SLM processed specimens show a reduced toughness (30-40%) in the heat treated condition. As explained before, this may be due to the formation of Ti-Al combined oxides in the martensite matrix which deteriorate the mechanical properties significantly in the heat-treated condition when the material is much more brittle.

6.7 Conclusions

1. Higher layer thickness and/or scan speed causes a decrease in density, which leads to a decrease in macro-hardness. On the other hand, there is no significant influence of layer thickness and scan speed on the micro-hardness of maraging steel 300 in the tested ranges.

2. Solidification takes place by cellular-dendritic growth mechanisms in SLM of maraging steel grade 300. Inter-cellular spacing is less than 1 μm which contributes to the excellent strength and hardness achieved in both as-produced and age hardened conditions. A similar microstructure was observed by Cabeza et al. /citeCabeza, in the laser surface melting of maraging steel grade 200.

3. Laser Remelting of every layer causes higher density and an additional natural aging, thereby further increasing the micro-hardness.

4. Age hardening the SLM-produced maraging steel for 5 hours at 480°C leads to a hardness of 58 HRC and an increase of ultimate tensile strength from 1290 MPa to 2216 MPa. Elongation was reduced from 13% to 2%.

The heat treatment causes an increase in Young's Modulus to 189 GPa due to the changes in the matrix for the formation of precipitates.

5. Comparison of the mechanical properties for wrought maraging steel and SLM-produced maraging steel shows the natural aging due to the SLM-process and due to remelting every layer. The ductility and toughness values obtained by SLM were found to be much lower than the ones obtained by conventional techniques, as the SLM parts contain Al-Ti oxides which affect the ductility and toughness. Similar work on SLM of 18Ni300 maraging steel [28] showed similar results: mechanical properties comparable to conventionally produced maraging steel, two types of pores (irregular and circular shaped) and a cellular dendritic morphology in the microstructure.

Chapter 7

M2 High Speed Steel

In section 7.1, the material properties of the M2 High Speed steel are summarized, and the role of the alloying elements is explained. In section 7.2, the challenges that come with the production of this material by SLM are declared. Section 7.3 briefly describes the powder material that was used in all experiments, while section 7.4 shows the influence of scan speed on the formation of single track scans.
In section 7.5, the origin of the cracks is explained and a pre-heating module is built. Using baseplate pre-heating, cracks can be prevented. Afterwards, the scan parameters are optimized to obtain maximal density. Later the effect of pre-heating and laser remelting on density and surface quality is shown. Section 7.6 describes the mechanical properties of the SLM-produced material, how it differs from conventionally produced M2, and how the properties are related to the scan parameters. Hardness and tensile tests are performed and results are correlated to the formed microstructure in section 7.7. The final section 7.8 summarizes the main conclusions of this chapter.

7.1 Material Properties

M2 High Speed Steel, also designated as AISI M2, is a molybdenum high speed grade tool steel. The chemical composition in wt%, according to AISI (American Iron and Steel Institute) of this alloy is given in Table 7.1.

The main characteristic of M2 HSS is its high hardness up to 65 HRC, depending on the heat treatment process [136]. This high hardness results from the high

Fe	C	Mn	Si	Cr	V	Mo	W
Bal.	0.8 - 1.05	0.15 - 0.4	0.2 - 0.45	3.8 - 4.5	1.8 - 2.2	4.5 - 5.5	5.5 - 6.8

Table 7.1: Chemical composition of M2 High Speed Steel in wt%, according to AISI [4]

carbon content, where M_xC_y type carbides are formed, M representing one or more alloying elements: Mo, W, V and Cr [193]. Besides the high amount of carbon, the M2 High Speed Steel is also characterized by the high percentage of alloying elements. Tungsten and vanadium are not only added to form carbides, but also increase the high temperature resistance. Chromium Cr on the other hand supports the required heat treatment, allowing core hardening.

	Conventionally Cast	**Cast + HT**
Young's modulus E [GPa]	190 - 210	190 - 210
Ultimate Tensile Strength UTS [MPa]	790	1550
Elongation at break ϵ [%]	16.5	1.5
Hardness Rockwell C [HRC]	18	65
Density ρ $[g/cm^3]$	8.16	
Solidification Range $[°C]$	1246 - 1437	
Thermal conductivity λ_{therm} [W/mK]	28.9	
Thermal expansion coefficient α_L $[10^{-6}/K]$	12.2	

Table 7.2: Mechanical and physical properties of conventionally cast M2 HSS parts, with and without heat treatment (HT) [9].

7.2 Challenges

The research for the production of M2 High Speed Steel by SLM is driven by the demand for a possibility to produce complex shaped cutting or forging tools, and casting dies with conformal cooling channels. This group of tool steels is the best fit for these applications, as the material can withstand high pressure, heat and wear. M2 HSS can reach a hardness up to 65 HRC, and maintain these values at elevated temperatures.

The high carbon content of this alloy ensures the formation of carbides, resulting in a very high hardness upon quenching after tempering and austenitizing. This high hardness however, goes hand in hand with a low toughness.

Moreover, due to high amounts of carbon being trapped within the BCC crystalline structure during rapid solidification, high internal stresses occur [156]. In welding, pre-heating is typically applied for high carbon steels (> 0.6 % C) to reduce the tendencies of thermal shocks and residual stresses [42, 65]. Chromium hot work steels, like for example H13, form less carbides and thus have a lower hardness and much higher toughness. Moreover, this H13 alloy has a smaller solidification range. The combination of both aspects lowers the tendency to form cracks during SLM.

Literature has revealed the possibility to process the M2 tool steel by laser based processes, and the effect of pre-heating on residual stresses. The work of Childs et al. showed that the formation of a stable, crack-free single line track is possible in M2 tool steel, and a process window is defined for low scan speeds and low laser power [31]. Niu et.al. [120] showed the influence of scanning parameters on the density of M2 HSS two-dimensional surfaces. Since no three-dimensional parts were built in that work, no cracks were formed.

In Abe et.al., a dual laser scanning system in which YAG and CO2 laser beams are offset a small amount from each other is proposed. It is considered that slow cooling or re-heating after melting can eliminate residual stress and improve the part's ductility [2]. The use of a pre-heating system to reduce thermal stresses has also shown its advantages in the work of Alimardani et al. [3], where the residual stresses were reduced by 22 % in a stainless steel wall produced by direct metal deposition, by using a pre-heating up to 800 K. Das et al. at the University of Texas developed a powder bed pre-heating system that reaches up to 1300°C [40]. Initial tests at pre-heating temperatures of 350°C and 900°C showed that the influence of pre-heating on the wetting behavior is minimal [39]. In SLM of ceramics, Hagedorn et al. established crack-free parts with a CO2 laser pre-heating of 1700°C [59].

Numerical models for residual stresses are developed by Shiomi et.al. [143], Zaeh et al. [188] and Mercelis et al. [106], while Casavola et al. [30, 29] showed the effect of part thickness on residual stress in maraging steel. It is however in measuring and eliminating these stresses that the major shortcomings lie.

7.3 Powder material

Gas atomized M2 HSS powder produced by LPW [97] was used. The SEM image in Figure 7.1 shows the spherical powder particles with some small satellite particles on the larger fraction. The size of the powder particles ranges from 15 to 45 μm in diameter (based on the sieving method).

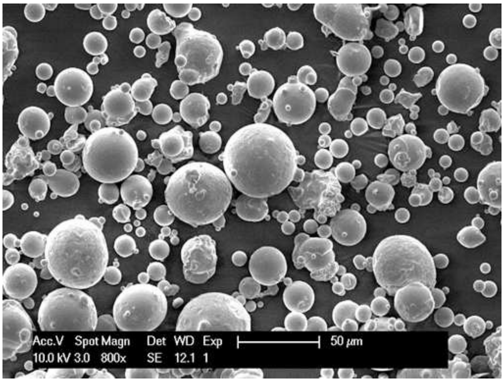

Figure 7.1: SEM image of M2 HSS powder.

7.4 Single track scans

As observed in chapter 4 on A360 aluminum alloy, single track scans can provide a preliminary process window, indicating for which scan parameters a stable melt pool was formed.

For M2 HSS, single track scans were produced on a Concept Laser M3 machine, employing a laser power of 100 W, a layer thickness of 30 μm and scan speeds varying from 50 to 700 mm/s. For every scan track, the top view was observed under SEM to check for discontinuities. Afterwards, the samples were cut in the direction of the YZ plane, in four different places. Every cross section is observed by SEM and the scan track's depth and width (definition see Chapter

4, Figure 4.5) are measured based on a pixelcount method. The results of these measurements are depicted in Figure 7.2 and Figure 7.3, with a confidence interval of 95 % on 4 measurements.

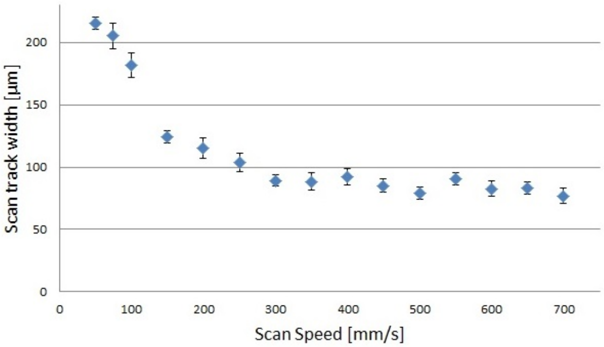

Figure 7.2: The width of single track scans, produced with a laser power of 100 W, layer thickness of 30 μm and scan speed varying from 50 to 700 mm/s.

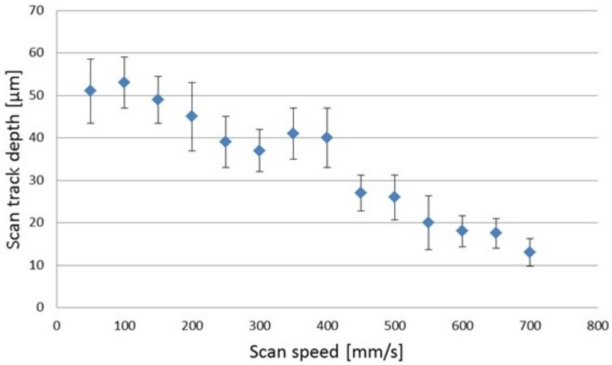

Figure 7.3: The depth of single track scans, produced with a laser power of 100 W, layer thickness of 30 μm and scan speed varying from 50 to 700 mm/s.

Similar to the single track scans in A360 aluminum alloy, the melt pool depth decreases with increasing scan speed. The reduced interaction time of the laser and the powder bed at high scan speeds results in less track penetration and balling phenomena.

The melt pool width also decreases for increasing scan speed. The more heat being transferred to the powder bed, the more particles will melt and the bigger the melt pool will be.

Some cross sectional SEM images are depicted in Figure 7.4, showing the effect of increased scan speed on the formation of the melt pool. In all cross sections a white Heat Affected Zone can be distinguished beneath the melt pool. For scan speeds above 550 mm/s, the balling effect starts to occur.

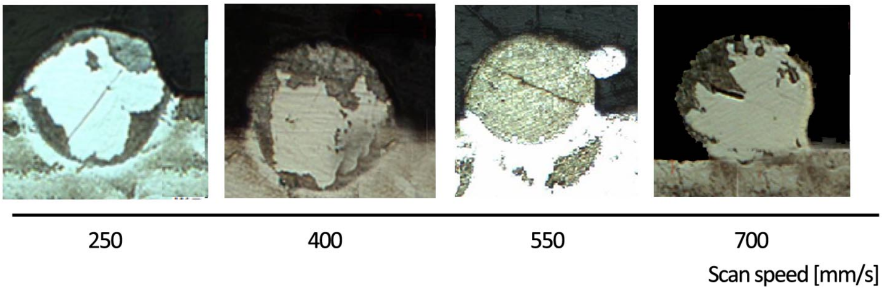

Figure 7.4: SEM images indicating the effect of increased scan speed on the formation of the melt pool in M2 HSS.

7.5 Parameter Optimization

7.5.1 Cracks, Warpage and Delamination

A laser power of 100 W was used in combination with different scan speeds, ranging from 150 to 700 mm/s, to produce preliminary three-dimensional 15 mm x 15 mm x 10 mm blocks. All parts were produced using the island scanning strategy, with 90 ° rotation between alternating layers, as this was shown to be the scanning strategy resulting in the least residual stresses [106, 131]. Some problems occurred in the form of warpage, cracks and delamination from the baseplate. The degree of warpage and cracks is more pronounced for parts fabricated with low scan speed. Figure 7.5 shows the produced parts and the difficulties that occurred.

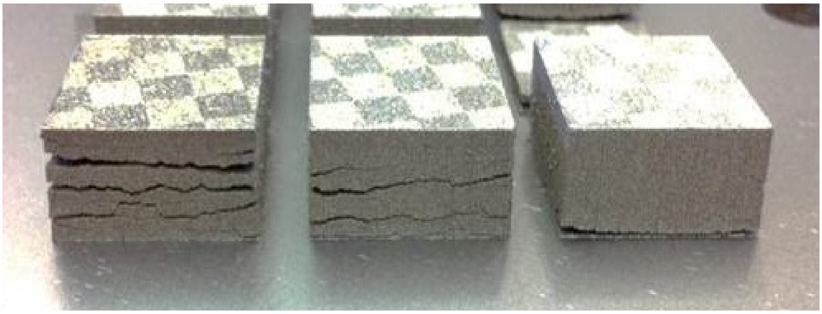

Figure 7.5: Preliminary M2 HSS parts produced by SLM, showing cracks, warpage and delamination from the baseplate.

When producing M2 HSS parts by Selective Laser Melting, high thermal stresses cause the parts to crack or delaminate from the baseplate. These thermal stresses need to be reduced in order to eliminate this cracking and to produce dense and qualitative parts in M2 HSS by SLM.
In SLM there are two mechanisms that may induce residual thermal stresses: (i) induced stresses in the solid substrate just underneath the present layer being melted and (ii) stresses due to the cool-down phase of the melted top layers.

The first phenomenon results from large thermal gradients in the solid material just underneath the laser spot (Figure 7.6). Due to the high temperature in the upper layers of the solid substrate, those upper layers will expand, while the colder underlying solidified layers will restrict this expansion. This induces compressive stresses σ_{comp} in the upper layers of the substrate that may rise above the yield strength of the material and cause plastic upsetting in those upper layers. When the yield strength is reached, the compressive stresses in the material cause plastic deformation ϵ_{pl} of the upper layers. When those plastically deformed layers cool down, their compressive state is converted into residual tensile stresses σ_{tens}. Those residual stresses may induce cracking of the part.

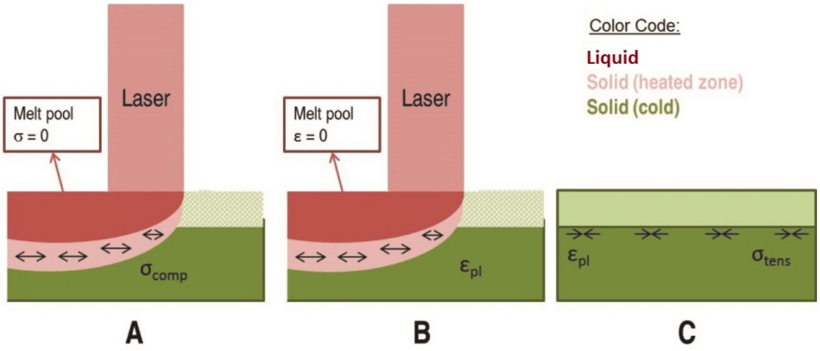

Figure 7.6: The formation of residual stresses due to thermal expansion of underlying layers.

In the second phenomenon, the melted top layers tend to shrink due to thermal contraction. This deformation is again prohibited by the underlying layers, thus introducing tensile stresses in the top layer, and compressive stresses below.

From previous work on reduction of thermal stresses by Mercelis et al. [106] and Shiomi et al. [143], it is shown that so far, the best way to reduce thermal stresses is uniform pre-heating of the baseplate. Also, this PhD report will show that there are more stresses built up in a part with higher density. Pores relax the residual stresses as they do not contain internal stresses.
With laser welding references in mind, a baseplate pre-heating system is developed to lower thermal gradients in SLM, with the aim to produce crack-free high density parts in M2 HSS.

7.5.2 Pre-heating

Figure 7.7 shows the schematic overview of the heating module that was designed and installed on the Concept Laser M3 machine [77]. The heating element itself (red) is installed underneath the building platform, on top of which the baseplate is mounted. The heating element is surrounded by insulation material so the rest of the building module does not heat up: it is critical that both the mechanical set-up (e.g. the building plane determines the layer thickness) and the optical set-up (determination of the laser path and focus) do not expand or damage due to excessive heat.

The temperature of the baseplate can be controlled by the resistive heat element. A proportional and integral control loop (PI-controller) controls the power to the heat element to achieve a desired temperature on the baseplate within a range of ± $2°C$, up to $200°C$. This pre-heating module can easily be disassembled.

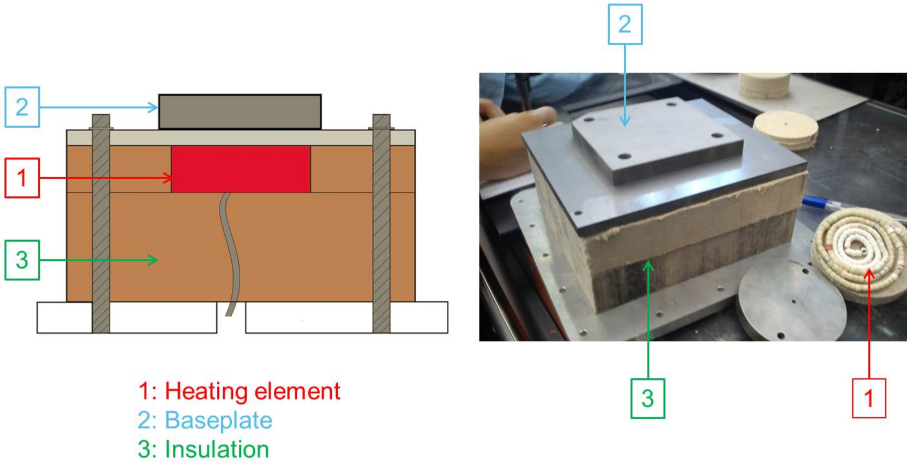

Figure 7.7: Left: Schematic overview of the pre-heating module. Right: Realization of the pre-heating module

In order to build crack-free parts with high density, pre-heating of the baseplate was applied to lower the thermal gradient during the process. Figure 7.8 shows 3 samples which were built using three different pre-heating temperatures ($90°C$ (left), $150°C$ (middle) and $200°C$ (right)). It can be seen that the higher pre-heating temperature results in less crack formation. All parts in Figure 7.8 were produced to have a density of 99.3 %, hereby eliminating the influence of density on stress relaxation and crack formation. When observing the cross-section of the crack-free part under LOM and SEM, it is shown that the part does not contain micro-cracks either.

Figure 7.8: M2 HSS parts produced with a pre-heating temperature of 90°C (left), 150°C (middle) and 200°C (right)

Secondly, crack formation is also influenced by the amount of porosity. Upon observation of three parts, produced with identical scan parameters (laser power 90 W, layer thickness 30 μm) but a different scan speed (250 , 400 and 550 mm/s), it can be seen that crack formation is more pronounced for parts with the lowest scan speed of 250 mm/s, which is also the part with the highest density.

In figure 7.9, these parts are shown, indicating the scan speed with which they were produced, the pre-heating temperature that was employed and the resulting part density. The lower the pre-heating temperature, the more pronounced the cracks are. The same can be concluded for the lower scan speed. It is however not directly the scan speed, but the resulting part density that influences the crack formation.

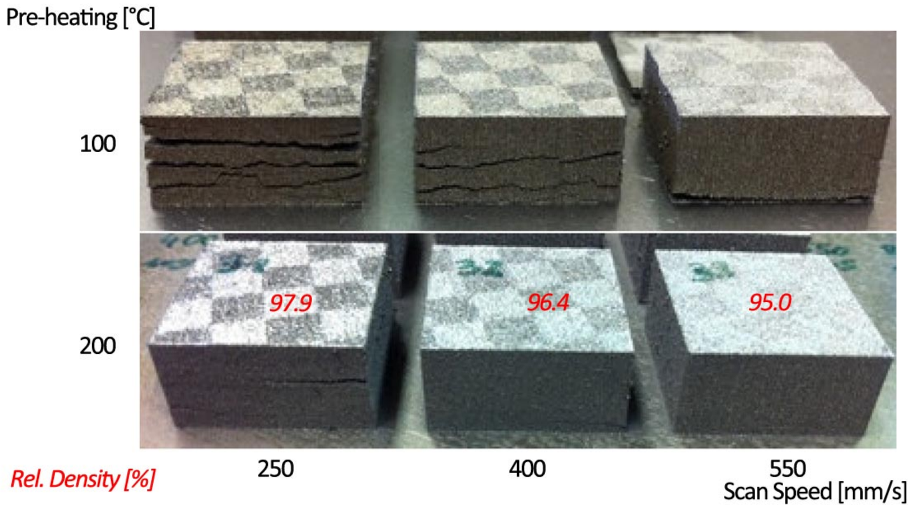

Figure 7.9: Crack formation is more pronounced for parts with high density and/or low pre-heating temperature. All parts were produced with a laser power of 90 W and a layer thickness of 30μm.

For further tests, all parts are produced with a pre-heating temperature of $200°C$ (on the baseplate) to avoid cracks, warpage and delamination from the baseplate.

7.5.3 Density optimization

Part density is one of the most important physical parameters to optimize. Not only because it has a direct influence on the part's mechanical and physical properties, but here it was also shown to have an influence on crack formation. The part density depends on many process parameters, while this research focuses on the effect of scan speed v, remelting and the pre-heating temperature T. The influence of these parameters on other properties like hardness and surface roughness will be discussed in the following subsections.

Numerous test parts were produced with a laser power of 105 W, scan speeds varying from 150 mm/s to 550 mm/s and pre-heating temperatures of $90°C$ and $200°C$. For some parts, every layer was remelted with a laser power of 105

W and scan speed of 200 mm/s before adding a new layer. Relative densities of these parts are depicted in Figure 7.10.

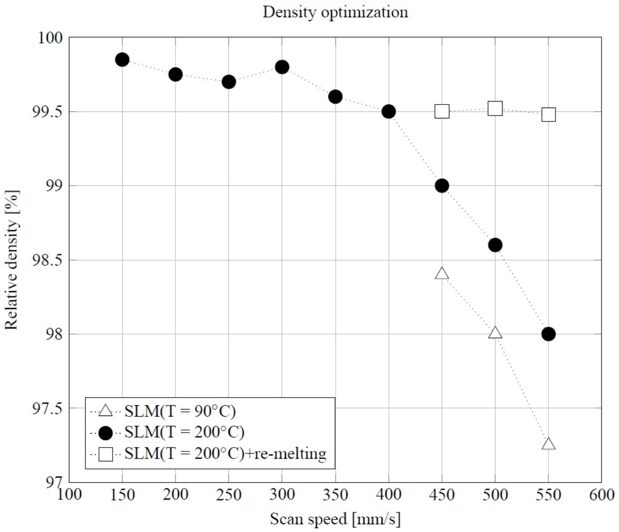

Figure 7.10: Density optimization of M2 HSS parts produced with and without remelting of every layer, at two different preheating temperatures.

Similar to density optimization for other materials in this thesis, the relative density decreases for increasing scan speed. The melt pool becomes too narrow, and eventually balling will occur, significantly lowering the part density. This was also shown in the work of Badrossamay et al. [12] on SLM of M2 HSS. Applying laser remelting in every layer can however increase the part density up to about 99.5%.

The pre-heating temperature T also influences the part density. When applying more pre-heating, less heat input is needed from the laser source to melt the powder. That is why, for higher pre-heating temperatures, higher scan speeds can be used to produce equally dense parts. Figure 7.10 shows that parts produced with a pre-heating of $90°C$ need a scan speed of 500 mm/s to result in 98.3% density. While parts produced with a pre-heating temperature of $200°C$ can be scanned with a scan speed of 550 mm/s to get the same density.

7.5.4 Surface roughness optimization

In this work, only top surface roughness is analyzed. The roughness on the side surface was not taken into consideration here, as it depends on many aspects like for instance the staircase effect [133] and layer thickness. The influence of scan speed on top surface roughness is negligible, within this applied range. To compare surface roughness for parts produced with and without remelting, for different pre-heating temperatures, several parts were produced with identical parameters, resulting in similar part density. As can be seen from the results in Figure 7.11, the best way to improve top surface quality is to apply laser remelting.

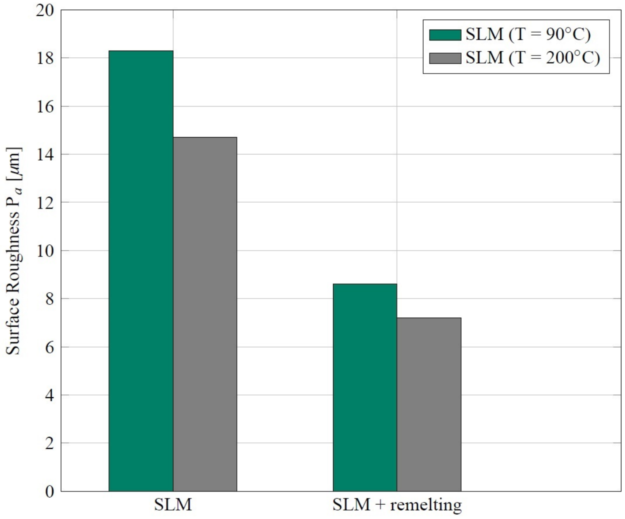

Figure 7.11: Influence of pre-heating temperature and remelting on top surface roughness.

By remelting the top layer, the surface roughness can be improved by 47% (from 18.3 μm P_a to 8.6 μm P_a). Both high pre-heating temperatures and remelting improve the top surface quality, because they both cause the formation of a stable melt pool. This is also shown in the SEM images(top) and surface roughness maps (bottom) of Figure 7.12. Note that remelting always increases the total production time, and a good trade-off must be made between productivity and part quality.

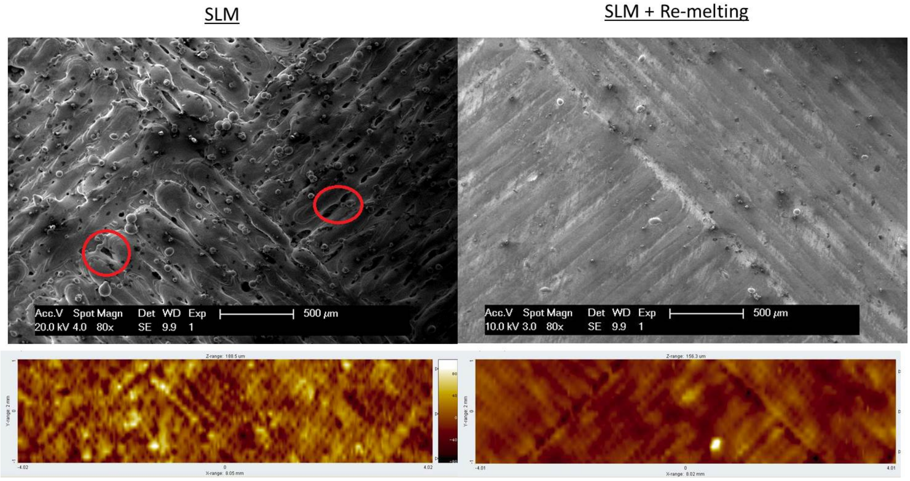

Figure 7.12: Top surface (SEM and roughness map) of parts produced with P = 105 W and v = 500 mm/s. left: no remelting, remaining porosity indicated by red circles. Right: laser remelting applied at 200 mm/s.

7.5.5 Remelting

Laser remelting has shown to improve part density and top surface quality. However, when remelting every layer of M2 parts, the formation of cracks becomes more likely due to:

1. The increase of density: remelting increases the density of the part, and thus enhances crack formation as stresses relax through pores.
2. The higher cooling rate: remelting every layer involves a higher cooling rate because solid material has a higher heat conductivity than powder material. Because of this higher cooling rate, more martensite phase will be formed, which is more brittle than austenite phase. While being submitted to the same stresses, the brittle martensite phase will crack more easily than the austenite phase. Figure 7.13 shows the difference of crack formation in parts that were produced with and without remelting every layer. Figure 7.14 indicates the increase in martensite formation for laser remelted parts.

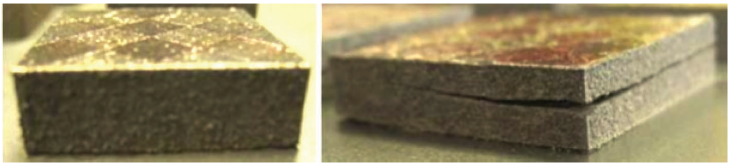

Figure 7.13: M2 HSS parts produced with P = 105 W, v = 250 mm/s and h = 128 μm. Left: only SLM. Right: SLM + remelting at 200 mm/s.

XRD measurements are performed both on the part without, and the part with laser remelting. For SLM parts without remelting, martensite and retained austenite were detected, in combination with some carbides. When laser - remelting is applied, most of the retained austenite transforms to martensite, and the presence of carbides is expected to slightly increase. In Holzweissig et al. [64], retained austenite was also detected in SLM-produced H13 tool steel, which is generally ferritic/martensitic.

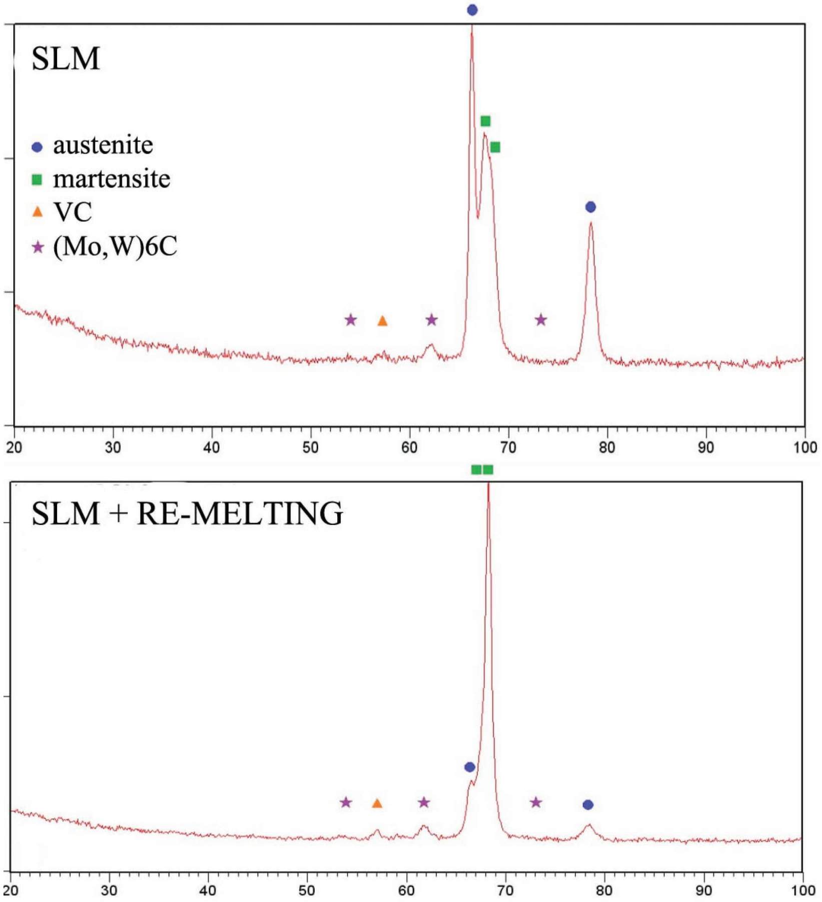

Figure 7.14: XRD measurements of M2 HSS parts produced with and without remelting of every layer. P = 105 W, v = 250 mm/s, h = 128 μm.

7.6 Mechanical properties

7.6.1 Hardness

For conventionally produced M2 HSS parts, the high hardness (of about 65 HRC) is reached by a post-process hardening heat treatment as defined by ASM

[9]. It includes an annealing step at 870 - 900°C followed by hardening for 2 to 5 hours at 1190 - 1230°C and quenching in oil or air.
Rapid cooling rates and high temperatures are typical for the SLM process. The rapid cooling results in rapid solidification of the melt pool and thus a very fine microstructure. Therefore, a relatively high hardness (57 HRC) is achieved for SLM produced M2 HSS parts, without need for a post-process thermal treatment. When every layer is remelted, the hardness of the final part even increases up to 64 HRC. The higher hardness of the remelted parts is due to the increase of martensite phase. More martensite is formed because the cooling rates are much higher for remelting (on solid material) than for first time melting (powder material), as shown in XRD measurements (Figure 7.14). All hardness results are depicted in Figure 7.15.

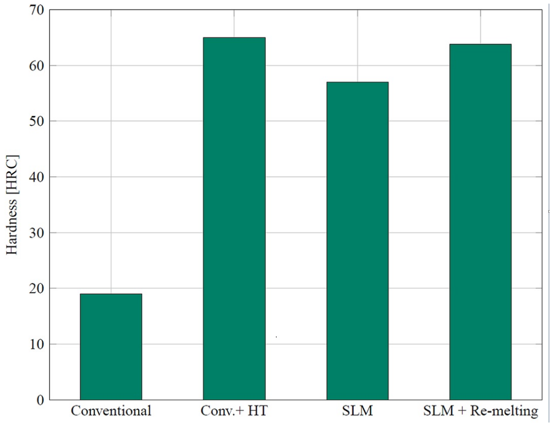

Figure 7.15: Hardness of M2 HSS SLM parts compared to conventionally cast parts.

7.6.2 Tensile Properties

Besides micro-hardness, also other mechanical properties were taken under investigation. Properties like tensile strength and ductility are compared for SLM-produced parts and conventionally produced parts. To reach the optimal mechanical properties (strength and hardness), conventional M2 HSS parts undergo a standardized heat treatment.
Tensile tests were performed on three types of tensile bars:

1. Conventionally cast M2 High Speed Steel, cut to the standardized dimensions by EDM.

2. Conventionally cast M2 HSS, cut to dimensions by EDM and furnace heat treated as defined by ASM [9]
3. SLM produced M2 High Speed Steel.

Of each type, five tensile bars were tested and the results in Figure 7.16 depict a 95% confidence interval.

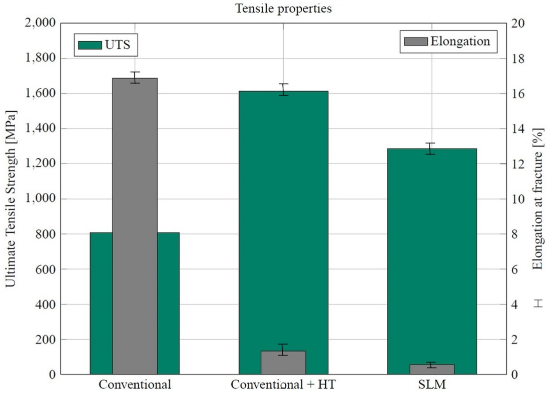

Figure 7.16: Ultimate tensile strength and elongation at fracture for three types of tensile bars.

As expected, the annealing + hardening treatment results in a more brittle, but stronger material. After heat treatment, the conventionally produced M2 High Speed Steel reaches and ultimate tensile strength of 1620 ± 283 MPa, compared to 804 ± 19 MPa without heat treatment.
In the austenitizing step of the heat treatment, the material is heated up close to the melting temperature, to ensure carbide dissolution. Afterwards, during quenching, a brittle martensite phase is formed, enriched with carbon. This causes the high increase in strength and the reduction of the elongation at fracture by a factor of 10.

In SLM produced parts, there is an inherent heat treatment that takes place during the process, because of the high temperatures that are reached and because of the high cooling rates. This causes the strong but brittle martensite phase to form during the SLM process, as indicated in the XRD measurements, leading to tensile test results that approach the values for conventionally produced and heat treated M2 High speed steel.

7.7 Microstructure

7.7.1 LOM

Upon etching with Vilella's reagent, the macrostructure of the M2 parts can be revealed. In Figure 7.17, the LOM images are depicted for the YZ-plane of three different parts, each with identical process parameters, but different scan speed: (from left to right) 250 mm/s, 550 mm/s and 700 mm/s.

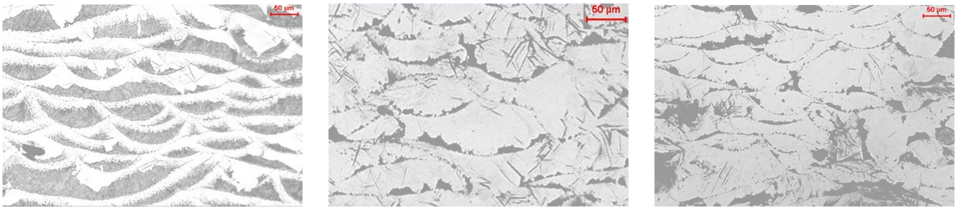

Figure 7.17: LOM images in the cross-sectional YZ-plane of M2 HSS parts produced with a laser power of 105W, and a scan speed of 250 mm/s (left), 550 mm/s (middle) and 700 mm/s (right).

A first observation of these macrographs indicates that there is an alternation between a dark and a bright phase. The elliptical shape of the melt pools can also be distinguished and the 90 ° rotation between successive layers is also shown. A similar macrostructure was observed by Simchi et al. [144] in SLS of M2 HSS, where a laser power of 200 W and a scan speed of 175 mm/s were conducted. The main difference is the larger melt pool size, due to the larger laser spot in SLS. The highest density that was achieved by Simchi et al. was close to 90 % with a laser power of 200 W and a scan speed of 50 mm/s [144]. The low scan speed of 250 mm/s shows a different microstructure compared to higher scan speeds of 550 mm/s and 700 mm/s. For higher scan speed, the macrostructure almost completely consist of the bright phase. The part produced with a scan speed of 250 mm/s is taken under further investigation, as it contains the most information and results in the highest density.

Figure 7.18 shows a higher magnification of the cross-section in the YZ-plane of the part produced with a scan speed of 250 mm/s. The image shows about one melt pool. At the bottom of the melt pool, the phase difference between bright and dark phase indicates the melt pool border. In the middle of the melt pool, a distinct phase transition is present between the dark and the bright phase, whereas on the top of the melt pool, this phase transition is more gradual. Upon observation of the cross section of the single track scans (Figure 7.4 it can be seen that the white elliptical border beneath the melt pool is a heat affected zone of about 8-10 μm thick.

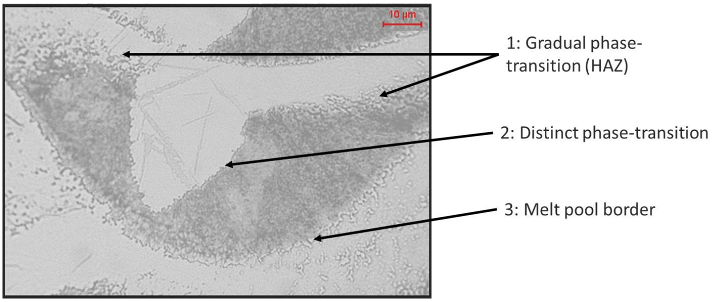

Figure 7.18: Higher magnification LOM image in the cross-sectional YZ-plane of M2 HSS parts produced with a laser power of 105 W and a scan speed of 250 mm/s. Three types of phase transitions can be distinguished.

The phase identification of these dark and bright phases is done based on XRD measurements and micro-hardness measurements.

The non-homogeneity in the macrostructure is taken under further investigation by performing micro-hardness tests to determine the hardness of both the bright and the dark phase. The results hereof are depicted in Figure 7.19. The bright zone has a micro-hardness of 846 ± 44 HV, while the dark zone has a hardness of 682 ± 32 HV, measured with a load of 0.5 kg. Based on these hardness results, in combination with the XRD measurements depicted in Figure 7.14, we conclude that the bright phase is martensite, and the dark phase is retained austenite. Similar martensitic structures were observed by [120, 119]

For higher scan speeds, the cooling rate is higher and more martensite is formed, as can be seen in Figure 7.17.

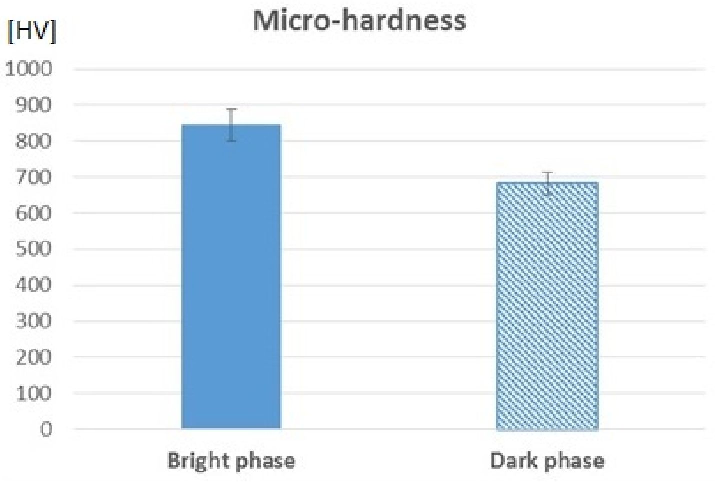

Figure 7.19: Vickers Micro-hardness of the bright and the dark phase in a part produced with P = 105 W, v = 250 mm/s, h = 128 μm. The results depict a 95 % confidence interval for 8 measurements.

7.7.2 SEM

The microstructure of the produced parts was observed under SEM. Both part with and without applying laser remelting were analyzed and in two directions: XY-plane (or top view) and YZ-plane (or side view). All parts that were observed under SEM were produced with a laser power of 105 W, a scan speed of 250 mm/s and a hatch spacing of 128 μm.

Without laser remelting

Figure 7.20 shows the XY plane of the produced part. The right image shows a higher magnification of the zone indicated in the left picture. The overall melt pool borders are seen in the left picture, while the right image enlarges the morphology of the melt pool border.

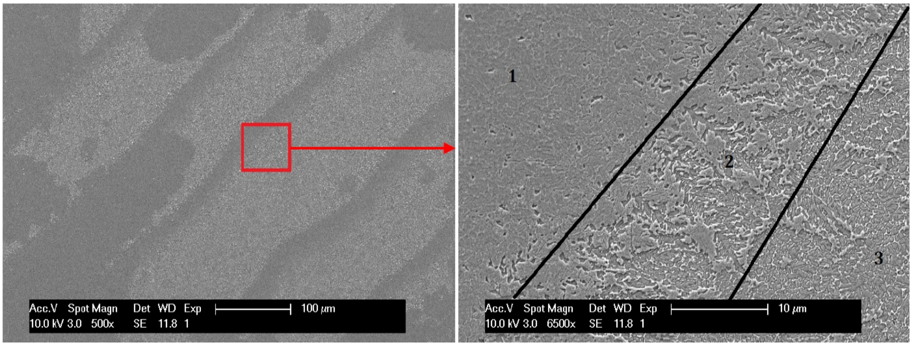

Figure 7.20: SEM image of a XY cross section for a part produced without remelting. Left: scan tracks in the XY plane. Right: Higher magnification of the melt pool border with indication of three different zones.

In the right image, three morphologies can be distinguished. The melt pool border is divided into three zones. Towards the middle of the melt pool, the microstructure becomes more coarse. A similar 3-zone morphology at the melt pool border was observed in A360 aluminum alloy by Thijs et al. [152].
Figure 7.21 shows the morphology of zone 1 more in detail. This first zone has a relatively coarse grain, with a cellular-dendritic morphology.

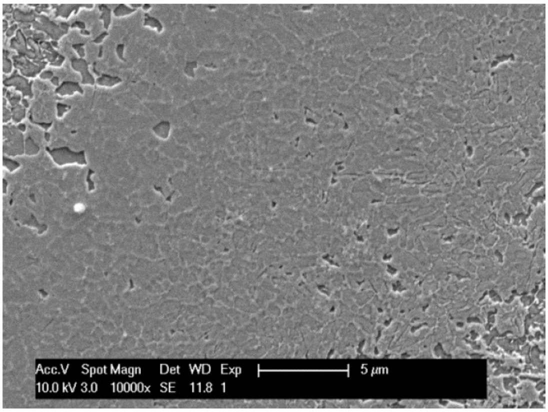

Figure 7.21: A detailed SEM view in the XY plane of zone 1 in the microstructure of a part produced without laser remelting.

Figure 7.22 shows a higher magnification of zone 2, which consists of a finer cellular-dendritic morphology. In the right image, an elongated grain is indicated by a red circle.

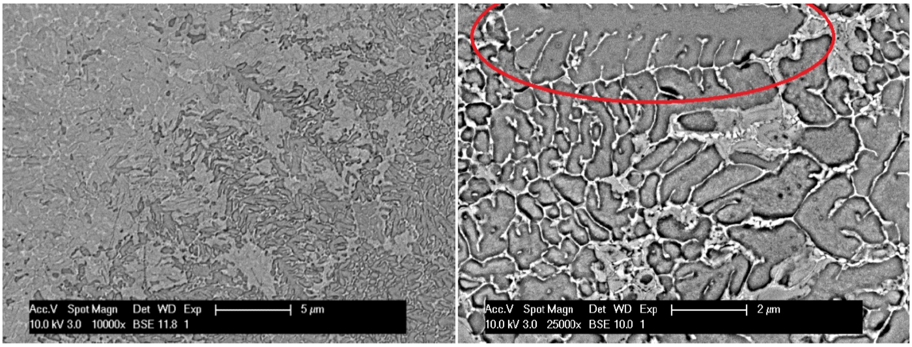

Figure 7.22: A detailed SEM view in the XY plane of zone 2 in the microstructure of a part produced without laser remelting. The red circle indicated an elongated grain that was formed in this zone.

In zone 3, the morphology is even more fine as the cells are smaller than 1 μm, as depicted in Figure 7.22. Upon close observation, lath martensite could be distinguished in the cells, which is consistent with the results of the microhardness and XRD measurements: martensite is present in the bright phase at the border of the melt pool (the heat affected zone).

Both in zones 2 and 3, there is a lighter phase between the grain boundaries, which could be an indication of carbide presence.

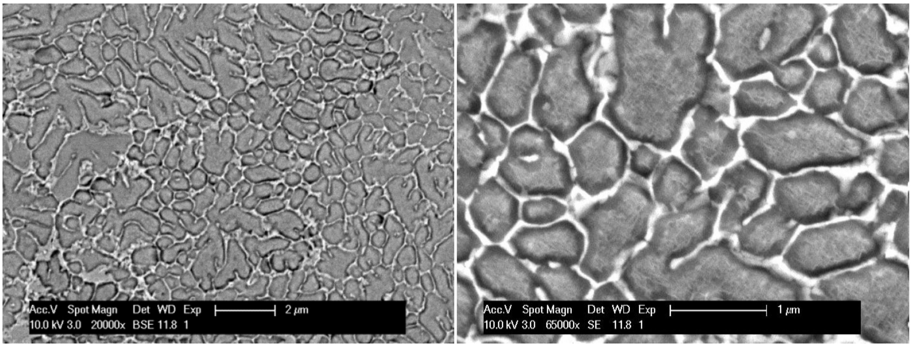

Figure 7.23: A detailed SEM view in the XY plane of zone 3 in the microstructure of a part produced without laser remelting.

While observing the cross-sectional view in the YZ-plane (Figure 7.24), these three morphological zones can also be seen. Zone 1 in the middle of the melt pool was observed into detail in Figure 7.25.

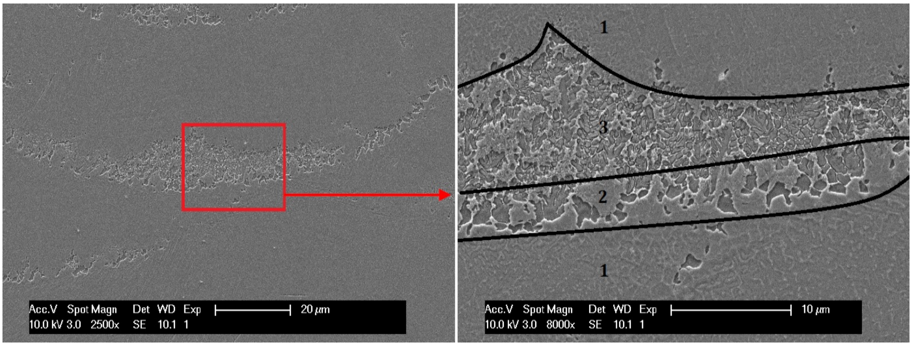

Figure 7.24: SEM image of a YZ cross section for a part produced without remelting. Left: scan tracks in the YZ plane. Right: Higher magnification of the melt pool border with indication of three different zones.

Also in this side view, the dendritic morphology is distinguished and it can be seen that the grains form towards the middle of the melt pool (and thus the heat source). A similar microstructure is observed by Kac et al. [71] upon CO_2 laser melting of M2 HSS. A very fine dendritic structure is characterized, with the orientation of the main dendrites in the direction of the heat transport. In this work as well, between the melted zone and heat-affected zone there is a transient zone, in which a cell structure is observed.

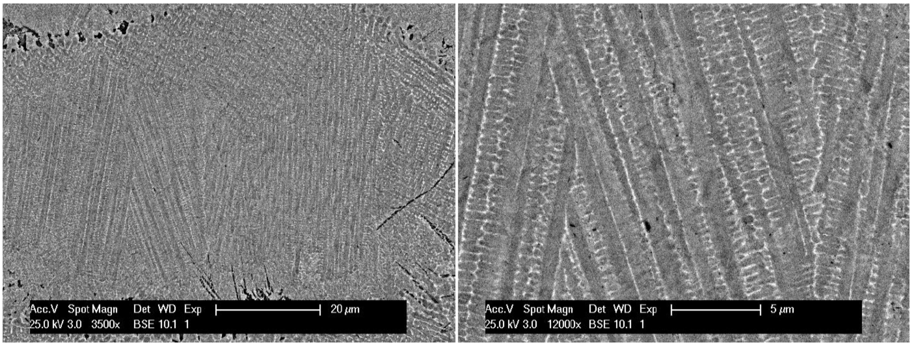

Figure 7.25: A detailed SEM view in the YZ plane of zone 1 in the microstructure of a part produced without laser remelting.

From zone 1 in the middle of the melt pool, towards zone 3 at the border, the grains are refined. The heat sink at the border of the melt pool is much bigger, thus explaining the finer microstructure. Similar microstructures are observed by Arias et al. [7, 6], Benyounis et al. [16] and Darmawan et al. [38] in laser melting of M2 HSS.

SLM + laser remelting

The laser remelting step is performed on solidified material, instead of powder material, and thus there is a different heat dissipation, resulting in a different microstructure. An overall view of the XY plane is shown in Figure 7.26. The scan tracks can be distinguished once again, as well as the three zones.

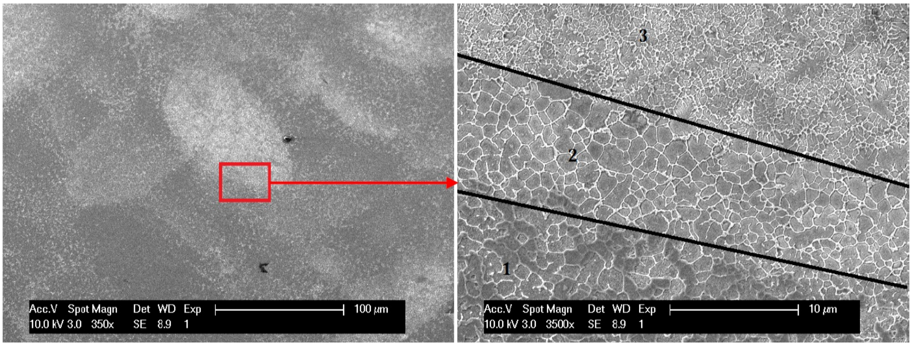

Figure 7.26: SEM image of a XY cross section for a part produced by SLM + laser remelting. Left: scan tracks in the XY plane. Right: Higher magnification of the melt pool border with indication of three different zones.

The detailed view of zone 1 is given in Figure 7.27. Compared to the parts produced without remelting (Figure 7.21), the grain boundaries are more clear, possibly due to carbide formation in this zone, indicated with a red arrow. Also, the dendritic morphology is no longer seen, rather than cellular morphology. Since the heat sink is greater for laser remelting, compared to the first melting step, this would explain the difference in morphology as a high heat sink results in smaller grain sizes.
The increase in carbides was also detected in XRD measurements in Figure 7.14.

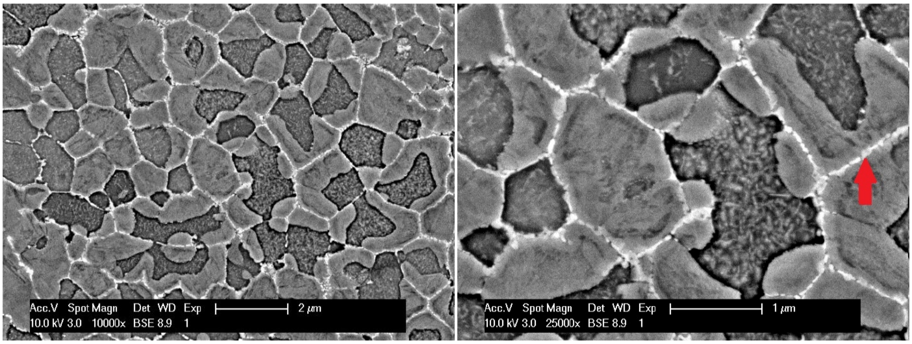

Figure 7.27: A detailed SEM view in the XY plane of zone 1 in the microstructure of a part produced by SLM + laser remelting. The red arrow indicates the location of possible carbides.

Figure 7.28 shows a magnification of zone 2 for a part produced with laser remelting. Like in zone 1, the grain boundaries are decorated with a white phase, which could be interpreted as carbides (indicated with a red arrow). The cells show a lath martensite structure, like in the parts produced without laser remelting.

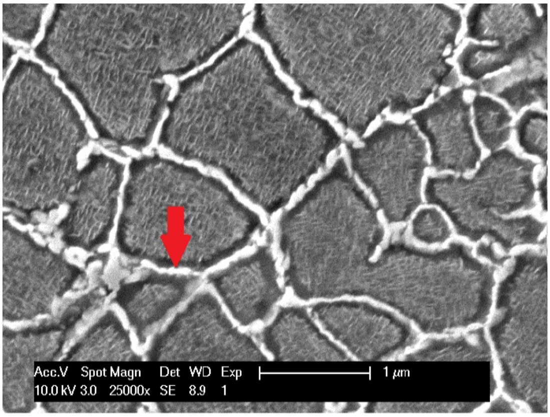

Figure 7.28: A detailed SEM view in the XY plane of zone 2 in the microstructure of a part produced by SLM + laser remelting.

The third zone which is shown in Figure 7.29 consists of the fine cellular structure, which is even finer after remelting than after the first scanning step, due to the higher cooling rates upon remelting.

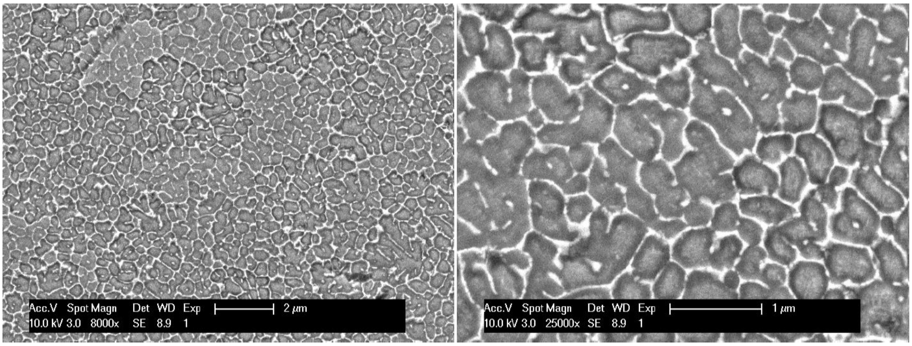

Figure 7.29: A detailed SEM view in the XY plane of zone 3 in the microstructure of a part produced by SLM + laser remelting.

7.8 Conclusions

1. The objective of this study, to produce crack-free M2 HSS parts with a high density by Selective Laser Melting, is achieved. The part with the maximum density of 99.8% is produced at a pre-heating of the baseplate of $200°C$, a laser power of 105 W, a scan speed of 150 mm/s and a hatch spacing of 126 μm. Lower scan speed, remelting and higher pre-heating temperature all lead to higher densities. The influence of these parameters on the density is strongly dependent on each other and it is not linear.
2. The best way to improve surface quality on the top surface is to apply remelting. A top surface roughness of 8.6 μm P_a has been reached by remelting.
3. When scanning without remelting, parameters which lead to a higher density, also lead to a better surface quality.
4. With the applications of M2 HSS in mind, we know that a high hardness is very important. The high hardness in conventional HSS M2 is obtained by an aging heat treatment. However, there is already an intrinsic heat treatment in the SLM process due to the typical characteristics of the process, which makes post heat treatment (with the goal to increase hardness) obsolete with SLM. In this study, hardness up to 57 HRC has been reached, without applying a post-treatment. Applying remelting in every layer, improves the hardness even up to 64 HRC, which is comparable to conventional heat treated M2 HSS.
5. Lowering the thermal gradient reduces the thermal stresses and hereby the amount of cracking. Pre-heating of the baseplate lowers the thermal gradient. It also lowers the cooling rate, leading to less martensite formation. Remelting leads to more cracks because the higher cooling rates lead to more formation of a brittle martensite phase. Similarly, in Shi et al. laser surface treatment was intentionally applied to increase the martensite phase for steel hardening [142].
6. Because of the high temperatures and cooling rates which are reached in the SLM-process, there is an inherent heat treatment that is applied to the SLM-produced parts, leading to a hardness and ultimate tensile strength approaching those of conventionally cast + heat treated parts.
7. The microstructure of M2 HSS parts produced with low scan speeds is inhomogeneous and consists of martensite and retained austenite. Possible carbides were detected by XRD. For high scan speeds or after applying remelting, the microstructure mainly consists of brittle martensite and is thus more prone to cracking.

Chapter 8

Conclusions

There is significant need for research to overcome the major problems and barriers in Selective Laser Melting of metal powders as defined in Chapter 2. That is why the overall objective of this thesis was defined as followed:

The overall goal of the thesis is to expand the materials palette in an empirical way, with high-demand materials fulfilling the prerequisites like full density and conventional mechanical properties. Along the way, barriers need to be overcome that characterize the SLM process, but prohibit it from reaching a higher technology readiness level, like thermal stresses, cracks and poor dimensional accuracy.
The scientific question to be answered is: What are the similarities and differences in processing different materials by SLM and is there a way to fasten the parameter optimization process?

Four different materials, divided in two material groups were processed in this work. The first part described the work on two aluminum alloys, a cast aluminum alloy A360 and a wrought aluminum alloy Al7075. The second part handles the process capabilities of two types of tool steel: a low-carbon maraging steel 18Ni300, and a high-carbon M2 High Speed Steel.

Overall conclusions

- The use of correct **powder material** is critical for the quality of the final SLM part. Powder morphology and size distribution determine the powder layer deposition, while the chemical composition of the powder influences the laser absorption and thus the melting behavior. It was shown that the powder with a spherical morphology and a broad particle size distribution leads to higher density parts.

- **Single track scans** offer a great amount of information on the formation of a melt pool and its characteristics. A low energy input per unit length results in droplet formation and a bad wetting to the previous layers or to the baseplate for the first layer. An energy input per unit length that is too high, causes a very deep melt pool and possibly keyhole porosity. For increasing scan speed, the melt pool width and depth decrease. A process window (laser power P - scan speed v) can be defined in which a stable melt pool is formed that meets the requirements for melt pool height, melt pool depth and connection angle. The parameters for optimal density will lie within this process window.

- By Selective Laser Melting, nearly fully **dense parts** can be produced, but the scan parameters have to be carefully optimized. Laser power P, scan speed v, layer thickness t and scan spacing h all have a strong, but non-linear influence on the resulting part density.
  For high laser powers, the range of scan speeds resulting in high-density parts becomes larger. Optimization of the scan spacing between scan tracks should not be underestimated. When the scan spacing is too large, the scan tracks will not connect, and unmolten powder will remain between the scan tracks. This results in a very low density and a rough top surface. For a very low scan spacing, the production time increases strongly and it could lead to pores if the scan track lies within the denudation zone of the adjacent track.
  Two types of pores remain after the SLM process: bigger, irregular pores and smaller spherical pores. The pores due to evaporation and gas are small and spherical in shape. The pores due to insufficient overlap of neighboring scan tracks are bigger and irregular.

- **Laser remelting** every layer has proven to increase the density significantly and is the best way to improve the surface roughness, if laser remelting parameters are chosen properly. Post-processing however might still be needed, as the average top surface roughness still reaches 8 μm after laser remelting.
  During the laser remelting step, there is a different heat flux for melting of solidified material, compared to powder material. The microstructure after laser remelting is even more refined because of the bigger heat sink in laser remelting, and thus the micro-hardness is even further increased compared to SLM-produced parts without laser remelting.

Laser remelting however has serious implications on the total production time.

- The **macrostructure** of SLM processed alloys (with exception of Ti6Al4V) shows the footprint of the scan strategy. The semi-circular melt pools can be distinguished. Due to the high cooling rates which are inherent to the process, solidification takes place by cellular-dendritic growth mechanisms. In the microstructure, the inter-cellular spacing is less than 1 μm which contributes to the excellent strength and hardness achieved in both as-produced and heat treated conditions.

- The **mechanical properties** (strength, hardness) in the as-built condition for nearly fully dense parts are comparable or even exceed those of conventionally cast or wrought test samples, which underwent the standard heat treatment. The very fine microstructure that is inherent to the SLM process conditions contributes to these high hardness and strength. Moreover, the high temperatures that are reached during SLM processing can result in an intrinsic heat treatment during the SLM process. For M2 HSS for example, carbides were detected in the as-built condition, without applying a post-process heat treatment.

- The standard **heat treatments** that are defined for hardening and strengthening of materials, are not optimal for SLM produced parts. Due to the intrinsic heat treatment and the very fine microstructure which is inherent to the SLM process, there is a need for a different heat treatment, or even no heat treatment at all. The annealing step that is often included in a standard post-processing cycle would undo the fine cellular microstructure, thus lowering the high hardness and strength that were reached after SLM processing. A sole aging step can improve the mechanical properties of SLM parts further, by formation of e.g. precipitates or carbides.

- The Selective Laser Melting process is characterized by high **residual stresses**, which can lead to cracks, delamination from the baseplate and warpage. There are two phenomena that may induce residual thermal stresses: (i) induced stresses in the solid substrate just underneath the present layer being melted and (ii) stresses due to the cool-down phase of the melted top layers. Brittle phases like martensite are more prone to crack formation when under stress, but on the other hand also contribute to the high hardness.
  The thermal stresses can be lowered by pre-heating the baseplate. The thermal gradients are lowered and it is shown that cracks can be eliminated for M2 HSS parts of 15 x 15 x 10 mm, when using a baseplate pre-heating of 200°.

Thermal stresses however, are not the only cause of cracks in SLM parts. Wrought aluminum alloys for example, were not designed to be formed in the liquid state, as they have a high thermal expansion coefficient. As a result, Al7075 parts produced by SLM will contain cracks. A solution that was tested in this work is the addition of silicon powder to the powder mixture. Silicon lowers the thermal expansion coefficient, but also the strength, so a trade-off has to be made. After addition of 3 wt% of silicon, cracks-free parts can be produced. The influence of the addition of silicon on mechanical properties is a strong suggestion for future work.

- Producing downfacing structures is still the biggest barrier regarding **dimensional accuracy** of SLM produced parts. Four possible ways to deal with dross formation are: re-orientation of the part, shape compensation, parameter adaptation and re-design of the final part.
  The method of parameter adaptation was explored in this work. A melt pool with a similar shape and size as during standard processing is formed at a lower laser power, due to the difference in heat flow in powder, compared to solid material. To ensure a good transition from downfacing parameters to standard parameters, the volume above the downfacing area is divided into five different zones, with transitioning scan parameters. The method has shown to be successful for both horizontal downfacings, and inclined downfacings, where three zones are sufficient.

Overall, it can be concluded that process optimization for new materials is still very material-dependent. Although some conclusions are valid for all four alloys processed in this work (and others, as concluded from literature), every material has its challenges. The workflow in process parameter optimization can be used for any material, as soon as crack-free production is possible. Cracks resulting from thermal stresses can be avoided by the use of pre-heating. The advantage of baseplate pre-heating is that is can be used for any material, and it is relatively easy to control. However, by lowering the thermal gradient, the microstructure will also become more coarse and the superior mechanical properties after SLM might be lost.
Cracks due to shrinkage can be eliminated by mixing additional powder materials. The fine microstructure inherent to the SLM process remains, but it is crucial to determine the right alloying element and the right amount, as it will also affect the material properties. Moreover, a homogeneous distribution of the new alloying element is not guaranteed.

Suggestions for Future Work

A brief overview is given of some suggestions for further work:

- Further parameter optimization for the production of fully dense Al7075 parts, and characterization thereof (mechanical and physical properties, microstructure, etc..).
- Laser remelting in this work was applied for every layer, in order to achieve high density parts. This has severe implications on the total production time of the part. Further research could include the effect of the number of remelting steps (e.g. every two or three layers) . An optimal trade-off between part quality and productivity needs to be considered.
- As SLM parts find many of their applications in aerospace and automotive industries, fatigue and fracture toughness properties need to be considered. These have not been tested in this work, and are strongly suggested in further research of these materials.
- The standard heat treatments that were defined for each alloy are not optimal for SLM produced parts. The optimization of the heat treatment for SLM produced 18Ni300 maraging steel was done in this work, but should also be considered for other materials.
- In this work, pre-heating was used to avoid cracks in brittle materials prone to the thermal stresses in SLM. The tests here were limited to 15 x 15 x 10 mm cubes. Further studies are recommended to determine the pre-heating temperature that is needed for other geometries and volumes. The same pre-heating system can also be used for parts that do not contain cracks, but to alter/influence the part's microstructure and resulting mechanical properties. More in-depth research and modeling is needed to fully understand the influence of different pre-heating process conditions, mechanical properties, density, etc.
  Moreover, other pre-heating methods can be considered like infrared heating, microwave heating or heating from the top instead of the baseplate.
- A broad field of research lies in the mixture of different powders. As SLM enables the incorporation of alloying element that can not be alloyed in the conventional way, this opens many new perspectives on alloy compositions and their resulting physical and mechanical properties.

Bibliography

[1] Abe, F., Costa Santos, E., Kitamura, Y., Osakada, K., and Shiomi, M. Influence of forming conditions on the titanium model in rapid prototyping with the selective laser melting process. *Proceedings of the Institution of Mechanical Engineers, Part C: Journal of Mechanical Engineering Science 217*, 1 (2003), 119–126.

[2] Abe, F., Osakada, K., Shiomi, M., Uematsu, K., and Matsumoto, M. The manufacturing of hard tools from metallic powders by selective laser melting. *Journal of Materials processing technology 111*, 1 (2001), 210–213.

[3] Alimardani, M., Toyserkani, E., Huissoon, J., and Paul, C. On the delamination and crack formation in a thin wall fabricated using laser solid freeform fabrication process: an experimental-numerical investigation. *Optics and lasers in engineering 47*, 1 (2009), 1160–1168.

[4] American iron and steel institute. Online, 2014. http://www.steel.org.

[5] Arata, Y., Matsuda, F., Mukae, S., and Katoh, M. Effect of weld solidification mode on tensile properties of aluminum weld metal. *Transactions of JWRI 2*, 2 (1973), 184–190.

[6] Arias, J., Cabeza, M., Castro, G., Feijoo, I., Merino, P., and Pena, G. Microstructure and mechanical behavior of laser surface melted AISI M2 high-speed steel. *Surface and Interface Analysis 42*, 6-7 (2010), 752–756.

[7] Arias, J., Cabeza, M., Castro, G., Feijoo, I., Merino, P., and Pena, G. Modification of AISI M2 high speed tool steels after laser surface melting under different operation conditions. *Revista de Metallurgia 46*, 3 (2010), 206–218.

[8] ASM INTERNATIONAL. *ASM Handbook.* ASM International, 1991, ch. Volume 4: Heat Treating.

[9] ASM INTERNATIONAL. *ASM Handbook.* ASM International, Volume 1:, 1991.

[10] ASTM INTERNATIONAL. ASTM standard E23-96: Standard test methods for notched bar impact testing of metallic materials, 2012.

[11] ASTM INTERNATIONAL. ASTM standard F2792-12a: Terminology for additive manufacturing technologies. DOI 10.1520/F2792-12A, 2012.

[12] BADROSSAMAY, M., AND CHILDS, T. Further studies in selective laser melting of stainless and tool steel powders. *International Journal of Machine Tools and Manufacture 47*, 5 (2007), 779 – 784.

[13] BADROSSAMAY, M., YASA, E., VAN VAERENBERGH, J., AND KRUTH, J.-P. Improving productivity rate in SLM of commercial steel powders. In *SME RAPID, Schaumburg Illinois USA* (2009).

[14] BAILEY, N. *Residual Stresses.* The Welding Institute, 1981, ch. The Metallurgical Effects of Residual Stresses.

[15] BAUFELD, B., BRANDL, E., AND VAN DER BIEST, O. Wire based additive layer manufacturing: Comparison of microstructure and mechanical properties of Ti–6Al–4V components fabricated by laser-beam deposition and shaped metal deposition. *Journal of Materials Processing Technology 211*, 6 (2011), 1146 – 1158.

[16] BENYOUNIS, K., FAKRON, O., AND ABBOUD, J. Rapid solidification of M2 high-speed steel by laser melting. *Materials and Design 30*, 3 (2009), 674 – 678.

[17] BERKAU, A., AND SCHWARZE, D. New possibilities in additive manufacturing of aluminium parts. In *6. Anwenderforum Rapid Product Development* (2011).

[18] BOURELL, D., LEU, M., AND ROOSEN, D. Roadmap for additive manufacturing: identifying the future of freeform processing, August 2009. Industrial roadmap for USA.

[19] BRAGG, W. The diffraction of short electromagnetic waves by a crystal. In *Proceedings of the Cambridge Philosophical Society* (1913), vol. 17, pp. 43–57.

[20] Brandl, E., Heckenberger, U., Holzinger, V., and Buchbinder, D. Additive manufactured AlSi10Mg samples using selective laser melting (SLM): Microstructure, high cycle fatigue and fracture behaviour. *Journal of materials and design 34* (2012), 159–169.

[21] Brandl, E., Palm, F., Michailov, V., Viehweger, B., and Leyens, C. Mechanical properties of additive manufactured titanium (Ti6Al4V) blocks deposited by a solid-state laser and wire. *Materials and Design 32*, 10 (2011), 4665 – 4675.

[22] Brans, K., and Craeghs, T. STREAM structural engineering materials with additive manufacturing, September 2012. Industrial roadmap for Flanders.

[23] Buchbinder, D., Meiners, W., Wissenbach, K., Mueller-Lohmeier, K., Brandl, E., and Skrynecki, N. Rapid manufacturing of aluminum parts for serial production via selective laser melting (SLM). In *International Conference on Rapid Manufacturing, 8th and 9th July 2009. Loughborough* (2009), vol. 4, pp. 1–12.

[24] Buchbinder, D., Schleifenbaum, H., Heidrich, S., Meiners, W., and Bultmann, J. High power selective laser melting (HP SLM) of aluminum parts. *Physics Procedia 12, Part A*, 0 (2011), 271 – 278. Lasers in Manufacturing 2011 - Proceedings of the Sixth International WLT Conference on Lasers in Manufacturing.

[25] Buls, S., Craeghs, T., Clijsters, S., kempen, K., Swevers, J., and Kruth, J.-P. The influence of a dynamically optimized galvano based laser scanner on the total scan time of SLM parts. In *Proceedings of the 24th Solid Freeform Fabrication Symposium* (2013), pp. 260–266.

[26] Calignano, F., manfredi, D., Ambrosio, E., and Iuliano, L. Influence of process parameters on surface roughness of aluminum parts produced by DMLS. *International jounrla of advanced manufacturing technology 67* (2013), 2743 – 2751.

[27] Campanelli, S., Contuzzi, N., and Ludovico, A. Manufacturing of 18 Ni marage 300 steel samples by selective laser melting. *Advanced Materials Research 83–86* (2010), 850–857.

[28] Casalino, G., Campanelli, S., Contuzzi, N., and Ludovico, A. Experimental investigation and statistical optimisation of the selective laser melting process of a maraging steel. *Optics & Laser Technology 65* (2015), 151–158.

[29] Casavola, C., Campanelli, S., and Pappalettere, C. Preliminary investigation on distribution of residual stress generated by the selective laser melting process. *The Journal of Strain Analysis for Engineering Design 44*, 1 (2009), 93–104.

[30] Casavola, C., Pappalettere, C., and Tursi, F. Residual stress on AISI 300 sintered materials - effect of thickness. *Structural Integrity and life 12*, 3 (2012), 153–158.

[31] Childs, T., Hauser, C., and Badrossamay, M. Mapping and modelling single scan track formation in direct metal selective laser melting. *CIRP Annals - Manufacturing Technology 53*, 1 (2004), 191–194.

[32] Childs, T., Hauser, C., and Badrossamay, M. Selective laser sintering (melting) of stainless and tool steel powders: experiments and modelling. *Journal of Engineering manufacture 219*, 4 (2005), 339–357.

[33] Clijsters, S. *Development of a Smart Selective Laser Melting Process (by introducing advanced job preparation and process monitoring).* PhD thesis, University of Leuven (KU Leuven), Department of Mechanical Engineering, 2014.

[34] Clijsters, S., Craeghs, T., Moesen, M., and Kruth, J.-P. Optimization of thin wall structures in SLM. In *Direct Digital manufacturing Conference* (2012).

[35] Concept laser gmbh. Online, May 2014. http://www.concept-laser.de.

[36] Conde, A., Garcia, I., and de Damborena, J. Pitting corrosion of 304 stainless steel after laser surface melting in argon and nitrogen atmospheres. *Corrosion Science 43*, 5 (2001), 817 – 828.

[37] Consultants, R. B. S. Additive manufacturing: a game changer for the manufacturing industry? On the WWW, November 2013. http://www.rolandberger.com.

[38] Darmawan, W., Quesada, J., Rossi, F., Marchal, R., Machi, F., and Usuki, H. Improvement in wear characteristics of the AISI M2 by laser cladding and melting. *Journal of Laser Applications 21*, 4 (2009), 176–182.

[39] Das, S. Physical aspects of process control in selective laser sintering of metals. *Advanced Engineering Materials 5*, 10 (2003), 701–711.

[40] Das, S., McWilliams, J., Wu, B., and Beaman, J. Design of a high temperature workstation for the selective laser sintering process.

In *Proceedings of the 2nd Solid Freeform Fabrication Symposium* (1991), pp. 164–170.

[41] Das, S., Wohlert, M., Beamen, J., and Bourell, D. Processing of titanium net shapes by SLS/HIP. *Materials and Design 20*, 2 (1999), 115–121.

[42] Dawes, C. *Laser Welding - A practical guide.* Abington Publishing, Cambridge, 1992.

[43] de Wolf, W. Directspare : Strengthening the industries competitive position by the development of a logistical and technological system for spare parts that is based on on-demand production. FP7 collaborative project, February 2012. Generic roadmap for spare part markets.

[44] Dinda, G., Dasgupta, A., and Mazumder, J. Evolution of microstructure in laser deposited Al 11.28%Si alloy. *Surface and Coatings Technology 206*, 8–9 (2012), 2152 – 2160.

[45] Dinda, G., Song, L., and Mazumder, J. Fabrication of Ti-6Al-4V scaffolds by Direct Metal Deposition. *Metallurgical and Materials Transactions A 39*, 12 (2008), 2914–2922.

[46] Duflou, J., Callebaut, B., and Kruth, J.-P. Laserforming of 3D features. *Advanced Materials Research 6–8*, 4 (2005), 425–432.

[47] Electro optical systems, EOS GmbH. Online, May 2014. http://www.eos.info.

[48] Facchini, L., magalini, E., Robotti, P., and Molinari, A. Microstructure and mechanical properties of Ti-6Al-4V produced by electron beam melting of pre-alloyed powders. *Rapid Prototyping Journal 15*, 3 (2009), 171 – 178.

[49] Fitzpatrick, M., Fry, A., Holdway, P., Kandil, F., Schckleton, J., and Suominen, L. *Measurement good practice guide no. 52, Determination of residual stresses by X-ray diffraction.* National Physical Laboratory,, Issue 2, 2005.

[50] Flagship. Heat treated aluminium high pressure die castings. Technical data sheets, May 2014.

[51] GE Aviation. Online, May 2014. http://www.geaviation.com/.

[52] Gebhardt, A., Fateri, M., Hotter, J.-S., Schmidt, F.-M., and Rieper, H. Numerical and experimental investigation of selective laser melting of silver. In *Fraunhofer Direct Digital manufacturing Conference* (2011).

[53] Gebhardt, A., Hoetter, J.-S., and Ziebura, D. Impact of SLM build parameters on the surface quality. *RTejournal - Forum fur Rapid Technologie 2014*, 1 (2014).

[54] Gerlich, D., Roberts, R., White, G., and Tainsh, R. Thermoelastic properties of 350 grade maraging steel. *Journal of materials Science 25*, 4 (1990), 2249–2252.

[55] Griffith, M., Keicher, D., Atwood, C., Romero, J., Smugeresky, J., Harwell, L., and Greene, D. Free form fabrication of metallic components using laser engineered net shaping (LENS). In *Proceedings of the Solid Freeform Fabrication Symposium* (1996), pp. 125–131.

[56] Gu, D., Meiners, W., Wissenbach, K., and Poprawe, R. Laser additive manufacturing of metallic components: materials, processes and mechanisms. *International Materials Reviews 57*, 3 (2012), 133–164.

[57] Gusarov, A., Yadroitsev, I., Bertrand, P., and Smurov, I. Model of radiation and heat transfer in laser-powder interaction zone at selective laser melting. *Journal of heat treansfer 131*, 7 (2009).

[58] Haboudou, A., Peyre, P., Vannes, A., and Peix, G. Reduction of porosity content generated during nd:yag laser welding of {A356} and {AA5083} aluminium alloys. *Materials Science and Engineering: A 363*, 1 - 2 (2003), 40 – 52.

[59] Hagedorn, Y., Balachandran, N., Meiners, W., Wissenbach, K., and Poprawe, R. SLM of net-shaped high strength ceramics: new opportunities for producing dental restorations. In *Proceedings of the Solid Freeform Fabrication Symposium* (2011), pp. 536–546.

[60] Hansson, K. N., and Hansson, S. Skewness and kurtosis: Important parameters in the characterization of dental implant surface roughness - a computer simulation. *Materials Science* (2011), 305312.

[61] Hao, L., and Lawrence, J. Effects of Nd:YAG laser treatment on the wettability characteristics of a zirconia-based bioceramic. *Optics and Lasers in Engineering 44*, 8 (2006), 803 – 814.

[62] Harrysson, O., Cansizoglu, O., Marcellin-Little, D. J., Cormier, D. R., and II, H. A. W. Direct metal fabrication of titanium implants with tailored materials and mechanical properties using electron beam melting technology. *Materials Science and Engineering: C 28*, 3 (2008), 366 – 373.

[63] Herzog, F. Method for the production of three-dimensional sintered workpieces, patent of CL island scanning, October 2001. Europaeische Patentschrift EP 1 441 897 B1.

[64] Holzweissig, M. J., Taube, A., Brenne, F., Schaper, M., and Niendorf, T. Microstructural characterization and mechanical performance of Hot Work Tool Steel processed by Selective Laser Melting. *Metallurgical and Materials Transactions B*, 1–5.

[65] Ion, J. *Laser Processing of Engineering Materials: principles, procedure and industrial application.* Elsevier Butterworth-Heinemann, Oxford, 2005.

[66] Izcara, X. L., Blank, A. G., Pyczak, F., Staron, P., Schumann, S., and Huber, N. Characterization and modeling of the influence of artificial aging on the microstructural evolution of age-hardenable AlSi10Mg(Cu) aluminum alloys. *Materials Science and Engineering: A 610*, 0 (2014), 46 – 53.

[67] Jägle, E. A., Choi, P.-P., Van Humbeeck, J., and Raabe, D. Precipitation and austenite reversion behavior of a maraging steel produced by selective laser melting. *Journal of Materials Research 29*, 17 (2014), 2072–2079.

[68] Jain, P. K., Pandey, P. M., and Rao, P. Effect of delay time on part strength in selective laser sintering. *The International Journal of Advanced Manufacturing Technology 43*, 1-2 (2009), 117–126.

[69] Jhabvala, J., Boillat, E., Andre, C., and Glardon, R. An innovative method to build support structures with a pulsed laser in the selective laser melting process. *The International Journal of Advanced Manufacturing Technology 59*, 1-4 (2012), 137–142.

[70] Jhabvala, J., Boillat, E., Antignac, T., and Glardon, R. On the effect of scanning strategies in the selective laser melting process. *Virtual and Physical prototyping 5*, 2 (2010), 99–109.

[71] Kac, S., and Kusinski, J. {SEM} and {TEM} microstructural investigation of high-speed tool steel after laser melting. *Materials Chemistry and Physics 81*, 2–3 (2003), 510 – 512.

[72] Karapatis, P. *A sub-process approach of Selective Laser Sintering.* PhD thesis, Ecole Polytechnique federal de Lausanne, 2002.

[73] Karner, C., Bauereiss, A., and Attar, E. Fundamental consolidation mechanisms during selective beam melting of powders. *Modelling and Simulation in Materials Science and Engineering 21*, 8 (2013), 085011.

[74] Kazanas, P., Deherkar, P., Almeida, P., Lockett, H., and Williams, S. Fabrication of geometrical features using wire and arc additive manufacture. *Proceedings of the Institution of Mechanical Engineers, Part B: Journal of Engineering Manufacture 226*, 6 (2012), 1042–1051.

[75] Kearney, A. *ASM Handbook.* ASM International, 1990, ch. Volume 2: Properties and Selection Nonferrous Alloys and Special-Purpose Materials.

[76] Kempen, K., Thijs, L., Humbeeck, J. V., and Kruth, J.-P. Processing alsi10mg by selective laser melting: Parameter optimization and material characterization. *Materials Science and Technology* (2015).

[77] Kempen, K., Vrancken, B., Buls, S., Thijs, L., Humbeeck, J. V., and Kruth, J.-P. Selective laser melting of crack-free high density m2 hss parts by baseplate pre-heating. *Journal of manufacturing Science and Engineering 136*, 6 (2014).

[78] Koike, M., Greer, P., Owen, K., Lilly, G., Murr, L., Gaytan, S., Martinez, E., and Okabe, T. Evaluation of titanium alloys fabricated using rapid prototyping technologies : Electron beam melting and laser beam melting. *Materials 4*, 10 (2011), 1776–1792.

[79] Kou, S. *Welding Metallurgy.* Cambridge University press, Cambridge, 2002.

[80] Kovacheva, R. Metallographic investigation of Al-Si-Mg and al-si-cu alloys. *Praktische Metallographie 30*, 2 (1993), 68–81.

[81] Kruth, J.-P. *Niet-conventionele bewerkingsmethoden: deel 1.* Acco, Belgium, 2013. ISBN 9789033452635.

[82] Kruth, J.-P., Badrossamay, M., Yasa, E., Deckers, J., L.Thijs, and Humbeeck, J. V. Part and material properties in selective laser melting of metals. In *16th International Symposium on Electromachining (ISEM XVI). Shanghai-China* (2010).

[83] Kruth, J.-P., Bartscher, M., Carmignato, S., Schmitt, R., De Chiffre, L., and Weckenmann, A. Computed tomography for dimensional metrology. *CIRP Annals-Manufacturing Technology 60*, 2 (2011), 821–842.

[84] Kruth, J.-P., Froyen, L., Vaerenbergh, J. V., Mercelis, P., Rombouts, M., and B.Lauwers. Selective laser melting of iron-based powder. *Materials Processing Technology 149*, 1 (2004), 616–622.

[85] Kruth, J.-P., Levy, G., Klocke, F., and Childs, T. Consolidation phenomena in laser and powder-bed based layered manufacturing. *CIRP Annals - Manufacturing Technology 56*, 2 (2007), 730 – 759.

[86] Kruth, J.-P., Peeters, P., T.Smolderen, Bonse, J., T.Laoui, Froyen, L., and Bernard, A. Comparison between CO2 and Nd:YAG lasers for use with selective laser sintering of steel-copper powders. *Revue internationale de CFAO et d'informatique graphique 13*, 4-6 (1998), 95–110.

[87] Kruth, J.-P., Wang, X., Laoui, T., and Froyen, L. Lasers and materials in selective laser sintering. *Assembly Automation 23*, 4 (2003), 357–371.

[88] Kurz, W., and Fisher, D. J. Fundamentals of solidification. *Trans Tech Publications Ltd, Trans Tech House 244* (1986).

[89] Lamikiz, A., Sanchez, J., de Lacalle, L. L., and Arana, J. Laser polishing of parts built up by selective laser sintering. *International Journal of Machine Tools and Manufacture 47*, 12–13 (2007), 2040 – 2050.

[90] Latrobe specialty steel company Marvac 300 vim-var data sheet. Technical data sheets, 2009.

[91] Levy, G. N., Schindel, R., and Kruth, J. Rapid manufacturing and rapid tooling with layer manufacturing (LM) technologies, state of the art and future perspectives. *CIRP Annals - Manufacturing Technology 52*, 2 (2003), 589 – 609.

[92] Li, R., Liu, J., Shi, Y., Wang, L., and Jiang, W. Balling behavior of stainless steel and nickel powder during selective laser melting process. *The International Journal of Advanced Manufacturing Technology 59*, 9-12 (2012), 1025–1035.

[93] Li, R., Shi, Y., Wang, Z., Liu, J., and Jiang, W. Densification behavior of gas and water atomized 316l stainless steel powder during selective laser melting. *Applied Surface Science 256*, 2 (2010), 4350–4356.

[94] Li, Y., Yang, H., Lin, X., Huang, W., Li, J., and Zhou, Y. The influences of processing parameters on forming characterizations during laser rapid forming. *Materials Science and Engineering: A 360*, 1–2 (2003), 18 – 25.

[95] Liu, A., Chua, C., and Leong, K. Properties of test coupons fabricated by selective laser melting. *Key Engineering materials 447* (2010), 780 – 784.

[96] Louvis, E., Fox, P., and Sutcliffe, J. Selective laser melting of aliminium components. *Journal of materials processing technology 211*, 1 (2011), 275–284.

[97] LPW technology LTD. Online, May 2014. http://www.lpwtechnology.com.

[98] Ma, P., Prashanth, K. G., Scudino, S., Jia, Y., Wang, H., Zou, C., Wei, Z., , and Eckert, J. Influence of annealing on mechanical properties of Al-20Si processed by selective laser melting. *Metals 4*, 1 (2014), 28 – 36.

[99] Ma, Z., Samuel, E., Mohamed, A., Samuel, A., Samuel, F., and Doty, H. Influence of aging treatments and alloying additives on the hardness of Al–11Si–2.5 Cu–Mg alloys. *Materials & Design 31*, 8 (2010), 3791–3803.

[100] Manfredi, D., Calignano, F., krishnan, M., canali, R., Ambrosio, E., and Atzeni, E. From powders to dense metal parts: characterization of a commercial AlSiMg alloy processed through direct metal laser sintering. *Materials 6*, 3 (2013), 856 – 869.

[101] Materialise. Online, May 2014. http://www.materialise.com/.

[102] Mazumder, J., Choi, J., Nagarathnam, K., Koch, J., and Hetzner, D. The direct metal deposition of H13 tool steel for 3-D components. *Journal Of Materials 49*, 5 (1997), 55–60.

[103] Meier, H., and Haberland, C. Experimental studies on selective laser melting of metallic parts. *Materials Science and Engineering Technology 39*, 9 (2008), 665–670.

[104] Meiners, W. *Direktes Selektives Laser Sintern einkomponentiger metallisher Werkstoffe.* PhD thesis, Rheinisch-Westfaelische Technische Hochschule Aachen, 1999.

[105] Mercelis, P. *Control of selective laser sintering and selective laser melting processes.* PhD thesis, University of Leuven (KU Leuven), Department of Mechanical Engineering, 2007.

[106] Mercelis, P., and Kruth, J.-P. Residual stresses in selective laser sintering and selective laser melting. *Rapid Prototyping Journal 12*, 5 (2006), 254–265.

[107] Mertens, R., Clijsters, S., Kempen, K., and Kruth, J.-P. Optimization of scan strategies in selective laser melting of aluminium parts with downfacing areas. *Journal of Manufacturing Science and Engineering 136*, 6 (2014).

[108] Messler, R. *Principles of welding.* John Wiley and Sons, USA, 2008.

[109] Mills, K., Keene, B., Brooks, R., and Shirali, A., Eds. *Marangoni effects in welding.* Philosophical transactions. Royal Society of London series of Mathematical, Physical and Engineering Sciences, 1998, pp. 911–926.

[110] Morgan, R., Papworth, A., Sutcliffe, C., Fox, P., and O'neill, W. High density net shape components by direct laser re-melting of single-phase powders. *Journal of Materials Science 37*, 15 (2002), 3093–3100.

[111] Mudge, R. P., and Wald, N. R. Laser engineered net shaping advances additive manufacturing and repair. *Welding Journal New York 86*, 1 (2007), 44–48.

[112] Mumtaz, K. A., Erasenthiran, P., and Hopkinson, N. High density selective laser melting of waspaloy. *Journal of Materials Processing Technology 195*, 1 - 3 (2008), 77 – 87.

[113] Murr, L., Esquivel, E., Quinones, S., Gaytan, S., Lopez, M., Martinez, E., Medina, F., Hernandez, D., Martinez, E., Martinez, J., Stafford, S., Brown, D., Hoppe, T., Meyers, W., Lindhe, U., and Wicker, R. Microstructures and mechanical properties of electron beam rapid manufactured Ti6Al4V biomedical prototypes compared to wrought Ti6Al4V. *Materials Characterization 60*, 2 (2009), 96–105.

[114] Murr, L., Quinones, S., Gaytan, S., Lopez, M., Rodela, A., Martinez, E., Hernandez, D., Medina, F., and Wicker, R. Microstructure and mechanical behavior of Ti6Al4V produced by rapid layer manufacturing, for biomedical applications. *Journal of the mechanical behavior of biomedical materials 2*, 1 (2009), 20–32.

[115] Murray, J., and McAlister, A. *ASM Handbook.* ASM International, 1992, ch. Volume 3: Alloy Phase Diagrams.

[116] Ng, C., Savalani, M., Man, H., and Gibson, I. Layer manufacturing of magnesium and its alloy structures for future applications. *Virtual and Physical prototyping 5*, 1 (2010), 13–19.

[117] Nickels, L. Channelling quality for moulded parts using fast manufacturing. *Metal Powder Report 64*, 8 (2009), 8–12.

[118] Niu, H., and Chang, I. Selective laser sintering of gas and water atomized high speed steel powders. *Scripta Materialia 41*, 1 (1999), 25–30.

[119] Niu, H., and Chang, I. Microstructural evolution during laser cladding of M2 high-speed steel. *Metallurgical and materials transactions A 31*, 10 (2000), 2615–2625.

[120] Niu, H., and Chang, T. Selective laser sintering of gas atomized M2 high speed steel powder. *Journal of materials science 35* (2000), 31–38.

[121] Nowell, D., Hills, D., and Tochilin, S. Use of the crack compliance method for the measurement of residual stress. In *Proceedings of the 6th International Conference on Residual Stresses* (2000), vol. 2, pp. 845–852.

[122] Noyan, I. C., Huang, T. C., and York, B. R. Residual stress/strain analysis in thin films by X-ray diffraction. *Critical Reviews in Solid State and Materials Sciences 20*, 2 (1995), 125–177.

[123] Olakanmi, E. Selective laser sintering/melting of pure Al, Al-Mg and Al-Si powders: effect of processing conditions and powder properties. *Journal of Materials Processing Technology 213* (2013), 1387–1405.

[124] Pardal, J., Tavares, S., Fonseca, M. C., Abreu, H., and Silva, J. Study of the austenite quantification by X-ray diffraction in the 18Ni-Co-Mo-Ti maraging 300 steel. *Journal of materials science 41*, 8 (2006), 2301–2307.

[125] Pardal, J., Tavares, S., Terra, V., Da Silva, M., and Dos Santos, D. Modeling of precipitation hardening during the aging and overaging of 18Ni–Co–Mo–Ti maraging 300 steel. *Journal of alloys and compounds 393*, 1 (2005), 109–113.

[126] Peng, L., Shengqin, J., Xiaoyan, Z., Qianwu, H., and Weihao, X. Direct laser fabrication of thin-walled metal parts under open-loop control. *International Journal of Machine Tools and Manufacture 47*, 6 (2007), 996 – 1002.

[127] Pinkerton, A., and Li, L. Effects of powder geometry and composition in coaxial laser deposition of 316L steel for rapid prototyping for rapid prototyping. *CIRP Annals - Manufacturing Technology 52*, 1 (2003), 181–184.

[128] Pinkerton, A., and Li, L. Direct additive laser manufacturing using gas- and water-atomised H13 tool steel powders. *International Journal of advanced manufacturing technologies 25*, 1 (2005), 471–479.

[129] Pinto, M. A., Cheung, N., Ierardi, M. C. F., and Garcia, A. Microstructural and hardness investigation of an aluminum-copper alloy processed by laser surface melting. *Materials Characterization 50*, 2-3 (2003), 249 – 253.

[130] Pogson, S., Fox, P., Sutcliffe, C., and Neill, W. O. The production of copper parts using DMLR. *Rapid Prototyping Journal 9*, 5 (2003), 334–343.

[131] Pohl, H., Simchi, A., Issa, M., and Dias, H. C. Thermal stresses in direct metal laser sintering. In *Proceedings of the 12th Solid Freeform Fabrication Symposium, Austin, TX* (2001).

[132] Prime, M. Residual stress measurement by successive extension of a slot: The crack compliance method. *Applied Mechanics Reviews 52*, 2 (1999), 75–96.

[133] Pyka, G., Kerckhofs, G., Papantoniou, I., Speirs, M., Schrooten, J., and Wevers, M. Surface roughness and morphology customization of additive manufactured open porous Ti6Al4V structures. *Materials 6*, 10 (2013), 4737–4757.

[134] Ramos-Grez, J., and Bourell, D. Reducing surface roughness of metallic freeform-fabricated parts using non-tactile finishing methods. *International Journal of Materials and Product Technology 21*, 4 (2004), 297–316.

[135] Rännar, L.-E., Glad, A., and Gustafson, C.-G. Efficient cooling with tool inserts manufactured by electron beam melting. *Rapid Prototyping Journal 13*, 3 (2007), 128–135.

[136] Roberts, G. A., and Kennedy, R. *Tool steels.* ASM International, 1998.

[137] Rombouts, M. *Selective Laser Sintering / Melting of iron-based powders.* PhD thesis, University of Leuven (KU Leuven), Department of Materials Science, 2006.

[138] Rombouts, M., Kruth, J.-P., Froyen, L., and Mercelis, P. Fundamentals of selective laser melting of alloyed steel powders. *CIRP Annals - Manufacturing technology 55*, 1 (2006), 187–192.

[139] Santos, E., Shiomi, M., Osakada, K., and Laoui, T. Rapid manufacturing of metal components by laser forming. *International Journal of Machine Tools and Manufacture 46*, 12–13 (2006), 1459–1468.

[140] Sexton, L., Lavin, S., Byrne, G., and Kennedy, A. Laser cladding of aerospace materials. *Journal of Materials Processing Technology 122*, 1 (2002), 63 – 68.

[141] Shamantha, C., Narayanan, R., Iyer, K., Radhakrishnan, V., Seshadri, S., Sundararajan, S., and Sundaresan, S. Microstructural changes during welding and subsequent heat treatment of 18Ni (250-grade) maraging steel. *Materials Science and Engineering: A 287*, 1 (2000), 43–51.

[142] Shi, B., and Attia, H. Integrated process of laser-assisted machining and laser surface heat treatment. *Journal of Manufacturing Science and Engineering 135*, 6 (2013), 061021.

[143] Shiomi, M., Osakada, K., Nakamura, K., T.Yamashita, and F.Abe. Residual stress within metallic model made by selective laser melting process. *CIRP Annals - Manufacturing technology 53*, 1 (2004), 195–198.

[144] Simchi, A., and Asgharzadeh, H. Densification and microstructural evaluation during laser sintering of M2 high speed steel powder. *Materials science and technology 20*, 11 (2004), 1462–1468.

[145] Sistiaga, M. L. M. Selective Laser Melting of high melting point metals: Tantalum and Tungsten. Tech. rep., Mondragon University and KU Leuven, 2012.

[146] Stanford, M., Kibble, K., Lindop, M., Mynors, D., and Durnall, C. An investigation into fully melting a maraging steel using direct metal laser sintering. In *Metal forming conference* (2008), vol. 79, pp. 847–852.

[147] Steen, W., Mazumder, J., and Watkins, K. *Laser Material Processing.* Springer, London, 2003.

[148] Stratasys. Online, May 2014. http://www.stratasys.com/.

[149] The Additive Manufacturing Platform EU. Additive manufacturing: Strategic research agenda 2011 a future vision for am, 2011. Industrial roadmap for Europe.

[150] Thijs, L. *Microstructure and texture of metal parts produced by Selective Laser Melting.* PhD thesis, University of Leuven (KU Leuven), Department of Materials Science, 2014.

[151] Thijs, L., Humbeeck, J. V., Kempen, K., Yasa, E., Kruth, J.-P., and Rombouts, M. Investigation on the inclusions in maraging steel produced by selective laser melting. In *Innovative developments in Virtual and Physical Prototyping.* (2011), pp. 297–304.

[152] Thijs, L., Kempen, K., Kruth, J.-P., and Humbeeck, J. V. Fine-structured aluminium products with controllable texture by selective laser melting of pre-alloyed AlSi10Mg powder. *Acta Materialia 61*, 5 (2012), 1809–1819.

[153] Thijs, L., Verhaeghe, F., , Craeghs, T., Humbeeck, J. V., and Kruth, J.-P. A study of the microstructural evolution during selective laser melting of Ti-6Al-4V. *Acta Materialia 58*, 1 (2010), 3303–3312.

[154] Tolochko, N., Khlopkov, Y., Mozzharov, S., Ignatiev, M., Laoui, T., and Titov, V. Absorptance of powder materials suitable for laser sintering. *Rapid prototyping journal 6*, 3 (2000), 155–161.

[155] Tolochko, N., Mozzharov, S., Yadroitsev, I., Laoui, T., Froyen, L., Titov, V., and Ignatiev, M. Balling processes during selective laser treatment of powders. *Rapid prototyping journal 10*, 2 (2004), 78–87.

[156] Totten, G., Howes, M., and Inoue, T. *Handbook of residual stress and deformation of steel.* ASM International, Materials Park, Ohio, 2002.

[157] Toyserkani, E., Khajepour, A., and Corbin, S. *Laser Cladding.* CRC Press, Florida, USA, 2005.

[158] Trumpf. Trumpf laser technology. On the WWW, May 2014. http://www.trumpf-laser.com.

[159] Vaerenbergh, J. V. *Process optimisation in Selective Laser Melting.* PhD thesis, Universiteit Twente, Netherlands, 2008.

[160] Vandenbroucke, B., and Kruth, J.-P. Selective laser melting of biocompatible metals for rapid manufacturing of medical implants. *Rapid Prototyping Journal 13*, 4 (2007), 196–202.

[161] Ventola, L., Chiavazzo, E., Calignano, F., Manfredi, D., and Asinari, P. Heat transfer enhancement by finned heat sinks with micro-structured roughness. *Journal of Physics: Conference Series 494*, 1 (2014), 012009.

[162] Verhaeghe, F., Craeghs, T., Heulens, J., and Pandelaers, L. A pragmatic model for selective laser melting with evaporation. *Acta Materialia 57*, 20 (2009), 6006–6012.

[163] Vojtech, D., Serak, J., and Ekrt, O. Improving the casting properties of high-strength aluminium alloys. *Materiali in Tehnologie 38*, 1–2 (2004), 99–102.

[164] Vollertsen, F., and Rodle, M. Model for the temperature gradient mechanism of laser bending. In *Proceedings of the LANE Conference* (1994), vol. 94, pp. 371–378.

[165] Voncina, M., Mrvar, P., and Medved, J. Thermodynamic analysis of AlSi10Mg alloy. *RMZ Materials and Geoenvironment 52*, 3 (2006), 621–633.

[166] Vrancken, B., Thijs, L., Kruth, J.-P., and Van Humbeeck, J. Microstructure and mechanical properties of a novel β titanium metallic composite by selective laser melting. *Acta Materialia 68* (2014), 150–158.

[167] Watkins, K., McMahon, M., and Steen, W. Microstructure and corrosion properties of laser surface processed aluminium alloys: a review. *Materials Science and Engineering: A 231*, 1 (1997), 55–61.

[168] Wehmoeller, M., Warnke, P., Zilian, C., and Eufinger, H. Implant design and production of a new approach by selective laser melting. *International Congress Series 1281*, 0 (2005), 690 – 695.

[169] Welkenhuyzen, F., Boeckmans, B., Kiekens, K., Tan, Y., Dewulf, W., and Kruth, J.-P. Accuracy study of a 450kv CT system with a calibrated test object. In *Proceedings of International symposium on measurement and quality control* (2013).

[170] Weston, J., Yoon, J., and Wallach, E. Laser welding of aluminium alloys using different laser sources. In *CISFFEL6, 6th International Conference on Welding and Melting by Electron and Laser Beams, Toulon* (2003).

[171] Withers, P., and Bhadeshia, H. Residual stress. part 2, nature and origins. *Materials Science and Technology 17*, 4 (2001), 366–375.

[172] Wohlers, T. *Wohlers Report 2013*. Wohlers Associates, USA, 2013. ISBN 0975442996.

[173] Wohlers Associates, i. Additive manufacturing technology roadmap for australia, March 2011. Industrial roadmap for Australia.

[174] Wong, T., Liang, G., and Tang, C. The surface character and substructure of aluminium alloys by laser-melting treatment. *Journal of materials processing technology 66*, 3 (1997), 172–178.

[175] Wu, X., and Mei, J. Near net shape manufacturing of components using direct laser fabrication technology. *Journal of Materials Processing Technology 135*, 2-3 (2003), 266 – 270.

[176] Xiao, R., and Zhang, X. Problems and issues in laser beam welding of aluminum–lithium alloys. *Journal of Manufacturing Processes 16*, 2 (2014), 166–175.

[177] Xu, W., Yue, T., Man, H., and Chan, C. Laser surface melting of aluminium alloy 6013 for improving pitting corrosion fatigue resistance. *Surface and Coatings Technology 200*, 16-17 (2006), 5077 – 5086.

[178] Xue, L., and Islam, M. Free-form laser consolidation for producing metallurgically sound and functional components. *Jounal of laser applications 12*, 4 (2000), 160–165.

[179] Yadroitsev, I., Bertrand, P., and Smurov, I. Parametric analysis of the selective laser melting process. *Applied surface science 253*, 19 (2007), 8064–8069.

[180] Yadroitsev, I., Gusarov, A., Yadroitsava, I., and Smurov, I. Single track formation in selective laser melting of metal powders. *Journal of materials processing technology 210*, 12 (2010), 1624–1631.

[181] Yadroitsev, I., and Smurov, I. Surface morphology in selective laser melting of metal powders. *Physics Proceedia 12*, 1 (2011), 264–270.

[182] Yadroitsev, I., Thivillon, L., Bertrand, P., and Smurov, I. Strategy of manufacturing components with designed internal structure by selective laser melting of metallic powder. *Applied Surface Science 254*, 4 (2007), 980 – 983.

[183] Yasa, E. *Manufacturing by combining Selective Laser Melting and Selective Laser Erosion/Laser re-melting.* PhD thesis, University of Leuven (KU Leuven), Department of Mechanical Engineering, 2011.

[184] Yasa, E., Deckers, J., and Kruth, J.-P. The investigation of the influence of laser re-melting on density, surface quality and microstructure of selective laser melted parts. *Rapid Prototyping Journal 17*, 5 (2011), 312–327.

[185] Yasa, E., Deckers, J., Kruth, J.-P., Rombouts, M., and Luyten, J. Charpy impact testing of metallic selective laser melting parts. *Virtual and Physical Prototyping 5*, 2 (2010), 89–98.

[186] Yasa, E., Kempen, K., Kruth, J.-P., Thijs, L., and Humbeeck, J. V. Microstructure and mechanical properties of maraging steel 300 after selective laser melting. In *Proceedings of the 21st Solid Freeform Fabrication Symposium* (2010).

[187] Yasa, E., and Kruth, J.-P. Microstructural investigation of selective laser melting 316l stainless steel parts exposed to laser re-melting. *Procedia Engineering 19*, 1 (2012), 389–395.

[188] Zaeh, M. F., and Branner, G. Investigations on residual stresses and deformations in selective laser melting. *Production Engineering 4*, 1 (2010), 35–45.

[189] Zhang, K., Liu, W., and Shang, X. Research on the processing experiments of laser metal deposition shaping. *Optics and Laser Technology 39*, 3 (2007), 549 – 557.

[190] Zhang, Y., Chen, J., Lei, W., and Xv, R. Effect of laser surface melting on friction and wear behavior of AM50 magnesium alloy. *Surface and Coatings Technology 202*, 14 (2008), 3175 – 3179.

[191] Zhao, H., and DebRoy, T. Pore formation during laser beam welding of die-cast magnesium alloy AM60B-mechanism and remedy. *Welding Journal 80*, 8 (2001), 204–210.

[192] Zhao, H., Niu, W., Zhang, B., Lei, Y., Kodama, M., and Ishide, T. Modelling of keyhole dynamics and porosity formation considering the adaptive keyhole shape and three-phase coupling during deep-penetration laser welding. *Journal of physics D: Applied Physics 44*, 48 (2011), 485302.

[193] Zhou, X. F., Fang, F., and Jiang, J. Q. A study on the microstructure of AISI M2 high speed steel manufactured by continuous casting. *Advanced Materials Research 146* (2011), 1211–1215.

Curriculum Vitae

Personalia

Karolien Kempen
E-mail: kempen.karolien@gmail.com
Date of Birth: January 25, 1987, Geel, Belgium

Education

- **2010 - 2015**: PhD Student
  Department of Mechanical Engineering, University of Leuven (KU Leuven)
- **2008 - 2010**: Master of Mechanical Engineering
  Department of Mechanical Engineering, University of Leuven (KU Leuven)
  Cum laude
- **2004 - 2008**: Master of Industrial Sciences: Electromechanical Engineering
  Katholieke Hogeschool Kempen, Geel.
  Cum laude

Professional experience

- **2014 - present**: Lecturer
  Department of Mechanical Engineering Technology, TC Geel , University of Leuven (KU Leuven)
  - Strength of Materials
  - Strength of Materials: part 2
  - Machine Components
- **2014 - present**: Research Engineer Biomechanics
- **2010 - 2014**: Research Engineer Additive Manufacturing
  Department of Mechanical Engineering, University of Leuven (KU Leuven)
- **2010 - 2014**: Teaching Assistant
  Department of Mechanical Engineering, University of Leuven (KU Leuven)
  - Advisor of 7 master theses
  - Production Engineering and systems: Lab sessions
  - Dimensional Metrology: Lab sessions
  - Non-conventional machining: Lab sessions
  - Student counselor Bachelor students
- **2012 - 2013**: Conference Manager
  17th CIRP Conference on Electro Physical and Chemical Machining (ISEM).

List of publications

Articles in internationally reviewed academic journals

- Kempen, K., Vrancken, B., Buls, S., Thijs, L., Van Humbeeck, J., Kruth, J. (2014). Selective Laser Melting of crack-free high density M2 HSS parts by baseplate pre-heating. *Journal of Manufacturing Science and Engineering*, 136(6), art.nr. MANU-14-1285; doi: 10.1115/1.4028513.

- Kempen, K., Thijs, L., Van Humbeeck, J., Kruth, J. (2014). Processing AlSi10Mg by Selective Laser Melting: Parameter optimization and material characterization. *Materials Science and Technology*, art.nr. 10.1179/1743284714Y.

- Mertens, R., Clijsters, S., Kempen, K., Kruth, J. (2014). Optimisation of Scan Strategies in Selective Laser Melting of Aluminium Parts With Downfacing Areas. *Journal of Manufacturing Science and Engineering*, 136 (6), art.nr. MANU-14-1191.

- Clijsters, S., Craeghs, T., Buls, S., Kempen, K., Kruth, J. (2014). In-situ Quality Control of the Selective Laser Melting Process using a High Speed, Real-Time Melt Pool Monitoring System. *International Journal of Advanced Manufacturing Technology*, art.nr. JAMT-D-14-00830R1.

- Thijs, L., Kempen, K., Kruth, J., Van Humbeeck, J. (2013). Fine-structured aluminium products with controllable texture by Selective Laser Melting of pre-alloyed AlSi10Mg powder. *Acta Materialia*, 61 (5), 1809-1819.

Articles in international conference proceedings

- Qian, J., Kempen, K., Welkenhuyzen, F., Vanderauwera, W., Kuijpers, A., Wang, J., Yang, F., Kruth, J.-P., Reynaerts, D. (2015) A novel process chain for manufacturing μIM mould inserts with conformal cooling. (submitted) *4M/ ICOMM 2015*, Milan, Italy, 31 March - 2 April 2015.

- Mertens, R., Kempen, K., Clijsters, S., Kruth, J. (2014). Production of AlSi10Mg parts with downfacing areas by Selective Laser Melting. *PMI.* Guimarães, Portugal, 10-12 september 2014.

- Buls, S., Clijsters, S., Kempen, K., Kruth, J. (2014). Melt Pool System Identification and Feedback Control for Selective Laser Melting. *PMI.* Guimarães, Portugal, 10-12 september 2014.

- Schubert, A., Zeidler, H., Martin, A., Kempen, K., Hackert-Oschätzchen, M., Kruth, J. (2014). Jet-Electrochemical Machining of Selective Laser melted Aluminum and Steel alloy for Micro Injection Moulding. *Proceedings of the 14th euspen International Conference.* euspen

- Kempen, K., Welkenhuyzen, F., Qian, J., Kruth, J. (2014). Dimensional accuracy of internal channels in SLM produced parts. . *ASPE spring topical meeting.* California, US, 13-16 april 2014.

- Vrancken, B., Kempen, K., Thijs, L., Kruth, J., Van Humbeeck, J. (2014). Adapted heat treatment of Selective Laser Melted materials. In Danninger, H. (Ed.), *Proceedings of the Euro PM 2014 Congress.* Euro PM2014 Congress. Salzburg, Austria, 21-24 September 2014 (pp. 1-6). Shrewsbury: European Powder Metallurgy Association (EPMA).

- Qian, J., Kempen, K., Wang, J., Yang, C., Reynaerts, D. (2014). A holistic approach for μEDM milling on SLMed steel. In Leach, R. (Ed.), *Proceedings of the 14th euspen International Conference: Vol. 2.* euspen International Conference. Dubrovnik, 1-6 June 2014 (pp. 404-408).

- Buls, S., Craeghs, T., Clijsters, S., Kempen, K., Swevers, J., Kruth, J. (2013). The influence of a dynamically optimized galvano based laser scanner on the total scan time of SLM parts. . *Solid Freeform Fabrication Symposium.* Austin, Texas USA, 12-15 August 2013.

- Kempen, K., Vrancken, B., Thijs, L., Buls, S., Van Humbeeck, J., Kruth, J. (2013). Lowering thermal gradients in Selective Laser melting by preheating the baseplate. *Solid Freeform Fabrication Symposium Proceedings.* solid freeform fabrication Symposium. Austin, Texas USA, 12-15 august 2013.

- Kempen, K., Thijs, L., Van Humbeeck, J., Kruth, J. (2012). Mechanical properties of AlSi10Mg produced by Selective Laser Melting. *Physics Procedia*: Vol. 39 (pp. 439-446) Elsevier BV.
- Thijs, L., Van Humbeeck, J., Kempen, K., Yasa, E., Kruth, J., Rombouts, M. (2012). Investigation on the inclusions in maraging steel produced by selective laser melting. *Innovative Developments in Virtual and Physical Prototyping.* International Conference on Advanced Research in Virtual and Rapid Prototyping (VRAP). Leiria, Portugal, 28 September - 1 October 2011 (pp. 297-304). P.O. Box 447, 2300 AK Leiden, The Netherlands: CRC Press/Balkema.
- Liu, Z., Chua, C., Leong, K., Kempen, K., Thijs, L., Yasa, E., Van Humbeeck, J., Kruth, J. (2012). A preliminary investigation on selective laser melting of M2 high speed steel. *Innovative developments in virtual and physical prototyping: Vol. 1.* International Conference on Advanced Research in Virtual and Rapid Prototyping (VRAP). Leiria, Portugal, 28 September - 1 October 2011 (pp. 339-346). London: Taylor & Francis group.
- Kempen, K., Yasa, E., Thijs, L., Kruth, J., Van Humbeeck, J. (2011). Microstructure and mechanical properties of Selective Laser Melted 18Ni-300 steel. *Physics Procedia: Vol. 12 (1).* 6th International WLT Conference on Lasers in Manufacturing (LiM). Munich, GERMANY, MAY 23-26, 2011 (pp. 255-263) Elsevier BV.
- Kempen, K., Thijs, L., Yasa, E., Badrossamay, M., Verheecke, W., Kruth, J. (2011). Microstructural Analysis and Process Optimization for Selective Laser Melting of AlSi10Mg. *Solid Freeform Fabrication Symposium Proceedings.* Solid Freeform Fabrication Symposium. Austin, Texas, USA, 8-10 August 2011.
- Yasa, E., Kempen, K., Kruth, J., Thijs, L., Van Humbeeck, J. (2010). Microstructure and mechanical properties of maraging steel 300 after Selective Laser Melting. *Solid Freeform Fabrication Symposium Proceedings.* Solid Freeform Fabrication Symposium. Austin, Texas, USA, 12-14 August, 2010

Chapter in academic book

- Kruth, J.-P., Dadbakhsh, S., Vrancken, B., Kempen, K., Vleugels, J., Van Humbeeck, J. (2015). Additive manufacturing of metals via selective laser melting: process aspects and material developments. *Additive Manufacturing: Innovations, Advances and Applications.*

Meeting abstracts, presented at international scientific conferences

- Thijs, L., Badrossamay, M., Clijsters, S., Craeghs, T., Deckers, J., Kempen, K., Yasa, E., Kruth, J., Van Humbeeck, J. (2010). Additive Manufacturing: Selective Laser Sintering & Selective Laser Melting. *Van Cauterenleerstoel.* Leuven, Belgium, 24 November 2010.
- Brinksmeier, E., Riemer, O., Brandao, C., Kempen, K., Kruth, J. (2013). Micro Milling of Additive Manufactured Metals. *Micro/nano manufacturing workshop.* Karlsruhe, Germany, 27-28 November 2013.

External reports

- Wohlers, T. (2013). *Wohler's report 2013*, Wohlers Associates, Inc.
- Wohlers, T. (2012). *Wohler's Report 2012*, Wohlers Associates, Inc.

Science popularization

- Kempen, K. Lauwers, B. (as contr.) (2013). Combinatie van additive manufacturing en oppervlaktebewerking met één laser. *Made different (online)* (01/2013).

Master's thesis

- Kempen, K., Van Humbeeck, J., Kruth, J.-P. Microstructuur en mechanische eigenschappen van 18Ni-300 staal bewerkt door Selectief Laser Smelten, Katholieke Universiteit Leuven (KU Leuven), Leuven, 2010.
- Kempen, K., Van der Vliet, J., Van Genechten, F., Swinnen, W. Ontwerp en realisatie van een boot op zonne-energie. Katholieke Hogeschool Kempen, Geel, 2008.

FACULTY OF ENGINEERING SCIENCE
DEPARTMENT OF MECHANICAL ENGINEERING
PRODUCTION, AUTOMATION AND MACHINE DESIGN
Celestijnenlaan 300 box 2420
B-3001 Heverlee
Karolien.Kempen@kuleuven.be
http://www.mech.kuleuven.be